THE UTILITY OF MULTILEVEL PRESSURE MEASUREMENTS IN MONITORING GEOLOGICALLY STORED CARBON DIOXIDE

A REPORT SUBMITTED TO THE DEPARTMENT OF ENERGY RESOURCES ENGINEERING

OF STANFORD UNIVERSITY

IN PARTIAL FULFILLMENT OF THE REQUIREMENTS FOR THE DEGREE OF MASTER OF SCIENCE

By
Christin Weierholt Strandli
June 2011

I certify that I have read this report and that in my opinion it is fully adequate, in scope and in quality, as partial fulfillment of the degree of Master of Science in Petroleum Engineering.

_____

Prof. Sally M. Benson
(Principal Advisor)

Abstract

Emissions of carbon dioxide (CO_2) due to the burning of fossil fuels are cited by the Intergovernmental Panel on Climate Change (IPCC) as virtually certain to have a dominant influence on atmospheric concentrations of CO_2 in the 21st century. A growing concern is that the presently rapid increase of greenhouse gases in the atmosphere contributes to climate change. CO_2 being the predominant greenhouse gas, much emphasis has been placed on how to reduce CO_2 emissions. One promising approach is carbon dioxide capture and storage (CCS). CCS can be summarized as the process through which CO_2 is captured from a stationary emission source (e.g. a power plant) and stored permanently in an underground geologic formation overlain by a 'caprock' formation with sealing properties. CCS has received a great deal of attention because it has the potential to significantly reduce anthropogenic CO_2 emissions while at the same time utilizing technology used in other industries.

Critical to large-scale implementation of CCS is the ability to monitor the injected CO_2 to ensure permanent sequestration. A monitoring method currently under investigation involves having multiple, vertically distributed pressure sensors in a monitoring well that extends down to the depth of injection. This study examines the extent to which multilevel pressure measurements in the storage reservoir, seal, and overlying aquifer can provide information on where the CO_2 as well as the displaced brine migrate in the reservoir.

The study is conducted using the TOUGH2 multiphase flow simulator. Based on assumed geology at a CCS demonstration project site in Illinois, we investigate multilevel pressure measurements in a 30-layer system where supercritical CO_2 is injected in the bottom layers of a 23-layer storage reservoir. A six-layer shale formation comprises the seal and a one-layer sandstone aquifer overlies the seal. Porosity, permeability, and the capillary pressure curve are uniquely defined for each layer. A total of one million metric tons are injected over three years.

Four basic scenarios for the constructed geologic system are studied: 1) homogeneous and isotropic, 2) homogeneous and anisotropic, 3) heterogeneous and

isotropic, and 4) heterogeneous and anisotropic. For practical purposes, the fourth scenario is the most realistic scenario, as every real reservoir will have some degree of heterogeneity and anisotropy. Because it is critical to know whether the presence of CO_2 in the system gives rise to a distinct pressure response compared to when there is just water flowing, we also conduct a sensitivity study on the effects of CO_2 injection versus pure water injection, assuming equivalent volumetric injection flow rates.

Examination of the pressure responses shows that large, detectable pressure changes can be observed for all of the scenarios. Distinct pressure transients for the different system scenarios suggest that heterogeneity greatly impacts the pressure response. Normalized vertical pressure gradients nevertheless appear to be more diagnostic of the nature of the system heterogeneity and CO_2 plume location rather than pressure transients from individual monitoring points alone. Normalized vertical pressure gradients provide 1) a clear representation of the system heterogeneity soon after start of injection, 2) distinct features depending on whether CO_2 is present in the system, and 3), a strong indication of where the CO_2 is in the reservoir, i.e. at what depth, prior to the CO_2 arriving at the monitoring well. Anomalous vertical pressure gradients can be attributed to anomalous vertical aqueous flow caused by water displacement due to the advancing CO_2 plume. Based on these results it seems beneficial to place as many pressure monitors as possible in the system; especially at the depth of injection and in low permeability layers above. The study presented here confirms the basis for an inverse method for reservoir characterization and CO_2 plume migration detection.

Acknowledgments

My deepest thanks go to my advisor, Dr. Sally Benson, for her patience, encouragement, and excellent scientific insight. I admire her sense of intuition and ability to guide.

I would also like to thank the members of the Benson Lab research group, especially postdocs Sam Krevor and Ronny Pini for providing constructive feedback and asking interesting questions worth pursuing in my research. Also, thanks to Whitney Sargent for proof reading parts of my Master's Report.

My fellow classmates in the Department of Energy Resources deserve to be acknowledged for providing an excellent study environment and for being extraordinarily nice and friendly. In particular, I would like to thank my three officemates, Monrawee Pancharoen, Xiaochen Wang, and Abby Kirchofer, for always having time to help, give advice, and share fun stories. My two years here at Stanford would not have been the same without you!

Finally, special thanks to Lilja Magnúsdóttir and Folake Ogunbanwo for being who you are. I am forever grateful for having gotten to know you.

Contents

List of Tables

List of Figures

Chapter 1

1. Introduction

1.1. Climate Change and Carbon Capture and Storage as a Mitigative Approach

According to the Intergovernmental Panel on Climate Change's (IPCC) Fourth Assessment Report, it is "extremely likely" that human activities have caused a significant net warming influence on the climate since 1750 (Solomon et al., 2007). There has been a larger rate of increase in radiative forcing from carbon dioxide (CO_2), methane (CH_4), and nitrous oxide (N_2O) for the past 40 years than at any time during the past 2000 years (Solomon et al., 2007). CO_2 is cited as the most important anthropogenic greenhouse gas (Solomon et al., 2007). From the 1990s to the time period 2000 to 2005, annual emissions of CO_2 from burning of fossil fuels, cement production, and gas flaring, increased from a mean of 6.4 ± 0.4 GtC per year to 7.2 ± 0.3 GtC per year (Solomon et al., 2007). According to the IPCC Special Report on Carbon Capture and Storage, "emissions of CO_2 due to fossil fuel burning are virtually certain to be the dominant influence on the trends in atmospheric CO_2 concentration during the 21st century" (IPCC, 2005). A further increase in average global temperature can be minimized by reducing atmospheric concentrations of CO_2. One way to reduce atmospheric concentrations of CO_2 is through carbon dioxide capture and storage (CCS). In short, CCS can be summarized as the process through which CO_2 is captured from a stationary emission source (e.g. a power plant) and stored permanently in a subsurface geologic formation.

CCS has received a great deal of attention because it has the potential to greatly reduce greenhouse gas emissions and because it utilizes technology already used in the oil and gas industry and in the field of hydrology. The basic process from "source to sink" is shown in Figure 1; CO_2 is first separated and captured from a large stationary emission source, then compressed and transported to the storage site, and finally injected into an appropriate subsurface geologic formation for permanent storage. Geologic formations evaluated for storage potential include deep saline aquifers, depleted oil and

gas reservoirs, and unminable coal seems, of which deep saline aquifers are regarded the most promising (NETL, 2009). In order for a geologic formation to be considered suitable, it needs to be sufficiently deep that the pressure and temperature stay high enough for the sequestered CO_2 to remain in the supercritical state. Supercritical fluids are fluids that exhibit both gas-like and liquid-like properties. In particular, supercritical CO_2 is denser than gaseous CO_2, which means it occupies less pore space and therefore can be stored more efficiently. In addition, a suitable geologic formation should be overlain by a sufficiently thick and low-permeability caprock that can act like a seal to upward-flowing CO_2.
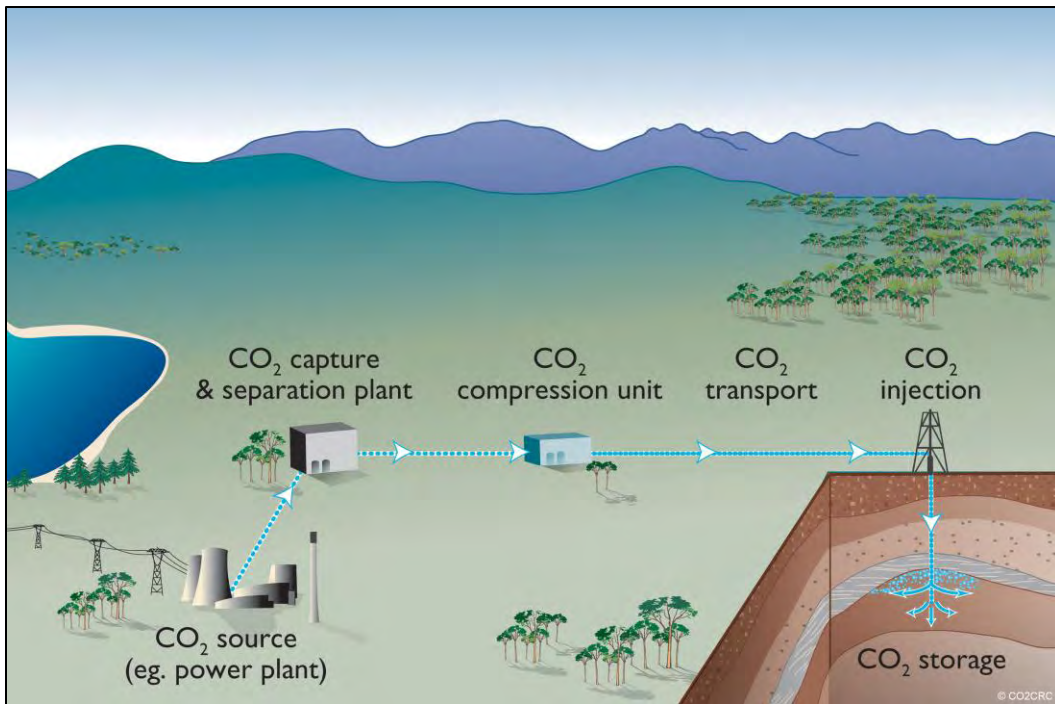
Figure 1.1: Basic process flow of geologic CCS

(Image from CO2SRC, http://www.co2crc.com.au/images/imagelibrary/gen_diag/ccsprocess_media.jpg)

A significant amount of research has been devoted to CCS, and a number of demonstration projects are currently in place to validate the ability of deep saline aquifers to serve as permanent storage reservoirs for CO_2.

1.2. Monitoring, Verification, and Accounting

Critical to large-scale implementation of CCS is the ability to monitor the CO_2 that has been injected underground. The motivation for monitoring is twofold. First, a primary objective is to ensure that the injected CO_2 remains sequestered and does not leak into overlying formations, such as groundwater aquifers (sources for drinking water), or into the atmosphere. Leakage into the atmosphere would defy the whole purpose of CCS, and leakage into groundwater aquifers or surface vegetation could pose health hazards to humans as well as animals. In cases where there are regulatory limits on emissions in place and/or tax credits may be received for avoiding emissions, it is important to confirm that the quantity stored is reported correctly. Second, monitoring is critical for tracking where the CO_2 migrates in the reservoir. This aids in updating the estimates of reservoir capacity and also serves to ensure that the CO_2 does not migrate beyond legal geographical boundaries or into regions where the geology is less favorable.

There are currently three main categories of monitoring techniques: atmospheric, near-surface, and subsurface (NETL, 2009). Atmospheric monitoring techniques include measurements of eddy covariance, Laser Systems and Light Detection and Ranging (LIDAR), and infrared analysis. Eddy covariance measurements involve observation of atmospheric fluxes of CO_2 over a relatively large area above the injection site (m^2 to km^2). The LIDAR technique determines concentrations of CO_2 in the atmosphere based on the amount of attenuation of a light pulse that is reflected over the injection site, and infrared analysis is used to detect concentrations of CO_2 in the soil air (NETL, 2009).

Near-surface monitoring techniques involve measurements performed either directly on the surface or directly below. Near-surface monitoring includes measurements of small changes in surface topography using tiltmeters, CO_2 concentrations in soil and vadose zone gas, and groundwater properties such as pH (NETL, 2009).

Subsurface monitoring involves placing instruments deep in the ground, in or close to the storage reservoir, or, measurements can be conducted through instruments on the surface, such as 3D time-lapse seismic surveys. Examples of subsurface monitoring techniques include cross-well seismic surveys, well logging, and electromagnetic surveys (NETL, 2009).

Operational monitoring includes the same monitoring techniques as the pre-operational phase; this time with the goal of detecting any deviations from the pre-operational measurements. The operational phase may last up to 50 years, possibly longer if the storage project is very large (Benson et al., 2004).

Closure monitoring refers to monitoring after the injection of CO_2 has ceased and the storage facilities have been closed off. This phase should last long enough to ensure that there is no leakage and no unexpected changes in the conditions at the storage site (Benson et al., 2004).

The post-closure monitoring phase may be required if a leak is suspected or if additional information about the storage site is needed. In the case of a leak, the post-closure phase will continue until the leak has been remedied (Benson et al., 2004).

Another aspect of any monitoring program is the cost associated with material, implementation, personnel, maintenance, and data processing. Given that the lifespan of a project may be several decades, spanning from the pre-injection phase to the closure- or post-closure phase, monitoring costs may comprise a significant portion of the long-term costs of a storage project. A monitoring program should be designed to provide the information required with optimal resolution without being so expensive so as to obstruct the project (IPCC, 2005).

Finally, if a leak develops, deep subsurface measurements are likely to provide the earliest indications of CO_2 leaking out of the storage reservoir. Subsurface monitoring instruments placed on the surface, e.g. instruments for 3D time-lapse seismic surveys, may not provide a high enough resolution for early-stage, small leaks to be detected (IPCC, 2005). Near-surface or surface monitoring instruments may only detect leakage after CO_2 has already escaped from the storage reservoir and arrived in the near-surface region or in the atmosphere (IPCC, 2005). The earlier the detection the better, as one would like to take remedial action before CO_2 reaches the surface and the atmosphere (Benson and Hepple, 2005).

1.3. Pressure Transient Measurements

Deep surface measurements in the form of pressure transients (pressure changes over time), are used in this investigation to evaluate their effectiveness in providing information about fluid movement in the reservoir. In particular, we examine pressure buildups in the reservoir with respect to the initial pressure of the storage reservoir and overlying formations.

Pressure transients are due to changes in production or injection fluids (Horne, 1995) (i.e. variations in fluid volume) and have been studied by hydrologists and petroleum engineers for decades to characterize and better understand the behavior of fluid-filled geologic reservoirs. In the United States, underground natural gas storage projects have been operated successfully for more than 90 years (Benson et al., 2002) as a means to meet supply and demand in the natural gas market. This process has many operational similarities to CCS. Many of the techniques used for monitoring of natural gas storage, to make sure that the gas stays where it should and does not leak, as well as techniques developed for remediation in the case a leak were to occur, can be considered for use in CCS (Benson et al., 2002). One example includes drilling a vertical monitoring well into a permeable geologic formation that lies directly above the primary sealing caprock. The pressure changes observed in the monitoring well are observed throughout the operational phase. If a leak were to occur, the leak would be indicated by an increase in pressure in the monitoring well. The idea of 'above-zone monitoring' was first proposed by Katz and Coats (1968).

While pressure transients above the sealing caprock have been studied in the context of CCS with the goal of detecting possible leakage, the concept of having multiple, vertically distributed pressure sensors in a monitoring well that extends down to the depth of injection, has not yet been evaluated for CCS and is unique to this investigation. In particular, we would like to evaluate the extent to which vertically distributed pressure monitors in the storage reservoir, seal, and overlying aquifer can provide information on where the CO_2 as well as the brine that the CO_2 displaces migrate in the reservoir.

The simulation study presented here is based on the Illinois Basin-Decatur Project in east-central Illinois led by the combined efforts of the Midwest Geological Sequestration Consortium (MGSC), the Illinois State Geological Survey (ISGS), Schlumberger Carbon Services, U.S. Department of Energy, and Archer Daniels Midland Company (ADM). The five parties have teamed together to conduct a study to demonstrate the ability of the Mt. Simon Sandstone formation to accept and store one million metric tons of CO_2 captured from ADM's ethanol plant in Decatur, Illinois (Finley, 2009). A vertical monitoring well is drilled that will have multiple pressure sensors in the storage reservoir, seal, and overlying aquifer.

1.4. Scope of Research

In this investigation, a simulation study is conducted to evaluate the effectiveness of vertically distributed pressure monitors in the storage reservoir, seal, and overlying aquifer, with the following objectives:

- Evaluate the magnitudes of the pressure buildups over time. Will they be large enough to be detected?
- Examine the effect of heterogeneity and anisotropy of the system on the pressure transients. Do the pressure transients appear to capture the nature of heterogeneity of the system?
- Determine whether, and how, the pressure data can be used to anticipate or track migration of the CO_2 plume.
- Based on findings, discuss the placement and distribution of pressure sensors in the monitoring well. Are there certain depth intervals at which it is more critical to place pressure sensors?

Addressing these questions should provide the groundwork for further investigation of multilevel pressure monitoring as an effective monitoring tool in the context of CCS.

Chapter 2

2. Literature Review

2.1. Pressure Transient Analysis

Pressure transient analysis, i.e. the analysis of pressure changes over time, has been used by hydrologists and petroleum engineers for a number of years to characterize and better understand the behavior of fluid-filled geologic reservoirs. Pressure changes over time are associated with small variations in the fluid volume. From pressure transient analysis, estimates of reservoir size and the ability of the formation to produce or accept fluids can be obtained (Oilfield Glossary, 2011).

Typically, fluids are exchanged through and pressure is measured in a cylindrical wellbore. The cylindrical form of the pressure-diffusion equation for a slightly compressible fluid in a porous medium is given by Equation 2.1:

$$\frac{\partial^2 p}{\partial r^2} + \frac{1}{r}\frac{\partial p}{\partial r} + \frac{k_\theta}{k_r}\frac{1}{r^2}\frac{\partial^2 p}{\partial \theta^2} + \frac{k_z}{k_r}\frac{\partial^2 p}{\partial z^2} = \frac{\varphi \mu c_t}{k_r}\frac{\partial p}{\partial t} \qquad (2.1)$$

where p is the pressure, r is the radial distance from the center of the wellbore, z is the vertical position in the reservoir, θ is the azimuthal orientation, k_r, k_θ, and k_z are the directional components of the permeability tensor, φ is the porosity of the rock, μ is the viscosity of the fluid, and c_t is the total compressibility of the rock-fluid system.

For a confined homogeneous, isotropic, horizontal reservoir, where the fluid flow is single-phase and the wellbore can be assumed to act as a line source in an infinite-extending reservoir, the solution is proposed by Theis (1935) as:

$$p(r,t) = p_i + \frac{Q\mu}{4\pi kh}\int_{y=u}^{\infty}\frac{e^{-y}}{y}dy \qquad (2.2)$$

$$\text{where } u = \frac{\varphi \mu c_t r^2}{4kt}$$

In Equation 2.2, p_i is the initial reservoir pressure, Q is the volumetric flow rate, h is the thickness of the reservoir, and the integral expression is known as the Exponential Integral, Ei. Unknown system parameters, such as diffusivity and storativity, can be determined by matching the analytical solution to the pressure data, provided that the assumptions underlying Equation 2.2 are found acceptable. The pressure is recorded at the active well (injection/production) or an observation well during a flow or injection test.

Since the analytical solution proposed by Theis, techniques known as semi-log analysis and log-log analysis have been introduced. After a certain critical time, the slope and vertical intercept of the linear response on a semi-logarithmic plot of pressure versus time can be used to estimate reservoir parameters. The log-log plot, because it provides consistent characteristic shapes of different flow regimes (i.e. wellbore storage, during which time the wellbore itself influences the transient response, actual reservoir response, and reservoir boundaries), is used to diagnose the nature of the flow system. Finally, because logarithmic scaling compresses the later time, the pressure derivative curve has been introduced as an addition to the log-log analysis to amplify some of the details in the transient behavior. (Horne, 1995) The pressure derivative curve, however, will not be considered in this investigation.

2.2. Multilevel Pressure Monitoring

Unique to this investigation is that we evaluate multilevel pressure measurements in the storage reservoir, seal, and overlying aquifer (i.e. in all three zones). Our study encompasses pressure transients at multiple depths as well as normalized vertical pressure gradients. The basis for our simulation model is the Illinois Basin-Decatur Project in Illinois, where Schlumberger's Westbay multilevel monitoring system is placed in the monitoring well.

8

2.2.1. Background on Multilevel Monitoring Systems

A multilevel monitoring system allows the monitoring of a number of discrete zones in the subsurface (Cooper, 2011). The modern multilevel device (single well) is comprised of ports and packers at various locations along a casing string, effectively providing access to and isolating each monitoring interval (Cooper, 2011). This minimizes the disturbance of the formation by drilling fewer holes and reduces the cost per monitoring zone (Cherry et al., 2007).

The history of multilevel monitoring goes back to systems used in studies of groundwater contamination in permeable unconsolidated deposits (Merritt and Parsons, 1960; Pickens et al., 1978; Cherry et al., 1983). In the late 1970s, Westbay Instruments Inc. designed the first commercially available multilevel monitoring system suitable for fractured rock (Cherry et al., 2007). Cherry and Johnson (1982) developed a second type of multilevel monitoring system for fractured rock, which was then redesigned and made commercially available by Solinst Canada Inc. in the late 1980s (Cherry et al., 2007).

The earliest systems were designed for sample collection rather than full scale monitoring, including sampling, water level measurements, and permeability testing. Prior to advancements in multilevel systems, monitoring was enabled by drilling separate boreholes to different depths (cluster type installation), or by installing piezometers at various depths in a single borehole (nested type). The single borehole nested type piezometer installation was introduced to limit the disturbance of the aquifer and costs associated with drilling multiple boreholes (Cooper, 2011). However in 1986, the U.S. Environmental Protective Agency (EPA) stated that "Information obtained on multiple piezometer placements in a single borehole may generate erroneous data" (EPA, 1986). This was in response to uncertain seal placement resulting in possible interconnection between monitoring zones. The multilevel systems used today have resulted from a number of improvements and modifications. Packers have been engineered to provide high quality, reliable seals between monitoring zones, and removable packers have been introduced to allow for maintenance on the system and for complete removal when the site is decommissioned. Furthermore, multilevel systems can today be customized to suit

both the type of subsurface environment and specific goals of the investigation, as well as the allotted budget (Cooper, 2011).

The number of monitoring zones is ideally determined by the number of formation layers encountered during drilling but may be limited by the type of monitoring equipment and cost. Ultimately, cost determines the number, depth, and type of installation. Flexibility associated with the modular design of multilevel systems nevertheless allows for last minute modifications. For long term monitoring, multilevel systems can be installed with dedicated pressure transducers, which, in conjunction with a "datalogger," provide real-time continuous pressure data. (Cooper, 2011) According to Cooper (2011), vibrating wire pressure transducers offer greater stability than other transducer types.

2.2.2. Above-Zone Monitoring

While multilevel pressure monitoring in the context of CO_2 sequestration is a fairly new strategy, of which the effectiveness has yet to be thoroughly evaluated, several studies have considered above-zone pressure monitoring (i.e. monitoring in the aquifer overlying the seal), especially for the purpose of detecting or ruling out leakage through the seal (e.g. Chabora, 2009; Benson et al., 2006; Perry, 2005; Benson et al., 2002).

A study by Meckel and Hovorka (2010) compares pressure transient behavior in the above-zone to pressure transients in the storage reservoir. In particular, Meckel and Hovorka (2010) collected pressure data from a continuous industrial scale CO_2 injection project at an enhanced oil recovery (EOR) site at Cranfield Field, Mississippi. Continuous downhole high-precision pressure data was collected at a single monitoring well at two depths; in the injection interval and in a selected above-zone monitoring interval (AZMI). The AMZI is a sandstone layer above the storage reservoir and above a thick confining formation (seal). The monitoring well is a 40-50 year old abandoned well that has been refitted for monitoring purposes. The two pressure gauges monitor storage reservoir and above-zone pressure perturbations related to activities at seven injection wells, nine production wells, and other potentially contributing abandoned wells in the area (Meckel and Hovorka, 2010).

A significant pressure buildup was sustained for the entire injection period (more than two years), reaching a maximum of 8.8 MPa, however the pressure trends and transients observed in the injection interval due to varying injection rates were not apparent in the AZMI data. The pressure buildup in the AZMI was less than 0.7 MPa. Arrival of CO_2 was seen at the monitoring well as an increase in tubing pressure due to CO_2 replacing brine from the tubing volume, which Meckel and Hovorka (2010) note is "an entirely expected signal." Formation pressure response appeared unaffected by the arrival of the CO_2, both in the injection interval and in the AZMI. (Meckel and Hovorka, 2010)

In spite of the AZMI data showing significant amounts of noise, the results reported suggest that above-zone monitoring can serve as a robust tool for evaluation communication between formations during CO_2 injection. In this case, AZMI pressure (and temperature) data indicated first-order isolation (i.e. no pressure communication) between the injection zone and the above-zone. (Meckel and Hovorka, 2010)

Zeidouni and Pooladi-Darvish (2010) present an inverse method to detect and characterize leakage pathways through a seal based on transient pressure measurements at a monitoring well in the above-zone (separated from the storage reservoir by a seal). Single-phase one-dimensional radial flow is assumed in the aquifers. The leakage occurs in the vertical direction through a single leakage point, the aquifers are considered infinite, and the injection rate is set to be constant. The authors consider 2,400 pressure measurements with a sampling frequency of one measurement per hour. While little information can be obtained on the leak location due to a wide confidence interval for acceptable leak locations, the leak transmissibility can be evaluated within a narrower confidence interval (Zeidouni and Pooladi-Darvish, 2010).

2.2.3. Pressure Response in Stratified Systems

Birkholzer et al. (2008) examine the large-scale impact of CO_2 sequestration in deep saline aquifers by conducting a sensitivity study on pressure response in stratified systems. The storage of additional fluids in a reservoir, such as CO_2, may result in pressure changes and brine displacement that affect subsurface volumes considerably

larger than the volume of the CO_2 plume itself (Birkholzer et al., 2008). Birkholzer et al. (2008) conduct numerical simulations using TOUGH2/ECO2N (see Sections 3.1 and 3.2 for details on TOUGH2/ECO2N), and let the model domain be that of an idealized multilayered groundwater system, with a sequence of aquifers and aquitards (seals) extending from the deep saline storage formation to the uppermost freshwater aquifer. The seal permeabilities are varied from 1.0E-16 to 1.0E-21 m^2. The storage reservoir itself is homogeneous and isotropic. Due to buoyancy forces, the CO_2 migrates upward until it reaches the seal. Then, for seal permeabilities < 1.0E-16, the CO_2 flows laterally, forming the characteristic shape of a "gravity tongue." Water flux vectors indicate that the brine ahead of the CO_2 plume flows mainly horizontally (slight upward incline immediately in front of the plume), whereas in the plume area, buoyant CO_2 migration generates a downward component of brine flow (Birkholzer et al., 2008).

For the pressure buildup examination, the seal permeabilities are varied from 1.0E-17 to 1.0E-20 m^2. The pressure buildup in the entire vertical sequence of strata is examined after 30 years of CO_2 injection. In cases with relatively high seal permeability, brine leaking upward from the storage reservoir has a positive attenuation effect on the pressure conditions within the storage reservoir, allowing for vertical pressure propagation (Birkholzer et al., 2008). For the low-permeability case (10E-20 m^2), there is an significant pressure increase extending out much farther laterally within the storage formation, but no significant pressure buildup above the lower portion of the seal immediately above the storage formation (Birkholzer et al., 2008). Birkholzer et al. (2008) have chosen set a cutoff of 0.1 bar (0.01 MPa) for the pressure contours displayed in the paper.

2.3. Measurement Sensitivity and Practical Considerations

At Cranfield Field, Mississippi, where data has been collected for more than a year during continuous industrial-scale CO_2 injection at an EOR site (starting July 2008), monitoring and injection zones were instrumented with Panex© model 6250 digital SRO (Surface Read-Out) quartz pressure and temperature gauges (Meckel and Hovorka, 2010). The pressure resolution was 0.01 psi (6.895E-5 MPa) (Meckel and Hovorka, 2010).

12

According to Zeidouni and Pooladi-Darvish (2010), who present an inverse method to detect and characterize leakage pathways through a seal based on pressure data, the pressure measurement error may significantly affect the parameter estimation, in particular when the pressure signal is small. Zeidouni (2010) discusses the characteristics of the error in the pressure data given current pressure transducer technology and environmental sources of error. It is believed, based on this discussion, that a high-quality pressure signal with a resolution of 0.01 psi may be obtained using a resonant quartz gauge (Zeidouni and Pooladi-Darvish, 2010).

Chabora (2009) has pointed out that pressure gauge accuracy, long-term repeatability and stability of the instrument, and naturally occurring subsurface pressure fluctuations all need to be considered alongside pressure gauge resolution in the context of long-term monitoring of injected CO_2. Whereas resolution refers to the smallest incremental pressure change that the gauge can discern, accuracy is a measure of the error between the measured value and the true value (Chabora, 2009). Repeatability denotes the error between consecutive pressure measurements performed under identical conditions, and stability refers to the consistency of the gauge over time with respect to its calibration criteria (Chabora, 2009).

Because we are concerned with the change in pressure from initial reservoir conditions, high resolution, repeatability, and stability are more important than absolute accuracy (Chabora, 2009). Chabora (2009) constructed a table providing a coarse overview of typical specifications and operating limits of permanent downhole gauges based on data sheets from Schlumberger and Halliburton (Table 1).

Table 2.1: Typical performance specifications of permanent downhole gauges (Table 2.1 in Chabora, 2009).

Range (psi)	Resolution (psi)	Accuracy (psi)	Repeatability (psi)	Stability (psi/year)
14.7 – 16,000	0.01	$< \pm 3$ (full scale)	$< \pm 2$ (full scale)	± 1 @ 12,000 psi
14.7 – 25,000	0.008	$< \pm 4$ (full scale)		± 5 @ 25,000 psi

In addition to gauge performance, there is a practical detection threshold to consider. For instance, a change in pressure of 0.1 psi over a week may be detectable whereas the same change over a year may be on the order of the drift of a typical gauge and not possible to discern. The practical threshold for positive detection will ultimately be determined by a combination of in-situ conditions at the storage site, instrument specifications, and industry experience with the instruments used. The minimum possible detection threshold may in practice extend up to 0.1 or 1 psi. (Chabora, 2009)

Natural fluctuations that may contribute to pressure changes observed over a long-term monitoring period include Earth tide fluctuations (changes in periodic stress in the Earth's crust due to gravitational interaction with other planets), whose peak-to-through magnitudes vary from 0.03 to 0.3 psi, changes in barometric pressure (~1 psi), and precipitation (~1 psi) (Chabora, 2009).

For the purpose of this investigation, we assume a minimum pressure buildup detection (resolution) of 0.001 MPa (0.145 psi).

Chapter 3

3. Investigative Approach

3.1. Overview

The goal of this study is to evaluate the effectiveness of vertically distributed pressure monitors. In order to do so, a geologic model is constructed that can be subjected to various combinations of heterogeneity/homogeneity and anisotropy/isotropy conditions to see how the migration of the CO_2 plume and resulting brine displacement vary and what the corresponding pressure responses are. Given the complexity of geologic systems represented and the physical processes described, numerical modeling is the best approach for this investigation.

A common simulation tool used by the CCS community is the TOUGH2 simulation program with the ECO2N equation of state (EOS) module (IPCC, 2005; Benson et al., 2004; Doughty et al., 2002). TOUGH2 is a numerical simulator developed at the Lawrence Berkeley National Laboratory (LBNL) Earth Sciences Division for nonisothermal multicomponent, multiphase fluid flow in one, two, and three-dimensional porous and fractured media (Pruess et al., 1999). ECO2N is a fluid property algorithm specifically designed to represent the thermodynamics and thermophysical properties of CO_2-H_2O-NaCl systems (Pruess, 2005). Due to its wide use in CO_2 sequestration research and its ability to capture the physical process of CO_2-brine systems in porous media, the numerical modeling in this study is performed in TOUGH2/ECO2N. The PetraSim software package is used as a pre- and post-processing interface to the TOUGH2/ECO2N algorithm (Alcott et al., 2006). PetraSim allows the user to easily construct a simulation mesh, input data, and manipulate system parameters.

In order to keep the investigation of the CO_2 migration and resulting water displacement manageable, the study is limited to four basic scenarios for the constructed geologic system: 1) homogeneous and isotropic, 2) homogeneous and anisotropic, 3) heterogeneous and isotropic, and 4) heterogeneous and anisotropic. For practical

purposes, the fourth scenario is the most realistic scenario, as every real reservoir will have some degree of heterogeneity and anisotropy.

3.2. Details of the TOUGH2/ECO2N Algorithm

The TOUGH2 algorithm (Appendix A in Pruess et al., 1999) is based on basic mass and energy equations that in the general form can be written as

$$\frac{d}{dt} \int_{V_n} M^\kappa dV_n = \int_{\Gamma_n} \mathbf{F} \cdot \mathbf{n} \, d\Gamma_n + \int_{V_n} q^\kappa dV_n \qquad (3.1)$$

In Equation 3.1, the integration is performed over an arbitrary subvolume V_n of the given flow system, where V_n is bounded by a closed surface Γ_n. The quantity $\mathbf{F}$ in the net flux term on the right hand side denotes mass or heat flux, and $\mathbf{n}$ is the inward-pointing normal vector on surface element $d\Gamma_n$. The quantity q (mass flow rate) represents any sink or source terms within the control volume V_n. The quantity M that appears in the accumulation term on the left hand side represents either mass or energy per unit volume, with the superscript κ indicating the component (e.g. H_2O or CO_2) ($\kappa = 1, \dots, \text{NK}$). The general form of the mass accumulation term is given by

$$M^\kappa = \varphi \sum_\beta S_\beta \rho_\beta X_\beta^\kappa \qquad (3.2)$$

where the total mass of component κ is obtained by summing the concentrations of κ in each fluid phase β (e.g. liquid, gas phase). The symbol φ represents porosity, S is the saturation, ρ is the density, and X is the mass fraction. Similarly, the heat accumulation term is expressed in the general form

$$M^{NK+1} = (1 - \varphi)\rho_R C_R T + \varphi \sum_\beta S_\beta \rho_\beta u_\beta \qquad (3.3)$$

where ρ_R is the grain density, C_R is the specific capacity of the rock, T is the temperature, and u is specific internal energy. The total advective mass flux $\mathbf{F}^\kappa$ across Γ_n is given as a sum over the individual phases:

16

$$\mathbf{F}^\kappa = \sum_\beta X_\beta^\kappa \mathbf{F}_\beta \qquad\qquad (3.4)$$

The individual phase fluxes are determined by a multiphase version of Darcy's law:

$$\mathbf{F}_\beta = -k \frac{k_{r\beta}\rho_\beta}{\mu_\beta}\left(\nabla P_\beta - \rho_\beta \mathbf{g}\right) \;, \qquad\qquad (3.5)$$

where k is the absolute permeability, k_r is the relative permeability to phase β, μ is viscosity, and $\mathbf{g}$ is the vector of gravitational acceleration. The fluid pressure in phase β, P_β, is defined as the sum of the pressure P of a reference phase (usually the non-wetting or gas phase) and the capillary pressure P_c (≤ 0) between the reference phase and phase β:

$$P_\beta = P + P_{c\beta} \qquad\qquad (3.6)$$

By applying Gauss's divergence theorem, Equation 3.1 can be converted to the following PDE:

$$\frac{\partial M^\kappa}{\partial t} = -\nabla \mathbf{F}^\kappa + q^\kappa \qquad\qquad (3.7)$$

The PDE in Equation 3.7 is used as the starting point for a finite element discretization of the governing equations. The TOUGH2 algorithm is based on the integral finite difference (IFD) method (Narasimhan and Witherspoon, 1976; Pruess, 1987, 1991), where the governing equations are discretized in space using the IFD method and in time using a fully-implicit first-order backward finite difference scheme (Zhang et al., 2008). The resulting nonlinear discrete finite difference equations for mass and energy are solved simultaneously by the Newton-Raphson method (Zhang et al., 2008).

The equations that govern multiphase mass and heat flow will always have the same mathematical form (Pruess et al., 1999). The nature of the specific fluid mixture in question enters into the governing equations through thermophysical parameters (e.g.

fluid density, viscosity) (Pruess et al., 1999). The thermophysical parameters are provided by an appropriate Equation of State (EOS) module (Pruess et al., 1999).

The ECO2N module is the fluid property module designed for applications of geologic sequestration of CO_2 in saline aquifers (Pruess, 2005). The ECO2N module is founded on experimentally based correlations of Spycher and Pruess (2005) and describes the thermodynamics and thermophysical properties of CO_2-H_2O-NaCl systems (Pruess, 2005). The flow process may be modeled isothermally or nonisothermally, and the phase condition may be aqueous or CO_2-rich single phase, or a two-phase mixture consisting of an aqueous and a single CO_2-rich phase (Pruess, 2005). Over the course of a simulation, a fluid phase may appear or disappear, and the ECO2N module can also treat precipitation of solid salt (Pruess, 2005).

3.3. Geologic Description

The simulation study is based on the Illinois Basin-Decatur demonstration project at ADM's facilities in central Illinois, where a total of one million metric tons of CO_2 will be injected into the Mt. Simon Sandstone over three years. The overlying Eau Claire Formation is expected to comprise the primary seal.

The Mt. Simon Sandstone is Cambrian in age and part of the Illinois Basin. The Illinois Basin is a 155,000 km^2 oval depression that extends under Illinois, southwestern Indiana and western Kentucky (Buschbach and Kolata, 1991). In particular, the Illinois Basin is an interior cratonic basin that resulted from a number of subsidence events and marginal uplifts (Macke, 1995). Today, the basin contains about 450,000 km^3 of primarily Cambrian through Pennsylvanian sedimentary rocks (Buschbach and Kolata, 1991).

A major unconformity exists between the Precambrian crystalline rocks (commonly referred to as the basement) and the overlying Cambrian sedimentary rocks (Atherton, 1975; Buschbach., 1975; Bickford et al., 1986). The basal unconformity is marked by the absence of late Precambrian and Early/Middle Cambrian rocks (Willman, 1975). The Precambrian crystalline rocks consist mostly of granite, rhyolite, and granodiorite (Buschbach and Kolata, 1991). A terrain of distinct topographic relief developed as a result of subaerial erosion (Buschbach and Kolata, 1991).

18

The sequences represented in the Illinois Basin include (from oldest to youngest) the Sauk, the Tippecanoe, the Kaskaskia, the Absaroka, the Zuni, and the Tejas (Kolata, 1991). Initial Cambrian deposition seems to have been nearly continuous with deposition of the rest of the overlying Sauk Sequence (Cambrian System through Lower Ordovician) (Macke, 1995). Deposition of the Sauk Sequence began mainly as siliciclastic deposition and ended with predominantly carbonate rock deposition (Macke, 1995).

After the rifting period and through most of the Paleozoic Era, the Illinois Basin area was an open-marine cratonic embayment. In contrast to what is typical for interior cratonic basins, no salt accumulated in the basin except for some small, local amounts of anhydrate (Kolata, 1991).

At the end of the Early Ordovician time, relative sea level dropped, and subaerial erosion began (Kolata, 1991). As a consequence, deposition of the Sauk sequence ceased (Kolata, 1991). East of the basin more than 31 m of relief developed, suggesting that arid conditions existed (Patton and Dawson, 1969). Prior to deposition of the Tippecanoe sequence, a terrain of predominantly carbonate rocks was exposed for about 10 to 15 million years (Kolata, 1991). Major tectonic events that occurred after the Illinois Basin had evolved into a cratonic embayment led to structural closure and the geometry that we see today (Buschbach, 1991).

More than 50 percent of the rock in the Illinois Basin is dolomite or limestone, close to 25 percent is sandstone, and the remainder consists of shale, siltstone, chert, and smaller amounts of anhydrite (Buschbach and Kolata, 1991). The stratigraphic units tend to thicken southward toward the rift complex (Buschbach and Kolata, 1991).

Present-day geothermal gradients obtained from a selection of deep wells in the deepest part of the Illinois basin range from 1.51°C to 2.31°C/100 m (Davis, 1991). The arithmetic mean is 1.88°C/100 m (Davis, 1991).

3.3.1. Mt. Simon Sandstone

Throughout the Middle Cambrian time, the dominant influence on deposition was faulting associated with rift formation (Houseknecht and Weaverling, 1983), but by Late Cambrian time rifting had ceased, and the rift complex and surrounding cratonic area

began to sag (Howe and Thompson, 1984). Around this time sea level also started to rise, and the Mt. Simon Sandstone was deposited on the Precambrian basement rock (Sargent, 1991). As the relative sea level continued to rise and as the sediment cover extended farther onto the craton, local sources of sediment became less influential (Houseknecht and Ethridge, 1978). The shoreline advanced northward, and most of the Mt. Simon Sandstone was deposited in a shallow, subtidal sea (Droste and Shaver, 1983). A marine setting of the Mt. Simon is also suggested by the presence of marine trace fossils (Fishman, 1997).

During the time of Mt. Simon Sandstone deposition, "the tectonic setting of the proto-Illinois Basin was that of a broad, slowly subsiding cratonic basin open to the south" (Fishman, 1997). In northeastern Illinois, local sag led to thick (>750m) accumulations of Mt. Simon Sandstone; elsewhere the Mt. Simon Sandstone is significantly thinner (Fishman, 1997). The local sag in northeastern Illinois seems to have lasted only during deposition of the Mt. Simon Sandstone since the overlying Eau Claire Formation is relatively uniform in thickness across this area (Fishman, 1997). Though no wells have penetrated the Precambrian basement in a large area consisting of central and east-central Illinois, west-central and southwestern Indiana, and western Kentucky, a number of wells, drilled either for gas storage or for waste disposal, penetrate thick sections of the Mt. Simon (Sargent, 1991). Hence, even though the wells fail to provide full stratigraphic thicknesses, they at least provide minimum thickness data for the Mt. Simon Sandstone (Sargent, 1991).

The Mt. Simon Sandstone is very fine to coarse grained and partly pebbly, and characterized by poor sorting and the presence of coarse to extra coarse sand in graded cross-stratified beds (Buschbach, 1975; Fishman, 1975). Variations in wave energy most likely caused the variations observed in size, sorting, and composition of the detrital grains (Fishman, 1997). This variability occurs both within cross bed laminae as well as within cross-bed sets (Fishman, 1997). Sorting within the sandstone ranges from good to poor, and the Mt. Simon is typically a quartzite or a subarkose, depending on grain size (Fishman, 1997). Fine to medium grained sandstone tends to be more arkosic (largely due to more detrital K-spar), whereas coarse grained sandstone tends to be quartzose (Fishman, 1997). Mt. Simon also contains beds of red and green micaceous shales

(Buschbach, 1975). Feldspar is abundant only in the deeper arkosic zones toward the base of the formation and near source areas on the Wisconsin arch and Ozark dome (Sargent, 1990). Elsewhere, the Mt. Simon is more quartz-rich and rounded (Sargent, 1991).

The Mt. Simon Sandstone was a likely conduit for passage of basinal brines, possibly multiple times during its diagenetic history (Fishman, 1997). Migration of warm (>100ºC) and saline (>20 wt percent NaCl equivalents) basinal brines through the Mt. Simon Sandstone resulted in formation of quartz overgrowths as suggested by fluid inclusions in the quartz (Fishman, 1997).

Authigenic quartz is the most common and volumetrically significant cement in the Mt. Simon Sandstone (Fishman, 1997). Carbonate, mainly dolomite, can locally comprise up to 20 percent of the rock volume but is for the most part a very minor cement (Fishman, 1997). When present, the dolomite occurs as poikilotopic cement, cementing earlier-formed authigenic K-spar and a good portion of the quartz overgrowths (Fishman, 1997).

Textural features indicate that Mt. Simon has undergone compaction; however the degree of compaction is variable (Fishman, 1997). Samples containing abundant quartz cement show evidence of compaction, and it is therefore likely that significant burial occurred prior to the formation of quartz overgrowths (Fishman, 1997).

Similarity in the diagenetic history for the Mt. Simon Sandstone across the study area considered by Fishman (1997) suggests that fluids traveled far and altered the formation in a similar fashion across the region. The mechanism responsible for driving the fluid flow through the Mt. Simon Sandstone must have been sufficient to sustain flow over significant periods of time such that alterations including quartz and K-spar cementation could occur possibly episodically (Fishman, 1997). Regional paleofluid flow through the formation must have occurred several times during the post-depositional history of the sandstone as a number of cements precipitated and some of them subsequently dissolved (Fishman, 1997).

3.3.2. Eau Claire Formation

Through most of the Illinois Basin the Eau Claire was unconformably deposited upon the Mt. Simon Sandstone (Sargent, 1991; Fishman, 1997). The Eau Claire constitutes today the primary seal over Mt. Simon. In the northern part of the Illinois Basin, the Eau Claire is dominated by siltstones and sandstones with some interbedded dolomite and dolomitic siliciclastics (Buschbach, 1975). Toward the south, the siliciclastics grade to carbonate rocks (Sargent, 1990). The Eau Claire is about 90 m thick in the northwestern part of the basin (Buschbach, 1975) but thickens toward the south and southeast to more than 685 m in the Reelfoot rift (Sargent, 1991). In the deepest parts of the Rough Creek graben, the Eau Claire exceeds 825 m (Sargent, 1991).

3.3.3. Ironton-Galesville Sandstone

The Eau Claire Formation is overlain by Galesville Sandstone (Sargent, 1991). Galesville is 12 to 30 m thick and can be traced as far south as southeastern Vermilion County and southern Christian County, Illinois (Buschbach, 1975), and into northwestern Indiana (Droste and Patton, 1985). The presence of sandstone and basal disconformity suggests there was a substantial regression prior to its deposition (Sargent, 1991). As Galesville and the overlying Ironton Sandstone were deposited, the present northern end of the basin remained a shallow subtidal environment (Droste and Shaver, 1983). The Galesville Sandstone is characterized by fine-grained sandstone (Buschbach, 1964), but the sand coarsens upward to the top of the Ironton Sandstone, which is composed of medium to coarse grained, poorly sorted, white quartz sandstone (Sargent, 1991). The Ironton and Galesville sandstones grade laterally southward into dolomite, and in the north-central part of the basin, south of central Illinois, they become an indistinguishable part of the Knox Supergroup (Buschbach, 1975). In the northern part of the basin, the Franconia is present above the Ironton-Galesville. In the remainder of the basin, the Franconia is present directly above the Eau Claire Formation (Sargent, 1991). Ironton-Galesville, with the exception of where the Franconia Formation takes over, composes the first high permeability unit over the Eau Claire Formation.

3.3.4. Decatur Region

In the Decatur region, bedded sedimentary rocks (mainly limestone, dolomite, sandstone, and shale) extend down to a depth of 1,500 to 2,000 m (Bergstrom et al., 1976). Pennsylvanian rocks comprise the uppermost bedrock throughout the region (Bergstrom et al., 1976). The sedimentary rocks thicken and dip to the southeast, whereas the base of the Precambrian crystalline rocks slopes slightly to the southeast toward the center of the Illinois Basin (Bergstrom et al., 1976).

The character, thickness, and structure of the rocks are known from a number of well penetrations that have been made in search of ground water and mineral deposits (Bergstrom et al., 1976). In nearby areas of Illinois, oil exploration holes have penetrated the entire section of sedimentary rocks and reached the top of the Precambrian crystalline rocks (Bergstrom et al., 1976). Because there are zones in the Mt. Simon Sandstone that are relatively porous, it is used or has been tested at several places in Illinois (Ancona, Crescent City, Herscher, Mahomet, Pontiac, Troy Grove, Tuscola, and McLean County) for the storage of natural gas to match supply and demand (Bergstrom et al., 1976). Besides requiring a porous rock for the reservoir, a gas storage project requires a caprock to vertically and laterally confine the gas, such as the Eau Claire Formation, which contains shale units that are believed to retard vertical fluid movement (Bergstrom et al., 1976).

In the thick Mt. Simon Sandstone the water is brine, likely containing more than 100,000 ppm total dissolved minerals (Bergstrom et al., 1976).

Table 3.1 lists the approximate thicknesses and rock types of the formations of interest in the Decatur region.

Table 3.1: Section of unconsolidated deposits and bedrock in the Decatur region; modified from Figure 12 in Bergstrom et al. (1976).

System	Series	Group or Formation	Thickness (m)	Description
Cambrian	Croixan	Ironton-Galesville	~15-46	Sandstone; thin dolomite at top
		Eau Claire	~129-168	Siltstone, limestone, dolomite, and shale
		Mt. Simon	~229-549	Sandstone
Precambrian				Granite and other igneous rock

3.3.5. Weaber-Horn # 1 Well

At the time of the initiation of this investigation, data from the ADM site was not available. We therefore based the stratigraphic layers in our geologic model on a sonic porosity log from the Weaber-Horn # 1 well, located in the Loudon Field Anticline in Fayette County, Illinois, roughly 100 km south of the ADM injection site (Figure 3.1).

The Weaber-Horn # 1 well has been used in the literature (e.g. Birkholzer, 2009; Zhou et al., 2009) and a Weaber-Horn well has also been used by the Illinois Basin-Decatur Project (e.g. Finley, 2010) as a predictor for the stratigraphy at the ADM site in Decatur. Even though Weaber-Horn is located about 100 km south of the site of interest, in a deeper section of the Illinois Basin (see Figure 3.1), the basic stratigraphy is expected to be similar.

The sonic porosity at Weaber-Horn # 1 has been measured every 0.15 m from an elevation of 966 m to 2621 m below the surface (Birkholzer, 2009; Zhou et al., 2009). Figure 3.2 shows the vertical profiles (gray lines) of sonic porosity and the corresponding calculated horizontal permeability for Weaber-Horn # 1 (Birkholzer, 2009). In the analysis by Birkholzer (2009), "the observed depositional variability in rock properties within the Mt. Simon was incorporated into the model using 24 hydrogeologic layers;" these are shown in red in Figure 3.2.
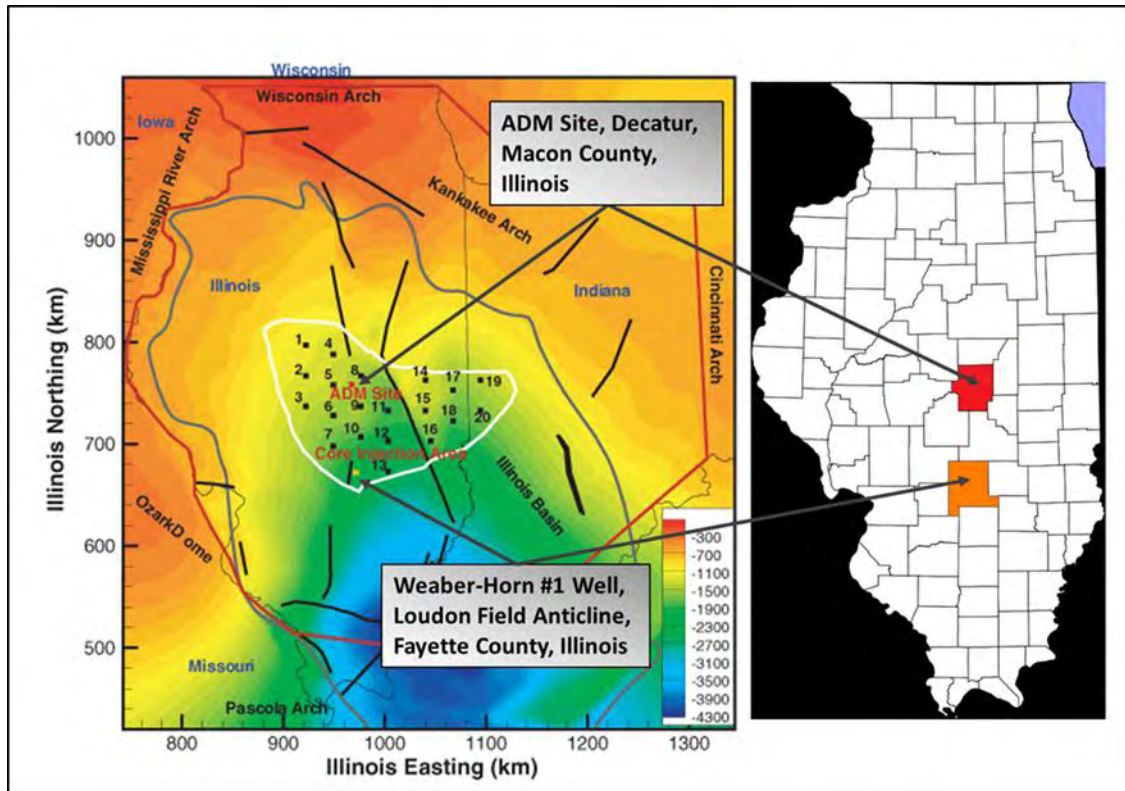
Figure 3.1: Geographic locations and elevation map of the Illinois Basin. Left: Overview of the Illinois Basin as bounded by arches and domes, with contour plot representing the top elevation (m) of the Mt. Simon Sandstone. State borders are marked by thin, black lines, the Illinois Basin boundary is marked by a gray line, and faults and anticlines are marked by thick, black lines. The ADM site is shown as a red square and Weaber-Horn #1 is shown as a yellow square. (Modified from Figure 1 in Zhou et al., 2009). Right: Map of Illinois (modified from Benbennick, 2006).

3.4. Model Description

We use the estimated porosity and horizontal permeability values presented by Birkholzer (2009) and Zhou et al. (2009) as a basis for the simulation model in TOUGH2/ECO2N. However, instead of 24 layers, we let the Mt. Simon storage reservoir consist of 23 layers. This decision is based on a visual estimation of the porosity and horizontal permeability values presented in Figure 3.2. For the Eau Claire Formation we make similar estimates, letting the Eau Claire Formation be comprised of six distinct layers. For the overlying aquifer no data was available; for simplicity we let this aquifer be represented by a uniform sandstone layer having the same characteristics as estimated

for the lowermost layer of the Mt. Simon Sandstone (making no attempt to represent the Ironton-Galesville in this study). Extending from 1935 to 2535 m below the surface, the height of the combined system is 600 m.
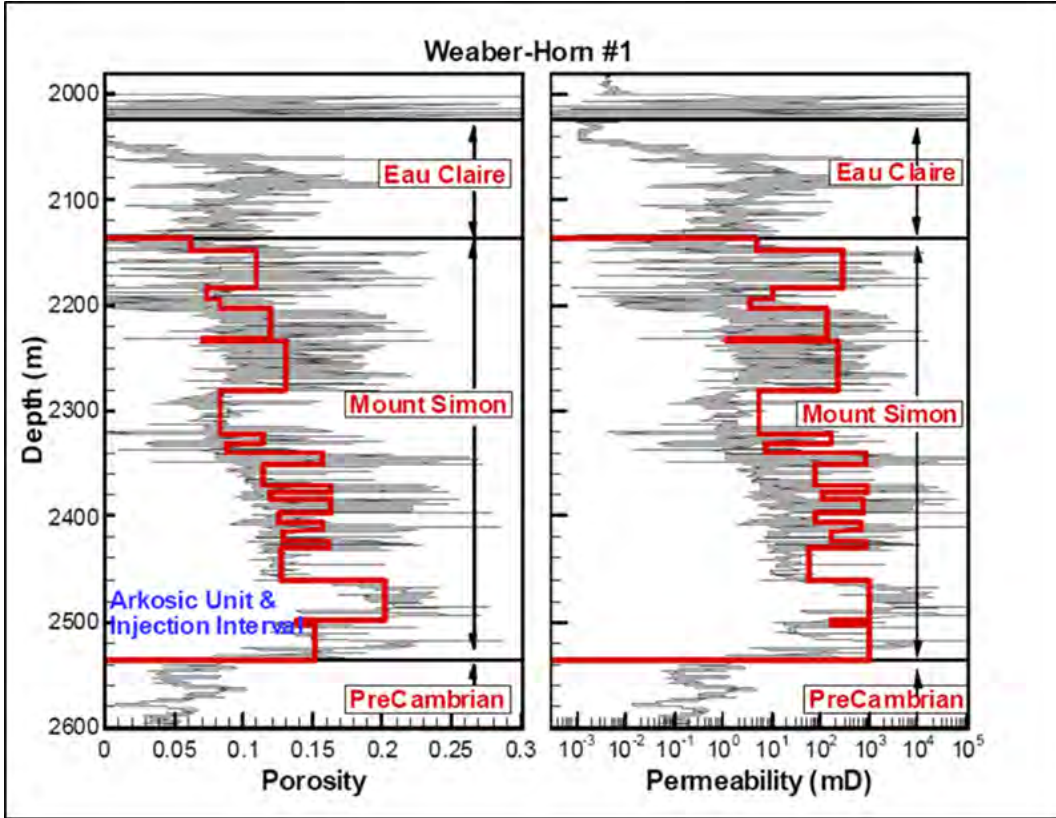
Figure 3.2: Vertical profiles of sonic porosity and horizontal permeability (md) (gray lines) for the Weaber-Horn # 1 well. Shown in red are the average porosity and permeability values for the 24 Mt. Simon hydrogeologic layers as defined by Birkholzer (2009). (Figure 3 in Birkholzer, 2009.)

3.4.1. Basic Mesh Architecture

Two concerns need to be addressed before a proper simulation mesh can be constructed. First, the geometry has to represent a geologic setting of 30 vertically stacked layers. Second, the migration of the CO_2 plume (saturation) will be captured more precisely with a finer grid, whereas the pressure, due to the elliptic nature of the diffusion equation, can be captured just as satisfactorily with a coarser grid.

The first concern is with regard to how to best represent the 30 distinct layers. The height of the thinnest layer is estimated to 5 m, whereas the height of the thickest layer (the overlying aquifer) is estimated to 85 m. In order to maintain a fine grid resolution, we let the grid cells be 5 m in the vertical direction.

Comparisons in the literature of well data from the ADM site with well data obtained from Weaber-Horn and another well in the region, Hinton # 7, suggest a large degree of lateral continuity across more than 100 km in the Illinois Basin (Finley, 2010). Hence, it is reasonable to assume lateral homogeneity for each layer. Figure 3.3 provides a simple schematic of the 30-layer geologic model.

The second concern is with regard to the grid size distribution in the horizontal direction. Two key processes to consider are the migration of the CO_2 plume and the pressure propagation through the reservoir. Whereas the migration of the CO_2 plume (saturation) will be captured more precisely with a finer grid, the pressure, due to the elliptic nature of the diffusion equation, can be captured with a coarser grid. Because the region close to the CO_2 injection is the most dynamic region in the reservoir, the grid cells here need to be small to capture the subtle changes in CO_2 saturation during simulation. Further away from the injection well, the reservoir is not expected to show much change in pressure or CO_2 saturation during the time of the simulation. The grid cells on the perimeter of the reservoir may therefore be larger. In addition, it is important that the dimensions of the model are large enough that the boundaries do not affect the pressure distribution during the time of simulation.

A radially symmetric (rz) grid is selected because it is suitable for the case where the individual layers are continuous and there is injection into a single well. Table 3.2 shows the number of cells and cell size for the vertical and radial directions. As shown in Figure 3.4, the reservoir extends out 100 km radially, and the radial distance from the injection well to the monitoring well is set to 255 m. The resulting mesh architecture should be reasonable in terms of geology and physics, as well as in terms of computational efficiency.
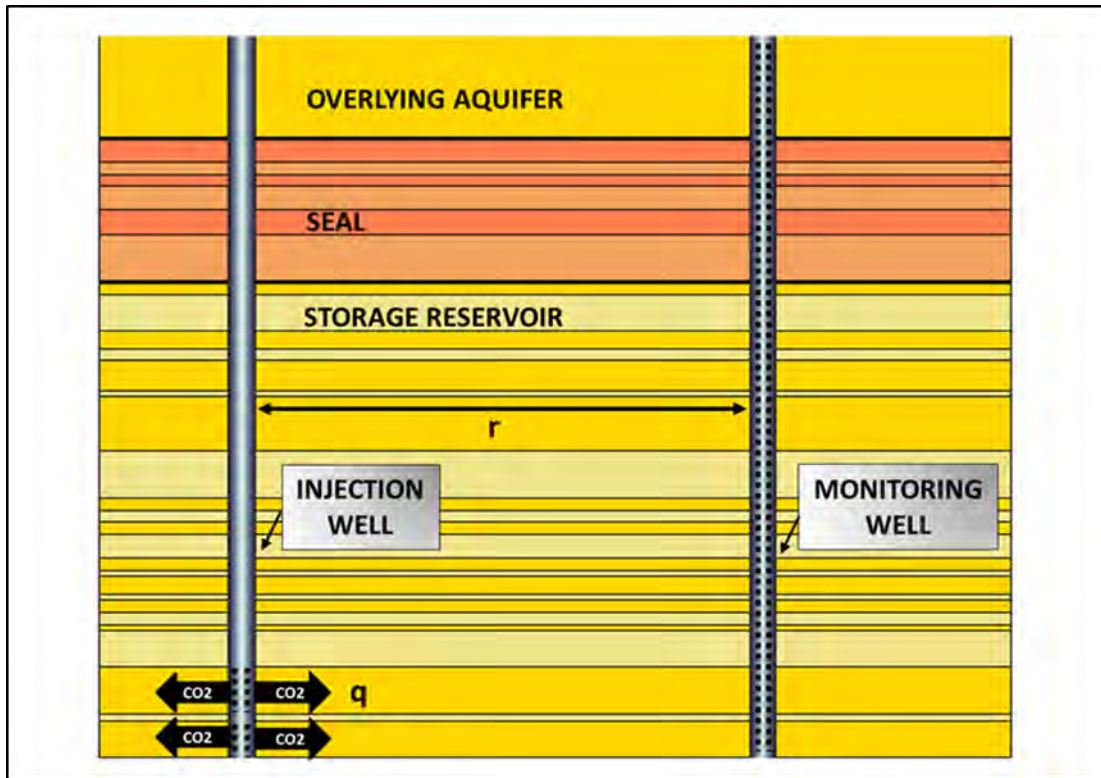
Figure 3.3: Simple schematic of the 30-layer geologic model (23-layer storage reservoir, six-layer seal, and one-layer overlying aquifer). Note that this schematic only illustrates the distinct layers and not the actual grid cells.

Table 3.2: Meshmaker rz. The number of grid cells in the radial and vertical directions is shown as well as the respective grid cell sizes.

Direction	Number of cells	Size (m)
r	5	0.2
r	5	1.8
r	10	9.0
r	20	10.0
r	7	100.0
r	5	1,800.0
r	5	18,000.0
z	120	5.0
Total number of cells: 6,840		
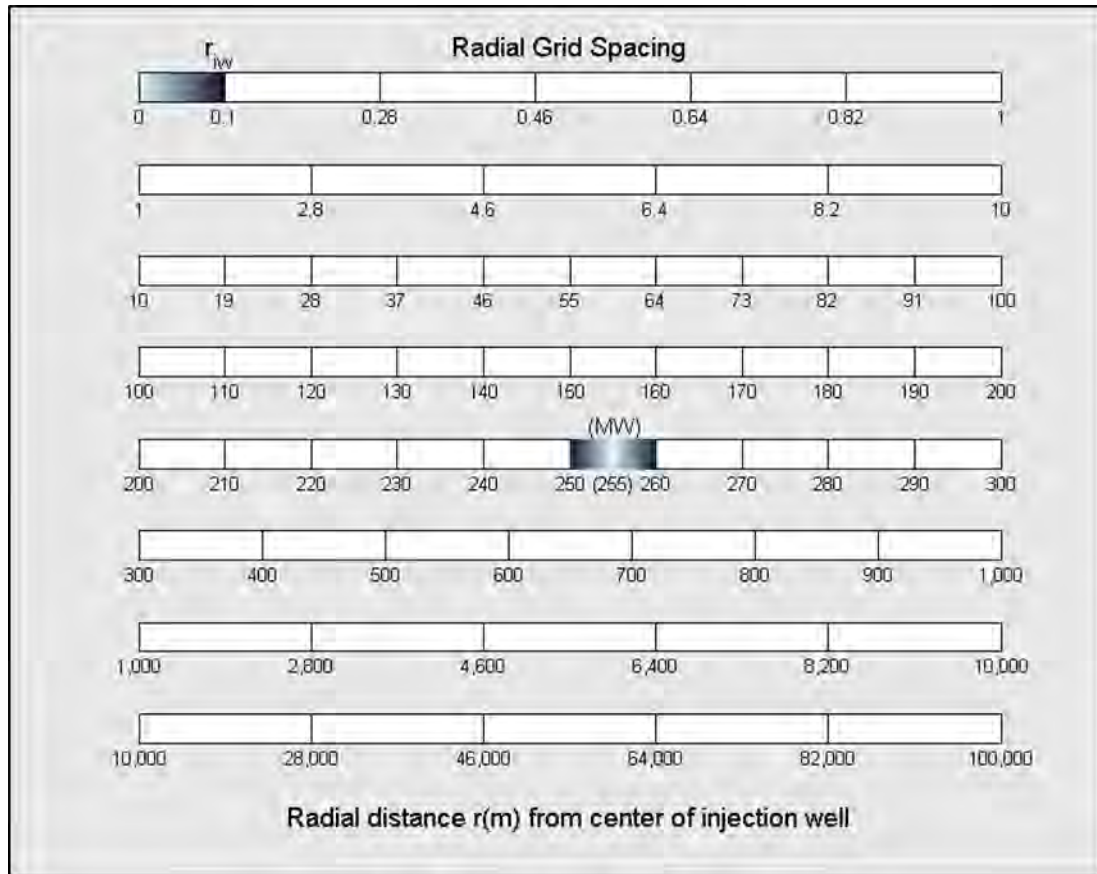
Figure 3.4: Illustration of the radial grid spacing, where r_{iw} denotes the radius of the injection well and MW denotes the position of the monitoring well (both in terms of the actual position of 255 m from the center of the injection well and in terms of cell position (250-260m). Every grid cell is 5 m in the vertical direction.

3.4.2. Geologic and Fluid Parameters of the System

Since no data was available for the overlying aquifer, we assumed the overlying aquifer has the same geologic characteristics as the lowermost layer in the Mt. Simon Sandstone. Important parameters of the three different zones (storage reservoir, seal, and overlying aquifer) are summarized in Table 3.3. Layer thickness h is estimated from Figure 3.2, rock density ρ_R is obtained from Finley (2010), values for rock compressibility c_R are obtained from the literature (Zhou et al., 2009), and the values for heat capacity C and heat conductivity K are based on typical values observed throughout the literature. The remaining geologic parameters, porosity φ and permeability k, are listed in Tables 3.4

and 3.5, where the (horizontal) permeability distributions for the heterogeneous scenarios are estimated from Figure 3.2.

For the cases where the reservoir is both heterogeneous and anisotropic, the following approach to assigning parameters is used. Due to the availability of only horizontal permeability values from the literature, we estimated an anisotropy value of 0.04 for the storage reservoir due to the high degree of heterogeneity within each of the layers (within the typical range for anisotropy of 0.01 to 0.1 provided in the literature for reservoirs), and a fairly low anisotropy of 0.004 for the seal.

For the homogeneous anisotropic scenario, the horizontal permeability is the arithmetic mean permeability and the vertical permeability is the harmonic mean permeability. For the homogeneous isotropic case, we assumed that flow in the reservoir is mainly horizontal and that flow in the seal is mainly vertical. In this case the permeability in the seal is the same as the vertical permeability in the seal for the homogeneous anisotropic case, and the permeability in the reservoir is the same as the horizontal permeability in the reservoir for the homogeneous anisotropic case. For the homogeneous cases, the porosity is the arithmetic mean porosity in the seal and reservoir, respectively. For the homogeneous cases, the rock density is an arithmetic mean of 2400 kg/m^3.

Based on a typical hydrostatic gradient of 10 MPa/km, we initialized the base of the storage reservoir (depth of 2535m) to 25.35 MPa and let the system equilibrate for 100 years before we started the injection. For simplicity, the system is isothermal, with a temperature of 60 ºC, and we also neglect the salinity of the system and instead focus on a pure CO_2-water system.

Table 3.3: Geologic parameters used in simulation model

Zone	Matrix	Layer	h(m)	$\rho_R \left(\frac{kg}{m^3}\right)$	$c_R (Pa^{-1})$	$C \left(\frac{J}{kg\,°C}\right)$	$K \left(\frac{W}{m\,°C}\right)$
Overlying Aquifer	Sand	Mt. Simon 1	85	2300	3.71E-10	920	2.51
Seal	Shale	Eau Claire 6	20	2580	7.42E-10	920	2.51
		Eau Claire 5	10	2580			
		Eau Claire 4	10	2580			
		Eau Claire 3	20	2580			
		Eau Claire 2	20	2580			

Zone	Matrix	Layer	h(m)	$\rho_R\left(\frac{kg}{m^3}\right)$	$c_R(Pa^{-1})$	$C\left(\frac{J}{kg\,°C}\right)$	$K\left(\frac{W}{m\,°C}\right)$
		Eau Claire 1	40	2580			
Storage Reservoir	Sand	Mt. Simon 23	10	2500	3.71E-10	920	2.51
		Mt. Simon 22	30	2500			
		Mt. Simon 21	15	2500			
		Mt. Simon 20	10	2500			
		Mt. Simon 19	25	2500			
		Mt. Simon 18	5	2500			
		Mt. Simon 17	45	2500			
		Mt. Simon 16	40	2500			
		Mt. Simon 15	10	2500			
		Mt. Simon 14	10	2500			
		Mt. Simon 13	10	2400			
		Mt. Simon 12	20	2400			
		Mt. Simon 11	10	2400			
		Mt. Simon 10	5	2400			
		Mt. Simon 9	15	2400			
		Mt. Simon 8	5	2400			
		Mt. Simon 7	10	2300			
		Mt. Simon 6	10	2300			
		Mt. Simon 5	5	2300			
		Mt. Simon 4	30	2300			
		Mt. Simon 3	40	2300			
		Mt. Simon 2	5	2300			
		Mt. Simon 1	30	2300			

Table 3.4: Porosity and permeability distributions for the heterogeneous scenarios

		Heterogeneous		
		Anisotropic		Isotropic
Layer	φ	$kH\,(md)$	$kV\,(md)$	$k\,(md)$
Eau Claire 6	1E-4	2.0E-3	8.0E-6	8.0E-6
Eau Claire 5	5E-4	4.1E-3	1.6E-5	1.6E-5
Eau Claire 4	0.053	1.5E-1	6.0E-4	6.0E-4
Eau Claire 3	0.096	3.0	1.2E-2	1.2E-2
Eau Claire 2	0.100	7.5	3.0E-2	3.0E-2
Eau Claire 1	0.080	1.1	4.4E-3	4.4E-3
Mt. Simon 23	0.061	5.0	2.0E-1	5.0
Mt. Simon 22	0.110	250	10	250
Mt. Simon 21	0.073	10	4.0E-1	10
Mt. Simon 20	0.083	4.0	1.6E-1	4.0
Mt. Simon 19	0.119	120	4.8	120
Mt. Simon 18	0.070	1.1	4.4E-2	1.1
Mt. Simon 17	0.130	200	8.0	200
Mt. Simon 16	0.083	5.0	2.0E-1	5.0
Mt. Simon 15	0.115	150	6.0	150
Mt. Simon 14	0.089	7.5	3.0E-1	7.5

| Layer | φ | Heterogeneous | | Isotropic |
| | | Anisotropic | | |
		kH (*md*)	kV (*md*)	k (*md*)
Mt. Simon 13	0.156	700	28	700
Mt. Simon 12	0.115	75	3.0	75
Mt. Simon 11	0.163	800	32.0	800
Mt. Simon 10	0.119	100	4.0	100
Mt. Simon 9	0.163	650	26	650
Mt. Simon 8	0.126	75	3.0	75
Mt. Simon 7	0.156	650	26	650
Mt. Simon 6	0.129	150	6.0	150
Mt. Simon 5	0.162	700	28	700
Mt. Simon 4	0.126	55	2.2	55
Mt. Simon 3	0.202	1,000	40	1,000
Mt. Simon 2	0.138	150	6.0	150
Mt. Simon 1	0.151	1,000	40	1,000

Table 3.5: Porosity and permeability values for the homogeneous scenarios

| Layer | φ | Homogeneous | | Isotropic |
| | | Anisotropic | | |
		kH (*md*)	kV (*md*)	k (*md*)
Eau Claire 1-6	0.055	2.0	8.0E-3	8.0E-3
Mt. Simon 1-23	0.124	298	12	298

Relative Permeability

A critical aspect of the flow behavior of a multiphase system is the relative permeability between two fluids, which depends on the wettability of the rock, the viscosities of the two fluids, the interfacial tension between the two fluids, and the tortuosity of the pores in the rock. This particular simulation study uses the Corey's Curves model (Corey, 1954) to describe the relative permeability. The parameters used in the Corey's Curves model are listed in Table 3.6 (using the notation of TOUGH2); Figure 3.5 displays the relative permeability curves.

Table 3.6: Parameters used in the Corey's Curves relative permeability model; residual water saturation (S_{lr}) and residual gas (CO_2) saturation (S_{gr}) for all three zones.

Zone	S_{lr}	S_{gr}
Overlying Aquifer	0.20	0.15
Seal	0.30	0.20
Storage Reservoir	0.20	0.15
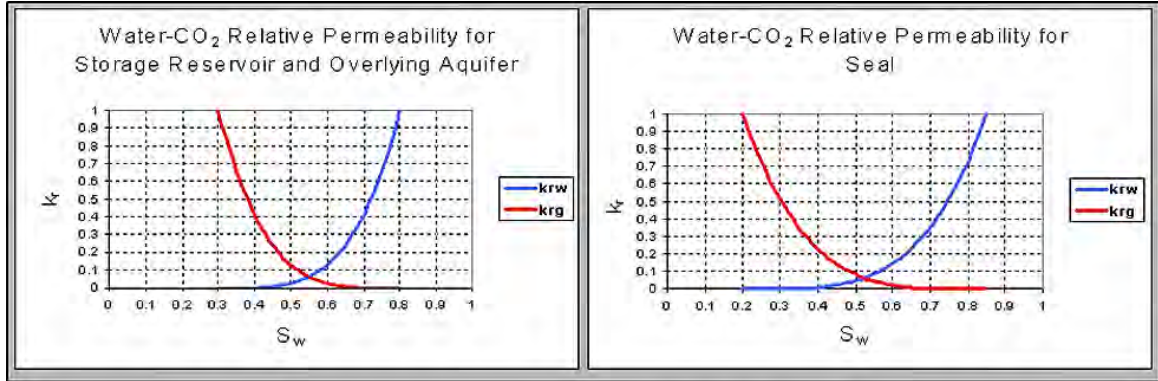
Figure 3.5: Relative permeability curves for the CO_2-water system using the Corey's Curves relationship. k_{rw} and k_{rg} are the relative permeabilities for water and CO_2, respectively, and S_w is the water saturation.

Capillary Pressure

Another important aspect of the flow behavior of a CO_2-water system is capillary pressure. At equilibrium, the force created by the surface tension between the two fluids is balanced by the pressure difference across the interface. This pressure difference is defined as the capillary pressure, P_c, and is described by the Laplace equation:

$$P_c \equiv P_{nw} - P_w = \frac{2\sigma \cos\Theta}{r_p} \tag{3.8}$$

where nw refers to the non-wetting phase (here: CO_2), w refers to the wetting phase (here: water), σ is the interfacial tension, Θ is the contact angle between the two fluids and the rock matrix, and r_p is the pore radius. For two immiscible fluids in contact with a porous medium, the capillary pressure governs the distribution of the non-wetting phase in the pore space.

The capillary entry pressure is defined as the minimum pressure required for CO_2 to displace water from the pore with the largest radius. Usually, the pores in shales are much smaller than the pores in sandstones. Consequently, the capillary entry pressure in a shale formation is much higher, making shales excellent barriers to fluid flow.

At the time of the initiation of this investigation we did not have any capillary pressure data for the Mt. Simon rocks or the Eau Claire; hence, we used capillary pressure measurements conducted on a sample of Berea sandstone. The measurements were performed by automated mercury injection porosimetry in the Department of Energy Resources Engineering at Stanford University. We first approximated the data with the van Genuchten function (van Genuchten, 1980) using the fractional form in Equation 3.9 and the fitting parameters in Table 3.7. We then used the Leverett J-function (Equation 3.10) (Leverett, 1941) to scale all the layers in the model (Mt. Simon 1-23 and Eau Claire 1-6) using the porosity and permeability values for each layer. All parameters used in the van Genuchten capillary pressure model in TOUGH2 are given in Table 3.7. The scaled capillary curves for each layer, as well as the capillary pressure curve for the Berea sandstone, are shown in Figures 3.6 to 3.8.

$$P_c = -P_0 \left[(S^*)^{-1/\lambda} - 1 \right]^{1-\lambda} \tag{3.9}$$

where $-P_{max} \leq P_c \leq 0$ and $S^* = \frac{S_l - S_{lr}}{S_{ls} - S_{lr}}$

In Equation 3.9 (using the notation of TOUGH2), P_0 is the capillary entry pressure, λ is a fitting parameter, S_l is the varying water saturation, S_{lr} is the residual water saturation, S_{ls} is the saturated water content, and P_{max} is the maximum capillary pressure at the residual water saturation.

$$J(S_{CO_2}) = \frac{P_c}{\sigma \cos \Theta} \sqrt{\frac{k}{\varphi}} \tag{3.10}$$

34

Table 3.7: Parameters used in the van Genuchten capillary pressure model

Layer	$P_{max}(Pa)$	λ	S_{lr}	S_{ls}	Heterogeneous $P_0(Pa)$	Homogeneous $P_0(Pa)$
Eau Claire 6	2.4E7	0.5	0.20	0.999	5.684E5	4.152E5
Eau Claire 5					8.877E5	
Eau Claire 4					1.504E6	
Eau Claire 3					4.547E5	
Eau Claire 2					2.935E5	
Eau Claire 1					6.855E5	
Mt. Simon 23	2.4E7	0.5	0.20	0.999	1.776E4	3.131E3
Mt. Simon 22					3.372E3	
Mt. Simon 21					1.376E4	
Mt. Simon 20					2.320E4	
Mt. Simon 19					5.063E3	
Mt. Simon 18					4.055E4	
Mt. Simon 17					4.099E3	
Mt. Simon 16					2.075E4	
Mt. Simon 15					4.451E3	
Mt. Simon 14					1.751E4	
Mt. Simon 13					2.400E3	
Mt. Simon 12					6.295E3	
Mt. Simon 11					2.295E3	
Mt. Simon 10					5.546E3	
Mt. Simon 9					2.546E3	
Mt. Simon 8					6.589E3	
Mt. Simon 7					2.491E3	
Mt. Simon 6					4.714E3	
Mt. Simon 5					2.443E3	
Mt. Simon 4					7.695E3	
Mt. Simon 3					2.285E3	
Mt. Simon 2					4.876E3	
Mt. Simon 1					1.975E3	
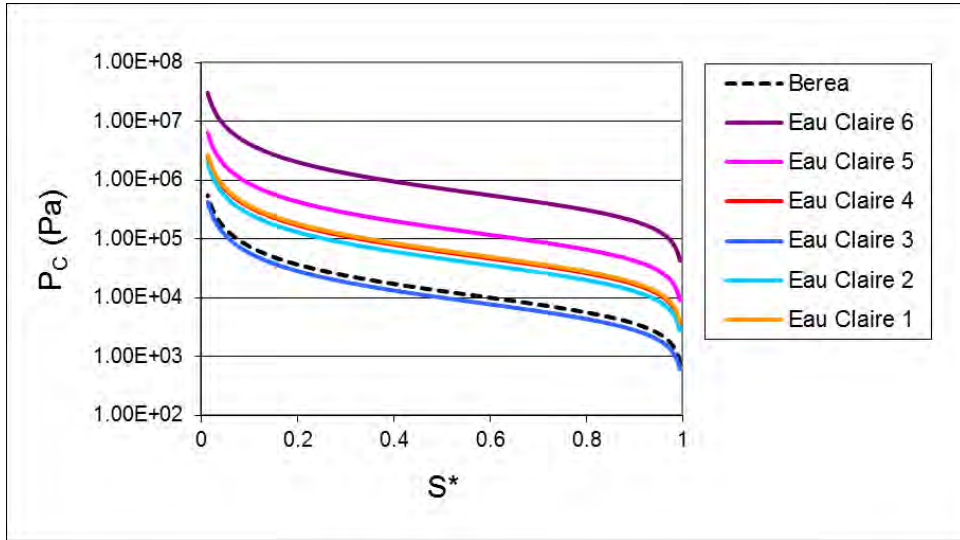
Figure 3.6: Scaled capillary pressure curves for the six layers in the seal (Eau Claire 1-6), as well as the base capillary pressure curve for the Berea sandstone
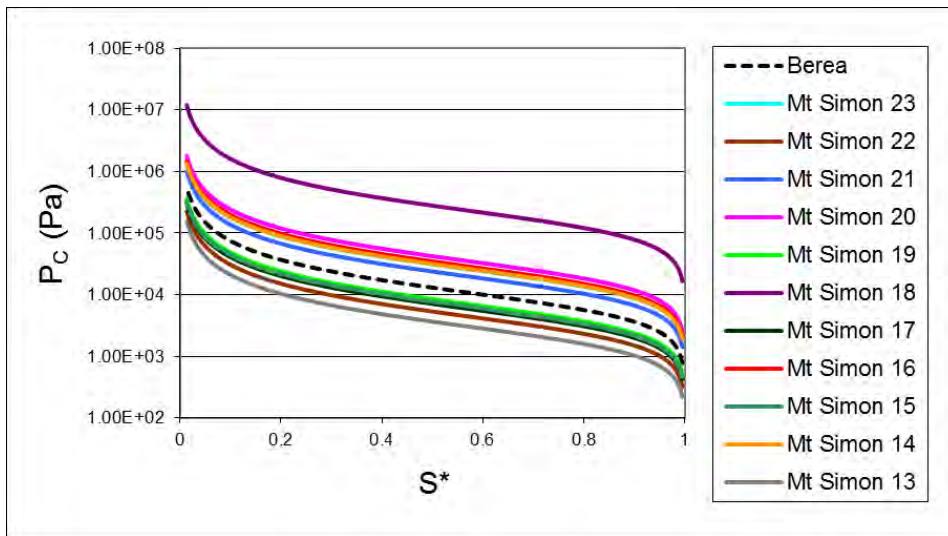
Figure 3.7: Scaled capillary pressure curves for the eleven uppermost layers in the storage reservoir (Mt. Simon 13-23), as well as the base capillary pressure curve for the Berea sandstone
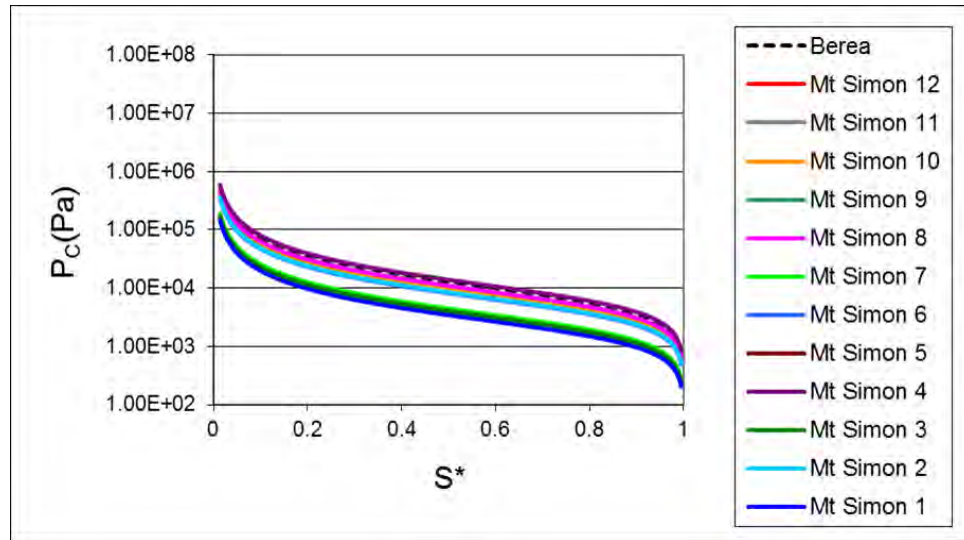
Figure 3.8: Scaled capillary pressure curves for the twelve lowermost layers in the storage reservoir (Mt. Simon 1-12), as well as the base capillary pressure curve for the Berea sandstone

3.4.3. Sensitivity Analysis

Because it is critical to know whether there is a distinct pressure response due to CO_2 being present in the system compared to when there is just water flowing, a sensitivity analysis is conducted on the effects of CO_2 injection versus pure water injection, assuming equivalent volumetric injection flow rates. Given that a total of one million metric tons of CO_2 is scheduled to be injected at the ADM site over the course of three years, the CO_2 injection mass flow rate is set to be 10.6 kg per second. Assuming the same volumetric flow rate for the pure water injection case, the water injection mass flow rate is set to 13.6 kg per second, taking the densities of water and supercritical CO_2 into account. For each case (pure CO_2 injection and pure water injection), we let the fluid be injected into Mt. Simon 1 and Mt. Simon 3 and we let the simulation run for three years.

3.5. Data Processing

The simulated output data is processed two ways. First, based on conventional well test analysis approaches (Horne, 1995), we examine the pressure transients at some given

depths in the monitoring well. Four monitoring points are assigned to the storage reservoir, one monitoring point is assigned to the seal, and one monitoring point is assigned to the overlying aquifer. Second, since we are interesting in obtaining a better understanding of where the CO_2 plume and the displaced water will migrate in the reservoir, we examine vertical pressure gradients at the monitoring well as a function of time. In this case, we do not limit ourselves to only a few monitoring points but are interested in the maximum information obtainable. For a real case setting it is desirable to distribute a given number of pressure monitors as wisely as possible.

3.5.1. Pressure Transients

An initial step for pressure transient analysis is to examine the change in pressure as a function of time. The pressure change, or, pressure buildup, can be defined as

$$\Delta P_z = P_{zt} - P_{zi} \tag{3.11}$$

where P_{zt} is the pressure at depth z at some time t, and P_{zi} is the initial hydrostatic pressure at that same depth. ΔP_z is usually plotted on logarithmic axes.

3.5.2. Vertical Pressure Gradients Normalized by Initial Hydrostatic Pressure

Another approach is to look at the change in the vertical pressure gradient as a function of time. If there is fluid flowing at the monitoring well, one would expect to see a pressure response. If, on the other hand, there is no flow, one would expect to see no changes from the initial hydrostatic pressure. The hydrostatic pressure is defined as

$$P = P_{atm} + \Delta d\, \mathbf{g}\, \overline{\rho_w} \tag{3.12}$$

where P_{atm} is the atmospheric pressure, Δd is the depth below the water table, and $\overline{\rho_w}$ is the average water density.

One way to examine the vertical pressure gradient is to look at the pressure gradient for each small length segment along the monitoring well and normalize it by the pressure gradient for the initial hydrostatic conditions. In the simulation model, each small length segment corresponds to the distance between the midpoints of two vertically adjacent grid cells (see Figure 3.9). The pressure gradient for the initial hydrostatic conditions is given by

$$\Delta P_i = P_{i2} - P_{i1} = \Delta z \, g \, \overline{\rho_w} \tag{3.13}$$

where P_{i2} is the initial hydrostatic pressure in the deeper grid cell, P_{i1} is the initial hydrostatic pressure in the shallower grid cell, and Δz is the length segment between the midpoints of the two grid cells. Similarly, the pressure difference at some later time t is given by

$$\Delta P(t) = P_2(t) - P_1(t) \tag{3.14}$$

where $P_2(t)$ is the pressure in the deeper grid cell at time t and $P_1(t)$ is the pressure in the shallower grid cell at time t. Figure 3.9 summarizes the two possibilities for the normalized vertical pressure gradient; a ratio of 1 indicates no change from the initial hydrostatic conditions; a ratio not equal to 1 indicates some vertical flow at the monitoring well.
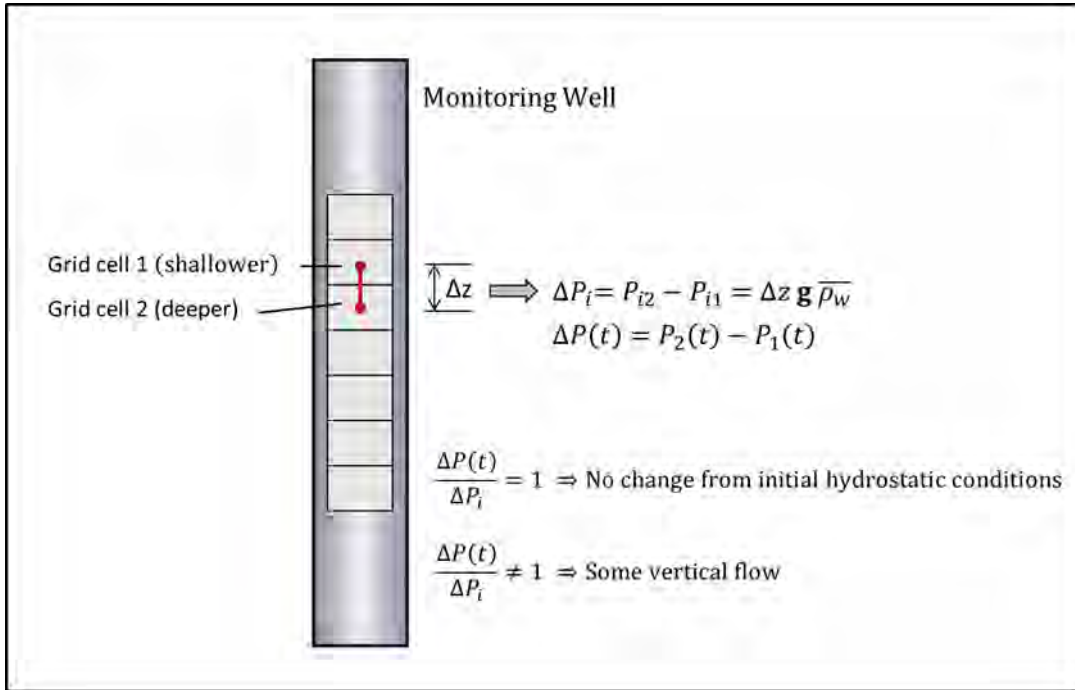
Figure 3.9: Illustration of the normalized vertical pressure gradient analysis.

Chapter 4

4. Results

In the following sections we present the results from a simulation study that encompasses CO_2 injection, and, for comparison purposes, pure water injection, into a 30-layer system comprised of storage reservoir, seal, and overlying aquifer. First, we discuss the simplest scenario, which is that of a homogeneous and isotropic system. The second scenario encompasses a homogeneous and anisotropic system, the third scenario is that of a heterogeneous and isotropic system, and finally, we discuss the perhaps most realistic scenario, which is that of a heterogeneous and anisotropic system. The heterogeneity and anisotropy are here understood as applying to the vertical direction only; in the radial direction each layer remains uniform. For each scenario we first examine pressure transients for CO_2 injection and for pure water injection for six equally distributed pressure monitors in the monitoring well. Then we examine vertical pressure gradients at the monitoring well, both for pure CO_2 injection and for pure water injection.

4.1. Homogeneous Isotropic Scenario

Porosity and permeability distributions, along with the position of the CO_2 plume over time, are shown in in Figure 4.1. Supercritical CO_2 is injected continuously over three years into the deepest portion of the storage reservoir. The CO_2 plume contour is defined as the contour of the CO_2 plume where the gas saturation, SG, is 0.1. Initially, the CO_2 is not constrained by any low permeability layers and migrates mainly in the upward direction. Due to buoyancy forces, since CO_2 is less dense than water, the plume will migrate upward until it reaches a geologic barrier. When the CO_2 reaches the top of the storage reservoir, the lower permeability seal prevents the plume from extending higher, forcing the plume to migrate laterally. The resulting characteristic shape of the CO_2 plume is commonly referred to as the "gravity tongue." The upper portion of the CO_2 plume reaches the monitoring well after 16 months of injection. Monitoring points for the

pressure transient investigation are illustrated by red markers and their depths are indicated by dashed, horizontal lines.
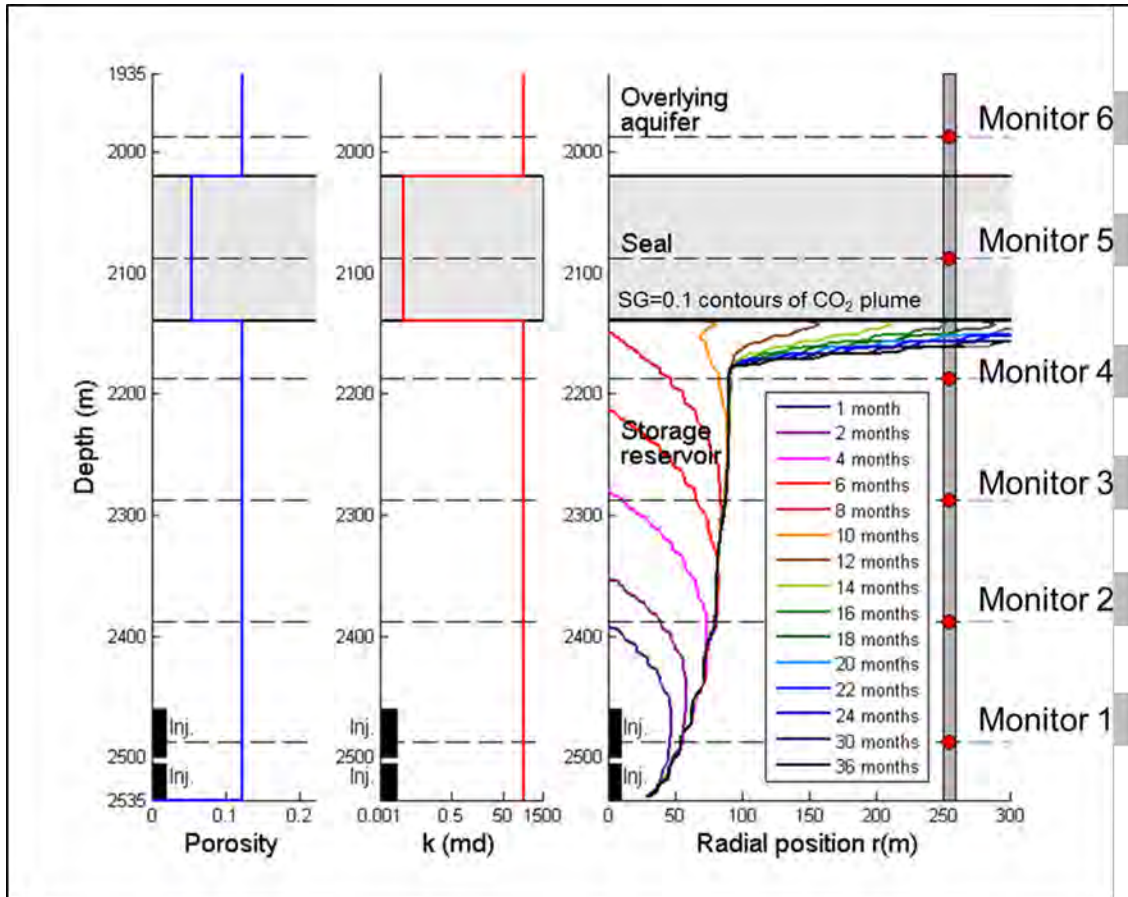
Figure 4.1: Homogeneous isotropic scenario: Left and Middle: Porosity (blue) and permeability (red) distributions for storage reservoir, seal, and overlying aquifer. Right: CO_2 plume contour as a function of position and time (a cutoff gas saturation SG of 0.1 defines the contour) and locations of the six pressure monitors in the monitoring well. Note that the black boxes indicating injection layers are drawn to scale only in the vertical direction.

4.1.1. Pressure Transients

In Figure 4.2 we show the pressure transients for each of the six monitors; in Figure 4.3 we display the pressure transients on logarithmic axes. Figure 4.3 shows the full range of pressure buildups; in Figure 4.3 the range is limited to pressure buildups that are above an assumed detection limit of 0.001 MPa.

42

At monitors 1-4, the pressure almost instantaneously builds up to 0.02 MPa. For the water injection case, each monitor experiences a steady increase in pressure buildup over time. The degree of pressure buildup, however, depends on the location of the monitor; shallower monitors experience slightly less pressure buildup. After three years of injection, the pressure buildup for the water injection case is almost 0.05 MPa at Monitor 1 and about 0.045 MPa at Monitor 4.
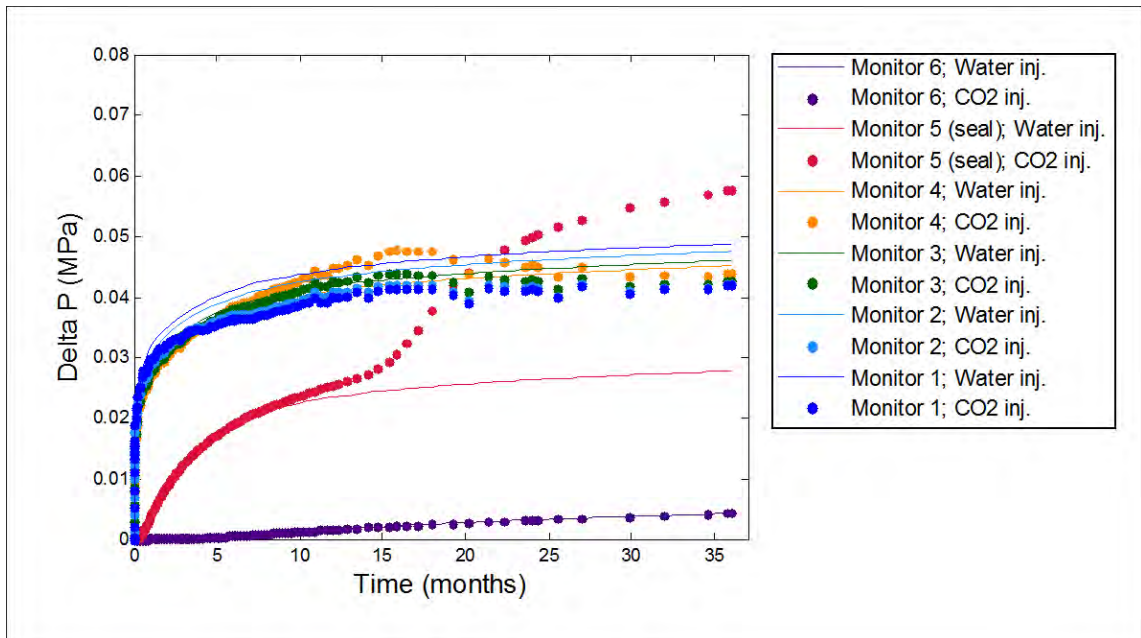
Figure 4.2: Pressure transients at Monitors 1-6 for the homogeneous isotropic scenario

For the first four months of injection, the pressure response at monitors 1-4 is slightly less for the CO_2 injection case than for the water injection case. The trend is still the same; the shallower monitors experience slightly less pressure drop. After four months of injection, however, the trend reverses for the CO_2 injection case; now the pressure response is greater for the monitors at shallower depths. Furthermore, for the CO_2 injection case, there is a hump in the pressure buildup about 15 months after the start of injection. For the CO_2 injection case, the pressure after three years of injection ranges from about 0.042 MPa for Monitor 1 to about 0.044 MPa for Monitor 4.
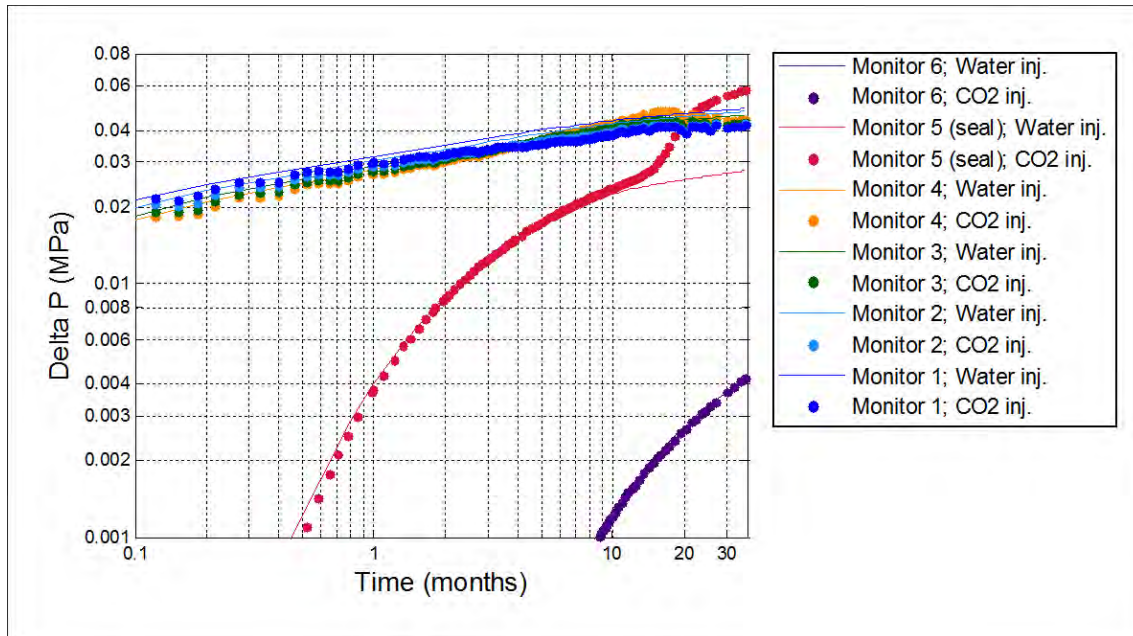
Figure 4.3: Pressure transients at Monitors 1-6 plotted on logarithmic axes for the homogeneous isotropic scenario

The pressure buildup at Monitor 5 in the seal increases steadily and reaches the assumed detection limit of 0.001 MPa after about two weeks of injection. After 10 months of injection, the pressure buildup for the CO_2 injection case starts to deviate from the pressure buildup for the water injection case. After 15 months of injection there is a sharp and distinct increase in the pressure buildup for the CO_2 injection case. After three years of injection, the pressure buildup at Monitor 5 is almost 0.06 MPa for the CO_2 injection case but only about 0.028 MPa for the water injection case.

The pressure buildup at Monitor 6 increases steadily but does not reach the assumed detection limit until after eight and a half months of injection.

4.1.2. *Vertical Pressure Gradients Normalized by Initial Hydrostatic Pressure*

Figure 4.4 shows the vertical pressure gradients after one month and after 12 months of injection, along with permeability as a function of depth.
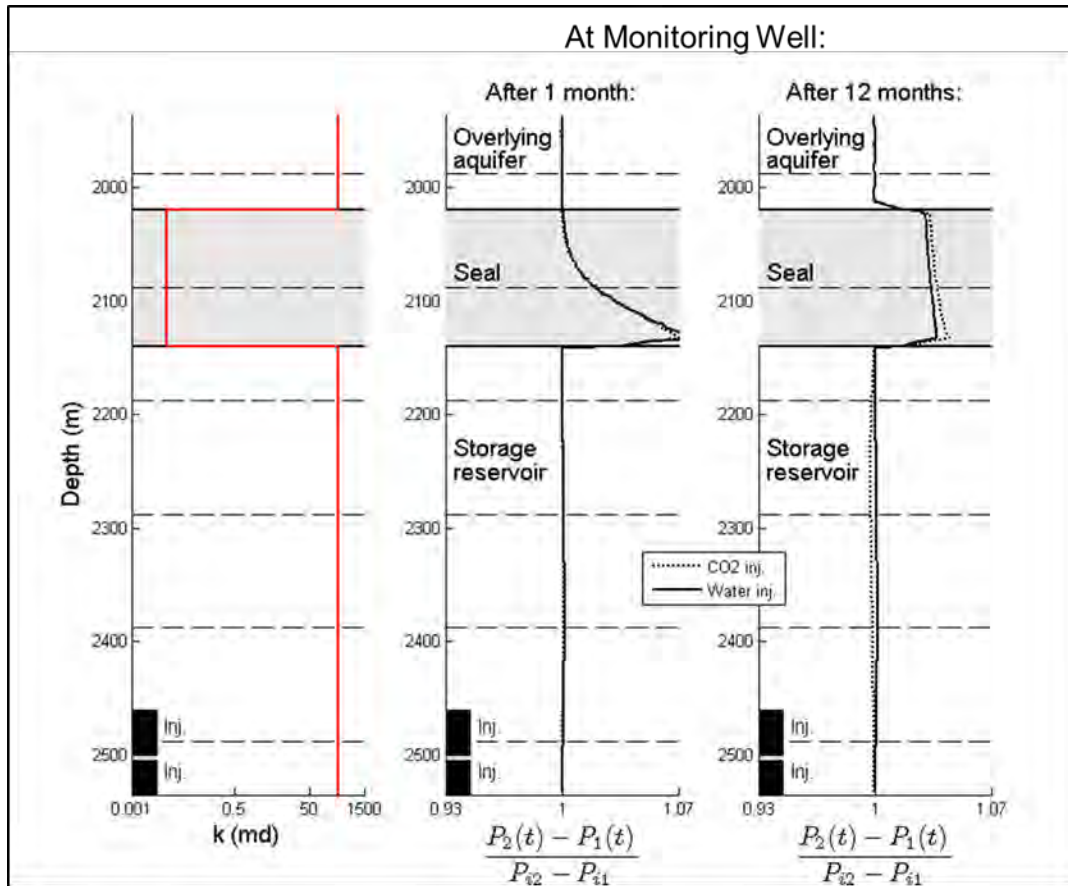
Figure 4.4: Homogeneous isotropic scenario: Left: Permeability distribution for storage reservoir, seal, and overlying aquifer. Middle: Normalized vertical pressure gradients at the monitoring well after one month of injection, for CO_2 injection and pure water injection. Right: Normalized vertical pressure gradients after 12 months of injection, for CO_2 injection and pure water injection.

After one month of injection there is no detectable difference between the CO_2 injection case and the water injection case. In the storage reservoir and the overlying aquifer, the normalized vertical pressure gradient equals 1. In the lower part of the seal there is a sharp, positive anomaly in the normalized vertical pressure gradient.

After 12 months of injection we start to see a slight difference between the CO_2 injection case and the pure water injection case, both in the storage reservoir and in the seal. In the storage reservoir, the normalized vertical pressure gradient is slightly less for the CO_2 injection case than for the water injection case. In the seal, the normalized vertical pressure gradient is slightly greater for the CO_2 injection case than for the water

injection case. Moreover, the spike in the normalized vertical pressure gradient that we saw earlier in the seal is now gone; there is at this time a more uniform increase in the normalized vertical pressure gradient along the entire height of the seal.

Figure 4.5 shows the position of the CO_2 plume with time, along with the normalized vertical pressure gradients for the CO_2 injection case from which the normalized vertical pressure gradients for the water injection case have been subtracted.
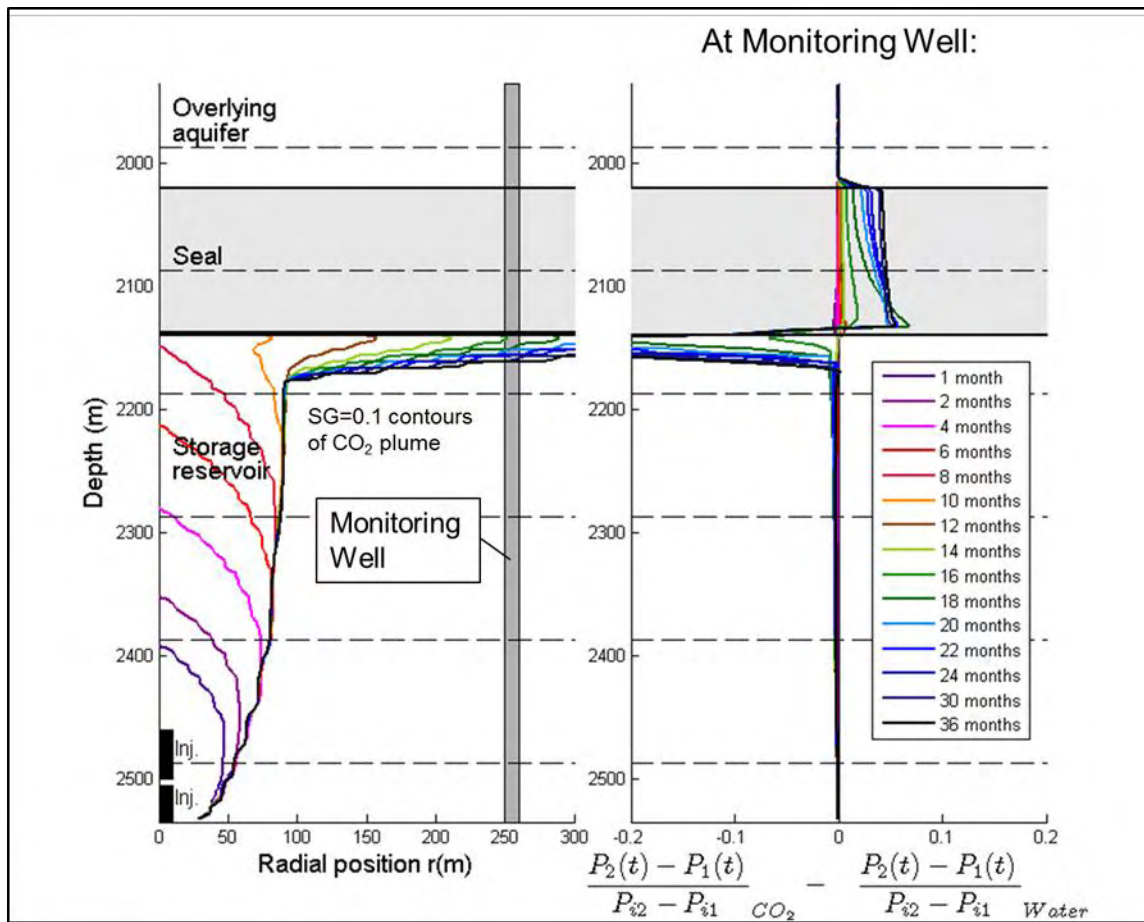
Figure 4.5: Homogeneous isotropic scenario: Left: CO_2 plume contour as a function of position and time (a cutoff gas saturation SG of 0.1 defines the contour). Right: Normalized vertical pressure gradient deviations as a function of time (normalized vertical pressure gradients for CO_2 injection from which the normalized vertical pressure gradients for water injection have been subtracted).

For the first 12 months there is, as we saw in Figure 4.4, hardly any difference between the normalized vertical pressure gradients for the CO_2 injection case and the normalized vertical pressure gradients for the water injection case. After 12 months of injection, however, the two cases start to deviate. In particular, there is a negative deviation just below the seal and a positive deviation in the seal. The position of the negative deviation below the seal corresponds well with the position of the upper part of the CO_2 plume that migrates laterally toward the monitoring well.

4.2. Homogeneous Anisotropic Scenario

Porosity and horizontal permeability distributions, along with the position of the CO_2 plume over time, are shown in Figure 4.6. Supercritical CO_2 is injected continuously over three years into two zones at the bottom of the storage reservoir. Constrained by a low vertical permeability, the CO_2 plume migrates mainly laterally. Given the homogeneity of the system, there is also some upward flow. In the beginning, the plume splits into two lateral tongues; this can be attributed to there being a 5 m interval with no injection between the two injection zones. As the CO_2 plume migrates further away from the injection well, the shape of the CO_2 plume becomes more rounded. The fastest portion of the CO_2 plume arrives at the monitoring well three years after start of injection, i.e., at the end of the simulation time. Monitoring points for the pressure transient investigation are illustrated by red markers, and their depths are indicated by dashed, horizontal lines.
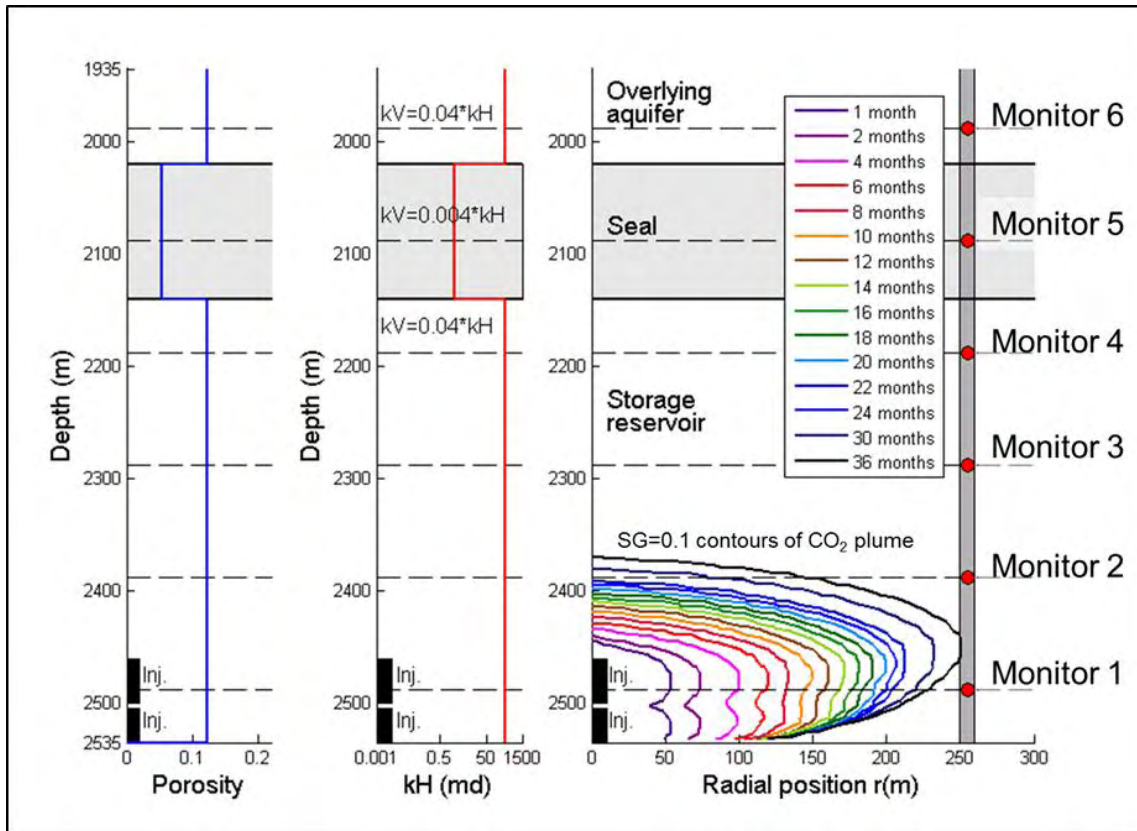
Figure 4.6: Homogeneous anisotropic scenario: Left and Middle: Porosity (blue) and permeability (red) distributions for storage reservoir, seal, and overlying aquifer. Right: CO_2 plume contour as a function of position and time (a cutoff gas saturation SG of 0.1 defines the contour) and locations of the six pressure monitors in the monitoring well. Note that the black boxes indicating injection layers are drawn to scale only in the vertical direction.

4.2.1. Pressure Transients

In Figure 4.7 we show the pressure transients for each of the six monitors; in Figure 4.8 we display the pressure transients on logarithmic axes. In Figure 4.7 the full range of pressure buildups is shown; in Figure 4.8 we limit the range to pressure buildups that are above an assumed detection limit of 0.001 MPa.

At Monitor 1 there is an almost immediate pressure buildup of 0.045 MPa for both the CO_2 injection case and the water injection case. After about one month of injection, the pressure responses for the two cases start to deviate; after about 10 months the pressure buildup starts to fall quite rapidly for the CO_2 injection case. After three years of injection, the pressure buildup at Monitor 2 is 0.05 MPa for the CO2 injection

case, whereas the pressure buildup has risen to more than 0.07 MPa for the water injection case.
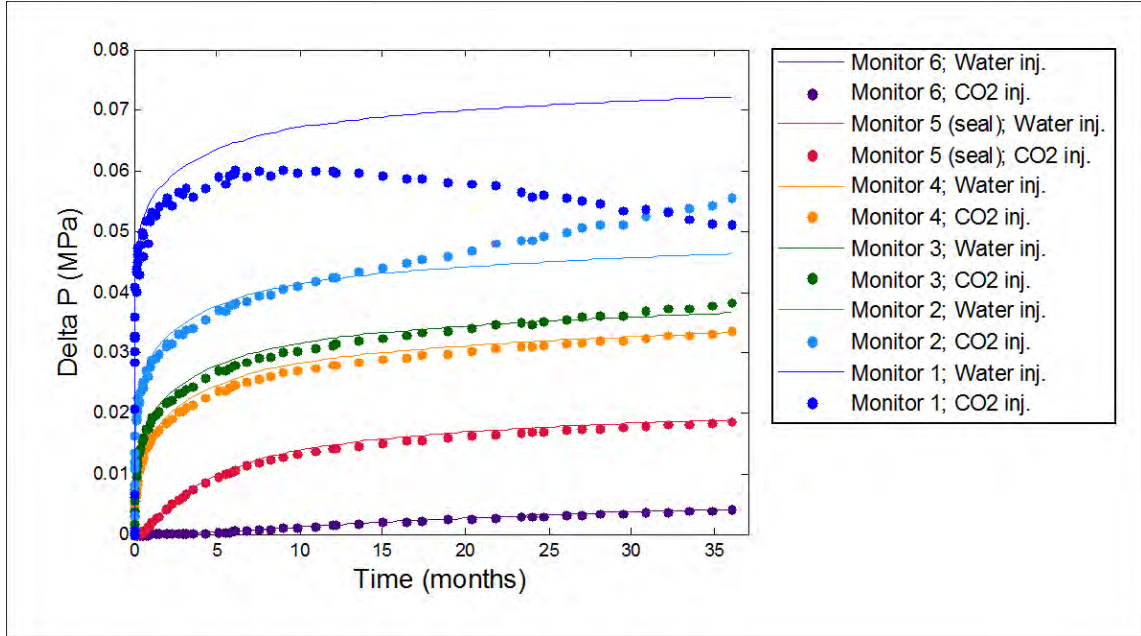
Figure 4.7: Pressure transients at Monitors 1-6 for the homogeneous anisotropic scenario

The pressure buildup at Monitor 2 reaches a value of close to 0.02 MPa almost instantaneously and the pressure response is almost identical for the CO_2 injection case and the water injection case for the first 10 months of injection. After 10 months of injection, the pressure response for the two cases starts to deviate, and after three years of injection the pressure buildup at Monitor 2 is about 0.056 MPa for the CO_2 injection case and about 0.046 MPa for the water injection case.

For Monitors 3-6, the pressure response for the CO_2 injection case is almost identical to that for the pure water injection case. At Monitor 3, the pressure buildup reaches a value of 0.01 MPa almost instantaneously, whereas the pressure buildup at Monitor 4 reaches a value of 0.006 MPa almost instantaneously. At Monitor 5, which is placed in the seal, we see a pressure buildup above the assumed detection limit after about three weeks of injection. Monitor 6, which is placed above the seal, detects a pressure buildup above 0.001 MPa after nine months of injection.
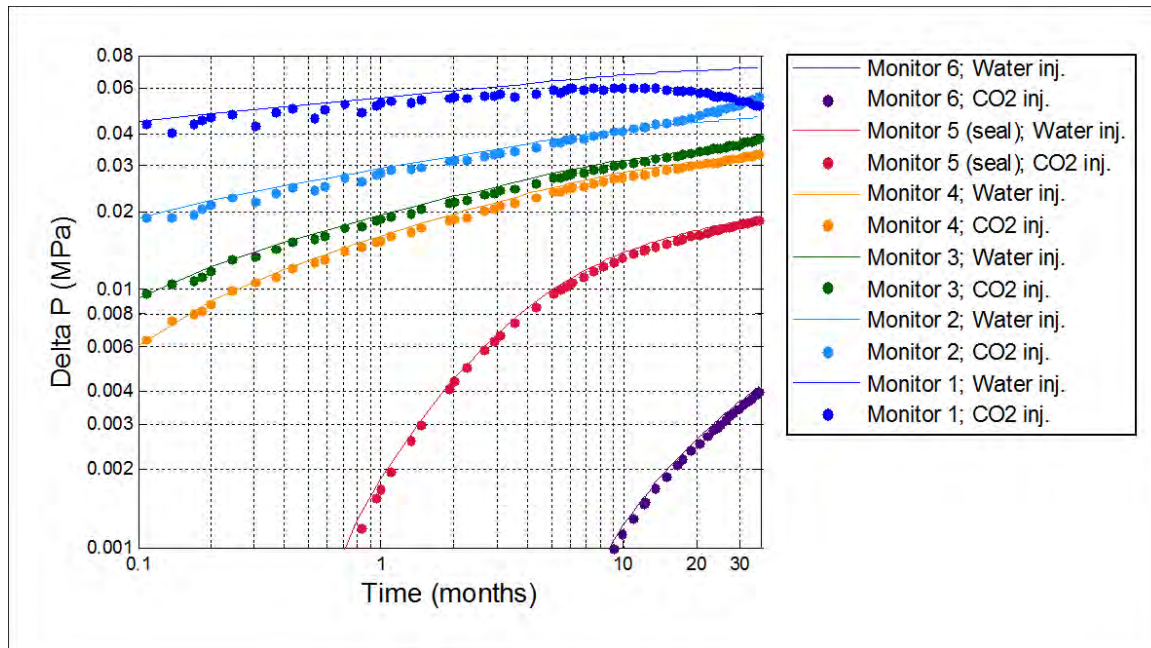
Figure 4.8: Pressure transients at Monitors 1-6 plotted on logarithmic axes for the homogeneous anisotropic scenario

4.2.2. Vertical Pressure Gradients Normalized by Initial Hydrostatic Pressure

Figure 14.9 shows the vertical pressure gradients after one month and after 12 months of injection, along with horizontal permeability as a function of depth.

After one month of injection there is no detectable difference between the CO_2 injection case and the water injection case. In the lower portion of the storage reservoir there is a positive anomaly in the normalized vertical pressure gradient; higher up, closer to the seal, the normalized vertical pressure gradient goes to 1. In the lower part of the seal, there is a sharp, positive anomaly in the normalized vertical pressure gradient. In the overlying aquifer, the normalized vertical pressure gradient equals 1.

After 12 months of injection we see some difference between the CO_2 injection case and the pure water injection case in the lower portion of the storage reservoir. The normalized vertical pressure gradient for the water injection case is close to identical to what it was after one month of injection. The normalized vertical pressure gradient for

50
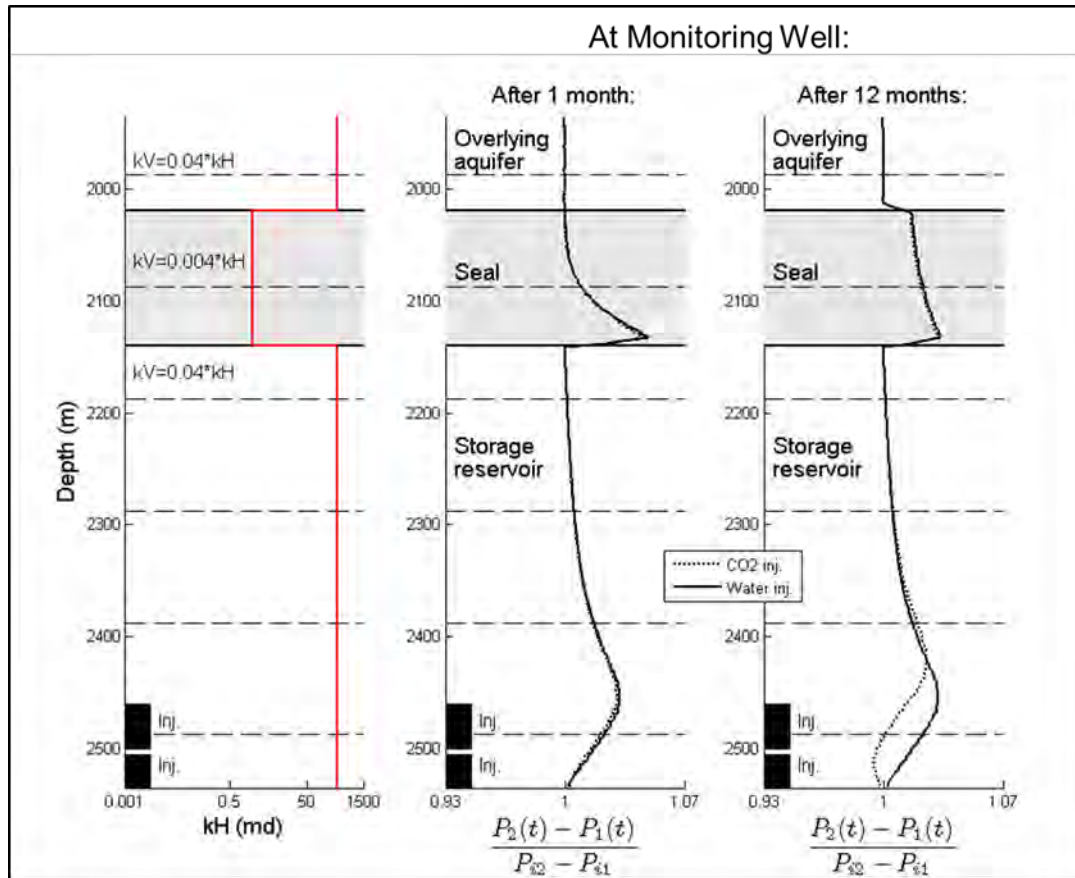
Figure 4.9: Homogeneous anisotropic scenario: Left: Permeability distribution for storage reservoir, seal, and overlying aquifer. Middle: Normalized vertical pressure gradients at the monitoring well after one month of injection, for CO_2 injection and pure water injection. Right: Normalized vertical pressure gradients after 12 months of injection, for CO_2 injection and pure water injection.

the CO_2 injection case is less than 1 at the bottom of the storage reservoir and greater than 1 but still less than for the water injection case a little higher up. In the upper half of the storage reservoir and in the rest of the system, the normalized vertical pressure gradients are the same for the CO_2 injection and the water injection cases. In the seal, the spike in the normalized vertical pressure gradient that we saw after one month of injection is gone; there is at this time a more uniform, positive normalized vertical pressure gradient along the entire height of the seal.

Figure 4.10 shows the position of the CO_2 plume with time, along with the normalized vertical pressure gradients for the CO_2 injection case, from which the normalized vertical pressure gradients for the water injection case have been subtracted.

51

In the lower part of the storage reservoir there is a negative normalized vertical pressure gradient deviation. The negative deviation becomes larger with time. Directly above the negative deviation there is a positive deviation in the normalized vertical pressure gradient.
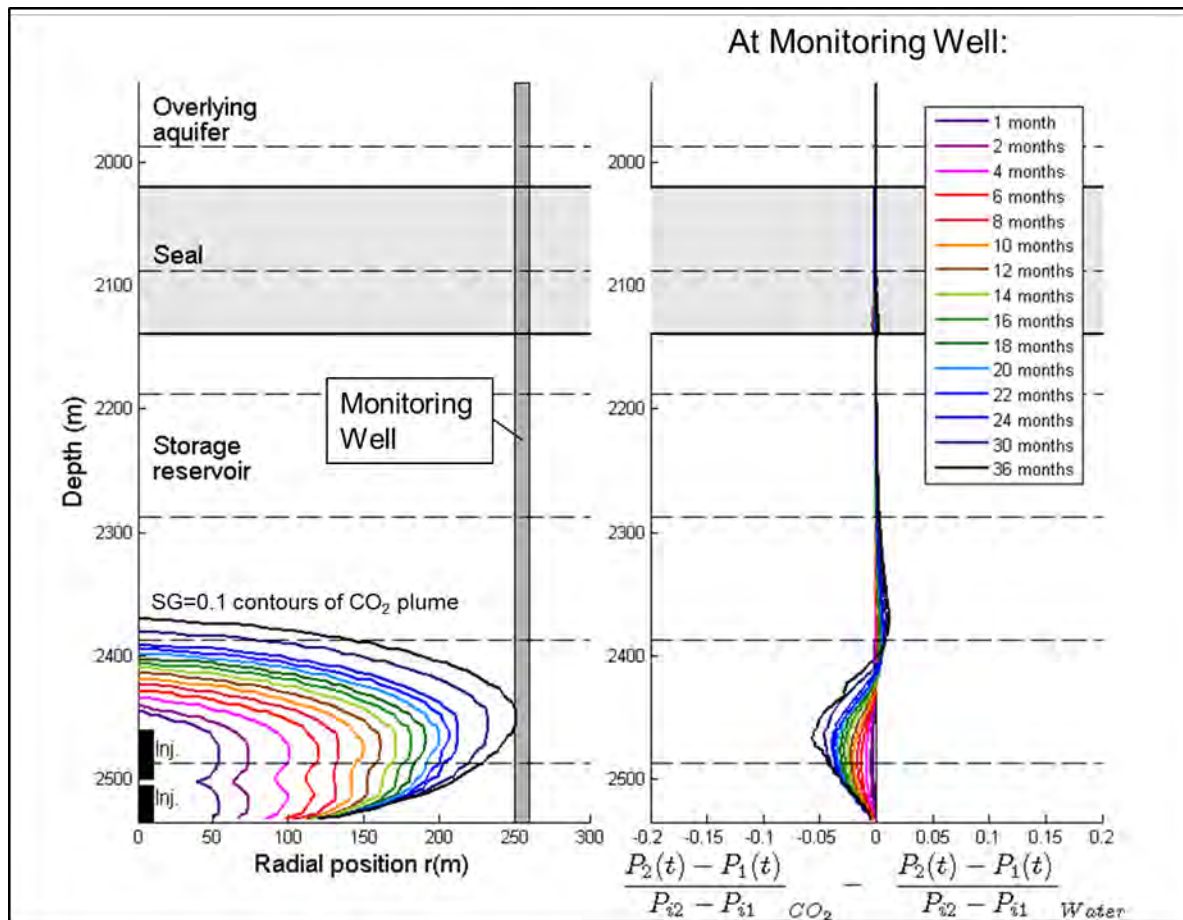
Figure 4.10: Homogeneous anisotropic scenario: Left: CO_2 plume contour as a function of position and time (a cutoff gas saturation SG of 0.1 defines the contour). Right: Normalized vertical pressure gradient deviations as a function of time (normalized vertical pressure gradients for CO_2 injection from which the normalized vertical pressure gradients for water injection have been subtracted).

The positive deviation also grows larger with time, though the magnitude is much less than for the negative deviation. The vertical position of the negative deviation corresponds well with the vertical position of the CO_2 plume. Also, the maximum negative deviation in the normalized pressure gradient appears to occur at a similar (but

not exactly the same) depth as the maximum lateral extent of the CO_2 plume. The positive deviation occurs slightly above or at the same height as the upper part of the CO_2 plume.

4.3. Heterogeneous Isotropic Scenario

For the heterogeneous isotropic scenario, porosity and permeability distributions as functions of depth, as well as the position of the CO_2 plume with time, are displayed in Figure 4.11. Due to the heterogeneity of the system and some layers of lower permeability, the plume is somewhat restricted. For the heterogeneous isotropic scenario, the front of the plume eventually splits into three lateral tongues. The fastest part of the front reaches the monitoring well 22 months after start of injection. The six pressure monitoring points are illustrated by red markers, and their depths are indicated by dashed, horizontal lines.

4.3.1. Pressure Transients

In Figure 4.12 we show the pressure transients for each of the six monitors; in Figure 4.13 we display the pressure transients on logarithmic axes. In Figure 4.12 the full range of pressure buildups is shown; in Figure 4.13 we limit the range to pressure buildups that are above an assumed detection limit of 0.001 MPa.

Monitors 1 and 2 detect almost instantaneous pressure buildups of about 0.02 MPa. For Monitor 1, the pressure buildup is always somewhat less for the CO_2 injection case than for the water injection case, however after five months of injection, the pressure buildup for the CO_2 injection case starts to deviate significantly from that of the pure water injection case. After three years of injection, the pressure buildup at Monitor 1 is 0.045 MPa for the CO_2 injection case and about 0.037 MPa for the water injection case. For Monitor 2, the pressure buildups for the CO_2 injection case and the water injection case remain similar for 25 months of injection. After three years of injection, the pressure buildup at Monitor 2 is about 0.038 MPa for the CO_2 injection case and about 0.0425 MPa for the water injection case.

Monitor 3 detects an almost instantaneous pressure buildup of about 0.013 MPa. For the first 12 months, the pressure responses are nearly identical for the CO_2 injection case and the pure water injection case. After 12 months of injection, the pressure responses start to deviate. After three years of injection, the pressure buildup is about 0.43 MPa for the CO_2 injection case and about 0.0375 MPa for the water injection case.
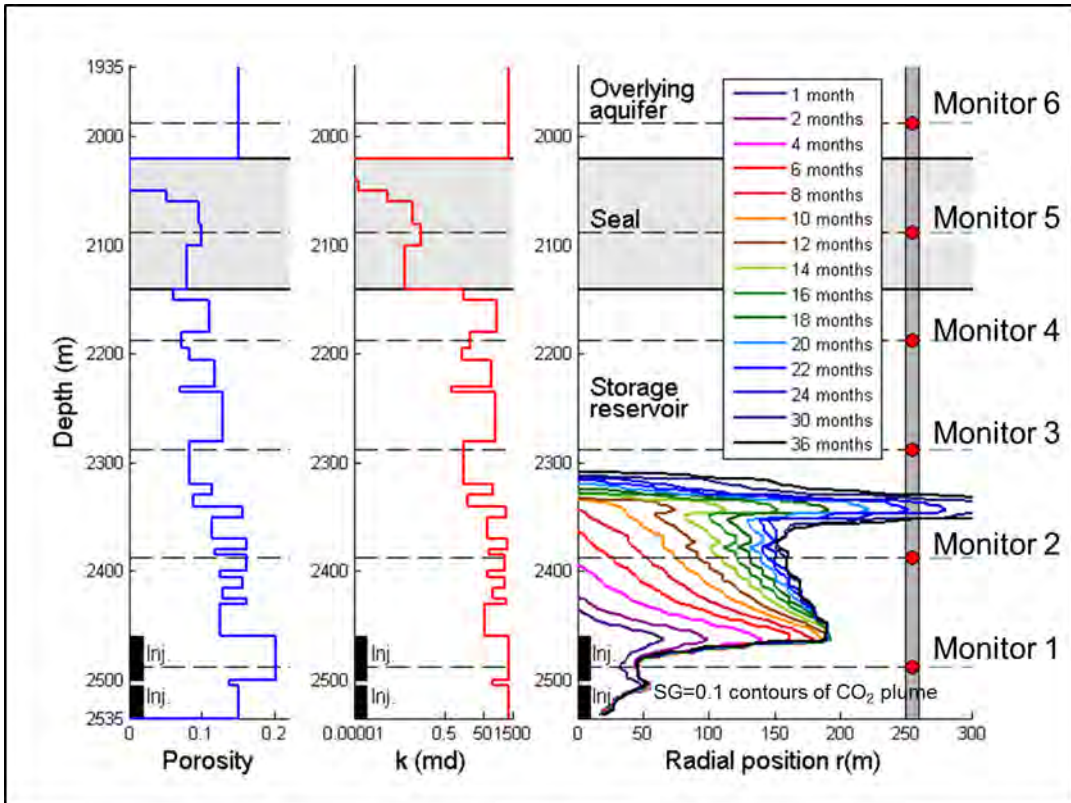
Figure 4.11: Heterogeneous isotropic scenario: Left and Middle: Porosity (blue) and permeability (red) distributions for storage reservoir, seal, and overlying aquifer. Right: CO_2 plume contour as a function of position and time (a cutoff gas saturation SG of 0.1 defines the contour) and locations of the six pressure monitors in the monitoring well. Note that the black boxes indicating injection layers are drawn to scale only in the vertical direction.
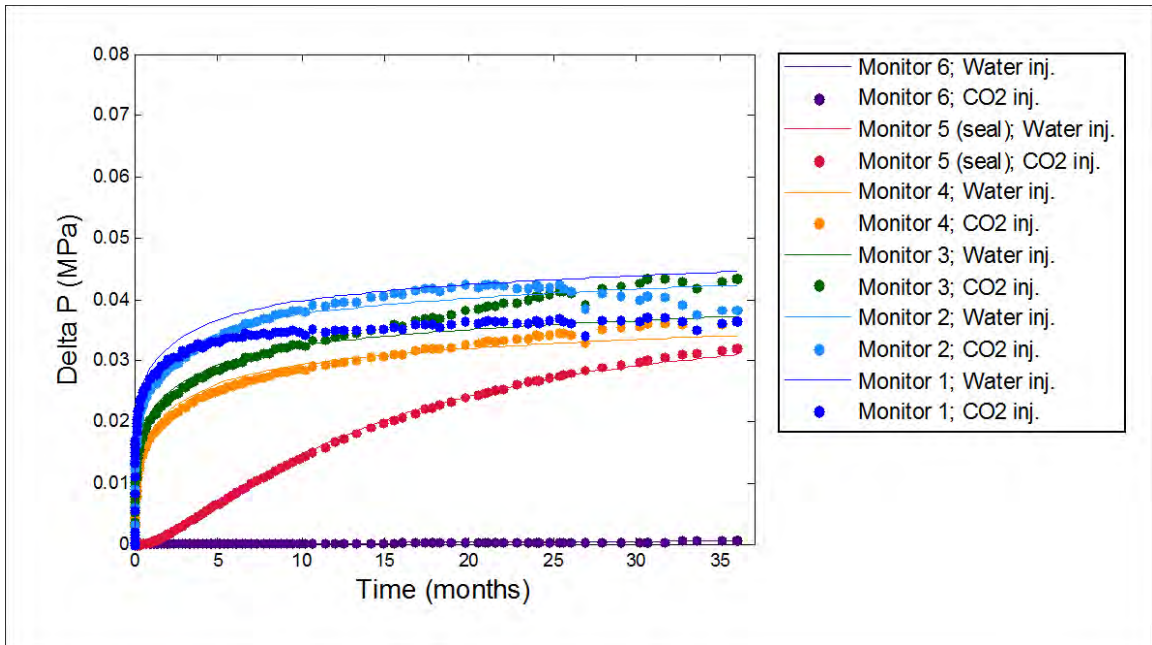
Figure 4.12: Pressure transients at Monitors 1-6 for the heterogeneous isotropic scenario

At Monitor 4, there is an almost instantaneous pressure response of 0.008 MPa, and the pressure buildups for the CO_2 injection case and pure water injection case follow each other closely for 25 months of injection. After 25 months of injection they start to deviate, and after three years of injection, the pressure buildup is about 0.036 MPa and 0.034 MPa for the CO_2 injection case water injection case, respectively.

At Monitor 5, which is placed in the seal, the pressure response is the same for the CO_2 injection case as for the water injection case. The pressure buildup reaches the assumed detection limit of 0.001 MPa after one and a half months of injection, however the increase in pressure response is quite rapid. After three years of injection, the pressure buildup at Monitor 5 has reached just above 0.03 MPa.

At Monitor 6, which is placed above the seal, the pressure buildup never reaches the assumed detection limit of 0.001 MPa. As we can see from Figure 4.12, the pressure response at Monitor 6 stays fairly flat during the entire period of injection.
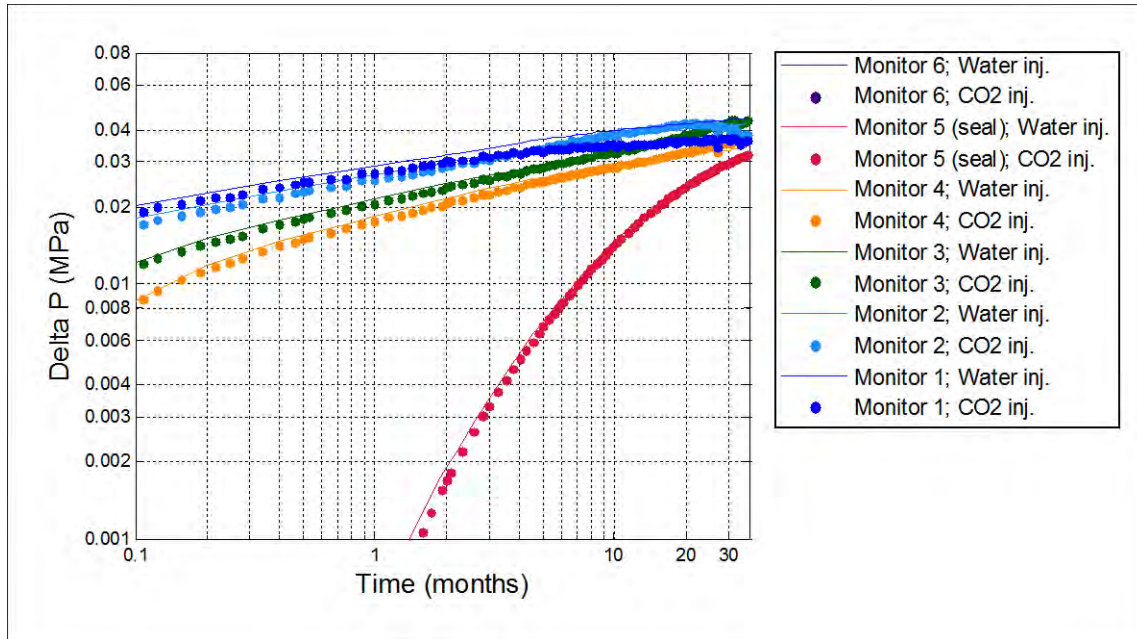
Figure 4.13: Pressure transients at Monitors 1-6 plotted on logarithmic axes for the heterogeneous isotropic scenario

4.3.2. Vertical Pressure Gradients Normalized by Initial Hydrostatic Pressure

Figure 4.14 shows the vertical pressure gradients after one month and after 12 months of injection, along with the permeability distribution as a function of depth.

After one month of injection there is no detectable difference between the CO_2 injection case and the water injection case. At some depths in the storage reservoir as well as in the overlying aquifer, the normalized vertical pressure gradient equals 1. At other depths in the reservoir, there are distinct positive anomalies in the normalized vertical pressure gradients. In the lower part of the seal, there is a sharp, positive anomaly in the normalized vertical pressure gradient.

After 12 months of injection we see some difference between the CO_2 injection case and the pure water injection case in the storage reservoir. In particular, there is a negative anomaly for the CO_2 injection case just above the injection zone, whereas the normalized vertical pressure gradient appears to be the same as it was after one month of

56

injection. Higher up in the storage reservoir, there is a slightly greater positive anomaly for the CO_2 injection case than for the water injection case. In the seal, the spike in the normalized vertical pressure gradient that we saw after one month of injection is gone; instead there are two zones of large, positive normalized pressure gradients.
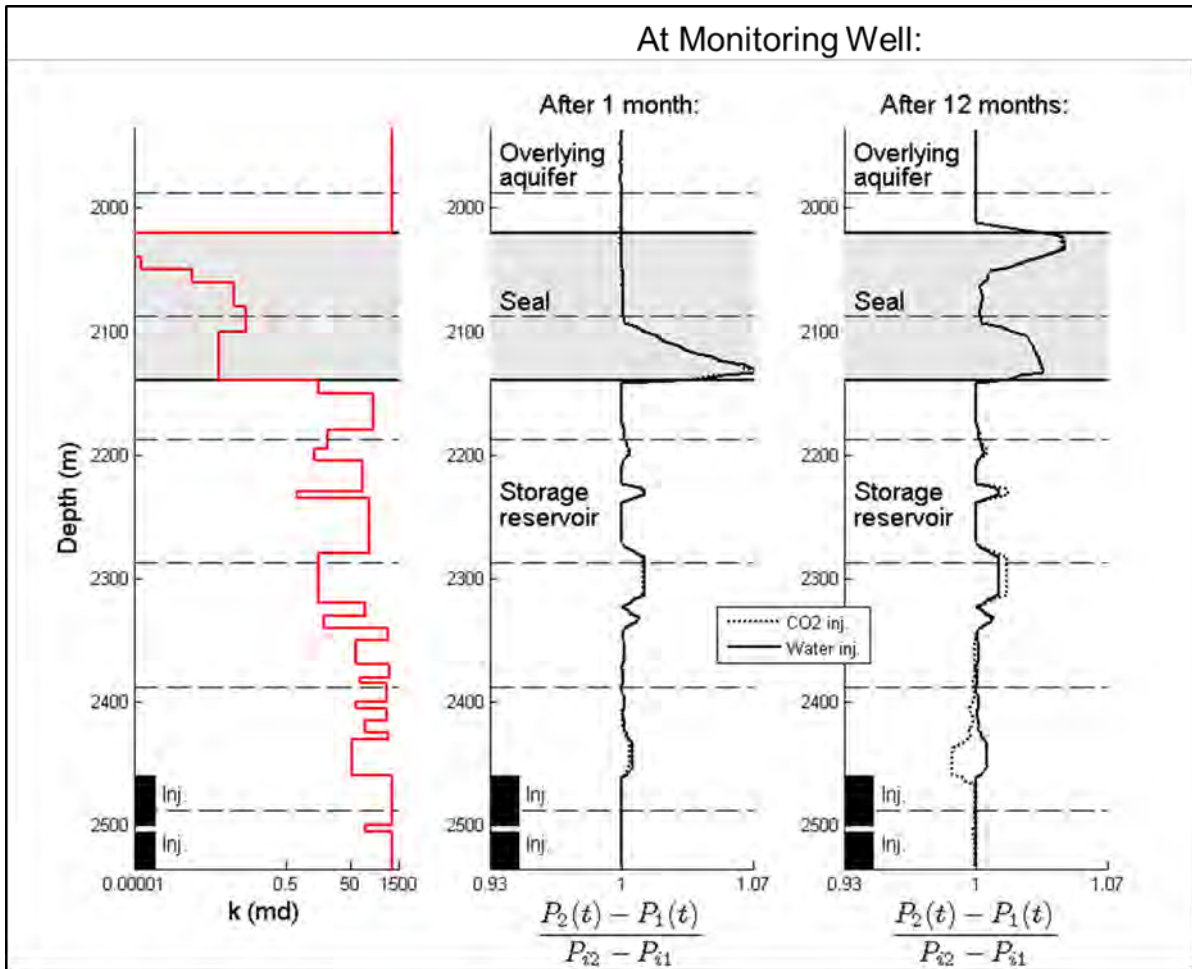
Figure 4.14: Heterogeneous isotropic scenario: Left: Permeability distribution for storage reservoir, seal, and overlying aquifer. Middle: Normalized vertical pressure gradients at the monitoring well after one month of injection, for CO_2 injection and pure water injection. Right: Normalized vertical pressure gradients after 12 months of injection, for CO_2 injection and pure water injection.

Figure 4.15 shows the position of the CO_2 plume with time, as well as the normalized vertical pressure gradients for the CO_2 injection case, from which the normalized vertical pressure gradients for the water injection case have been subtracted.

57

At the depths of the CO_2 plume in the storage reservoir there are some regions of negative normalized pressure gradient deviations. The maximum negative spike occurs at the depth at which the CO_2 reaches the monitoring well first, but the spike does not occur until just as the CO_2 arrives at the monitoring well. Directly above the large negative spike is a large positive spike. The positive spike also does not occur until just as the CO_2 arrives at the monitoring well. At some shallower depths in the storage reservoir there are some positive deviations, though the magnitudes of these are much smaller. In the seal there are some slight deviations in the upper and lower portions.
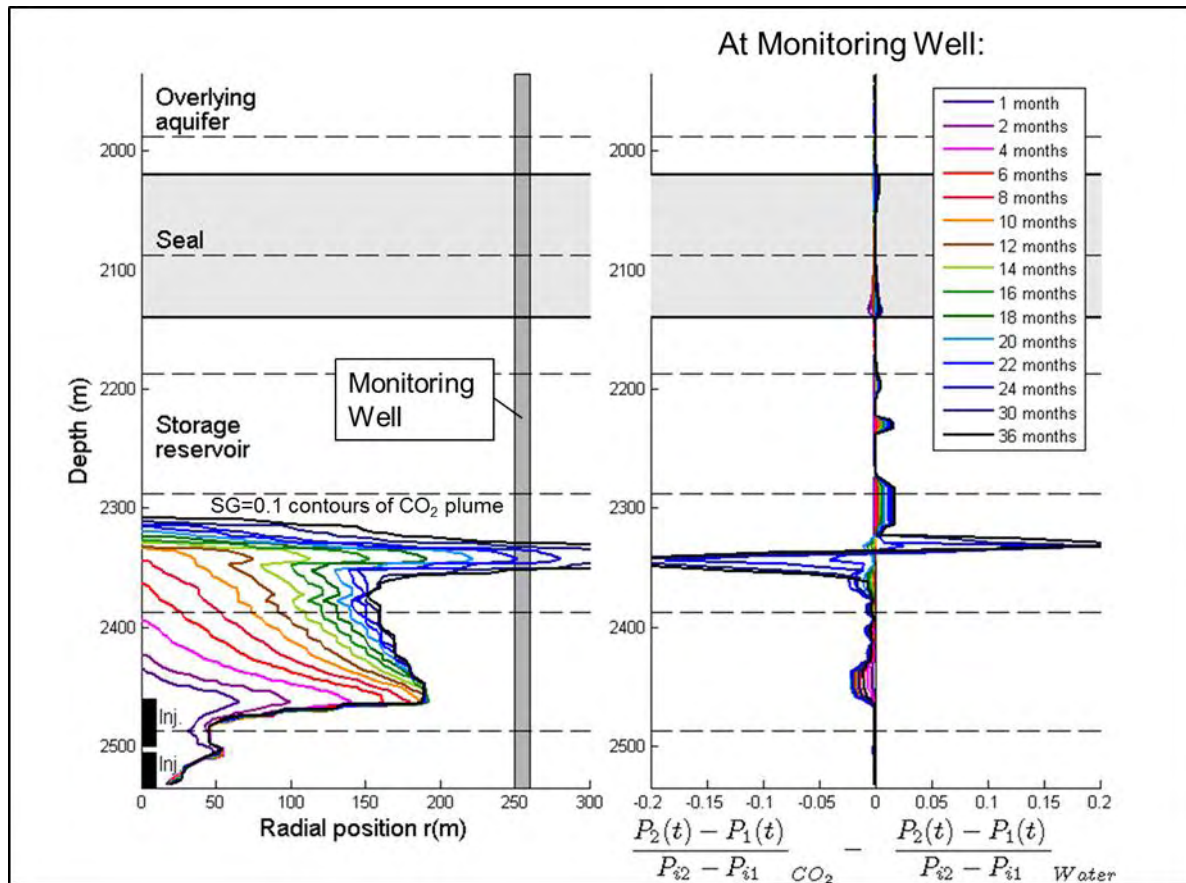
Figure 4.15: Heterogeneous isotropic scenario: Left: CO_2 plume contour as a function of position and time (a cutoff gas saturation SG of 0.1 defines the contour). Right: Normalized vertical pressure gradient deviations as a function of time (normalized vertical pressure gradients for CO_2 injection from which the normalized vertical pressure gradients for water injection have been subtracted).

58

4.4. Heterogeneous Anisotropic Scenario

Porosity and horizontal permeability distributions as functions of depth, along with the migration of the CO_2 plume, are shown in in Figure 4.16. Supercritical CO_2 is injected continuously over three years into two higher permeability layers at the bottom of the storage reservoir. Between the two higher permeability layers at the bottom there is a thin, lower permeability layer. From Figure 4.16 we see that the CO_2 plume, due to the lower vertical permeability, migrates mainly laterally in the reservoir. Because of the lower permeability layer between the two injection layers, the front of the plume splits into two lateral tongues, one for each higher permeability injection layer. The fastest part of the front of the plume reaches the monitoring well between 16 and 18 months after start of injection. Again, the six pressure monitoring points are illustrated by red markers, and their depths are indicated by dashed, horizontal lines.
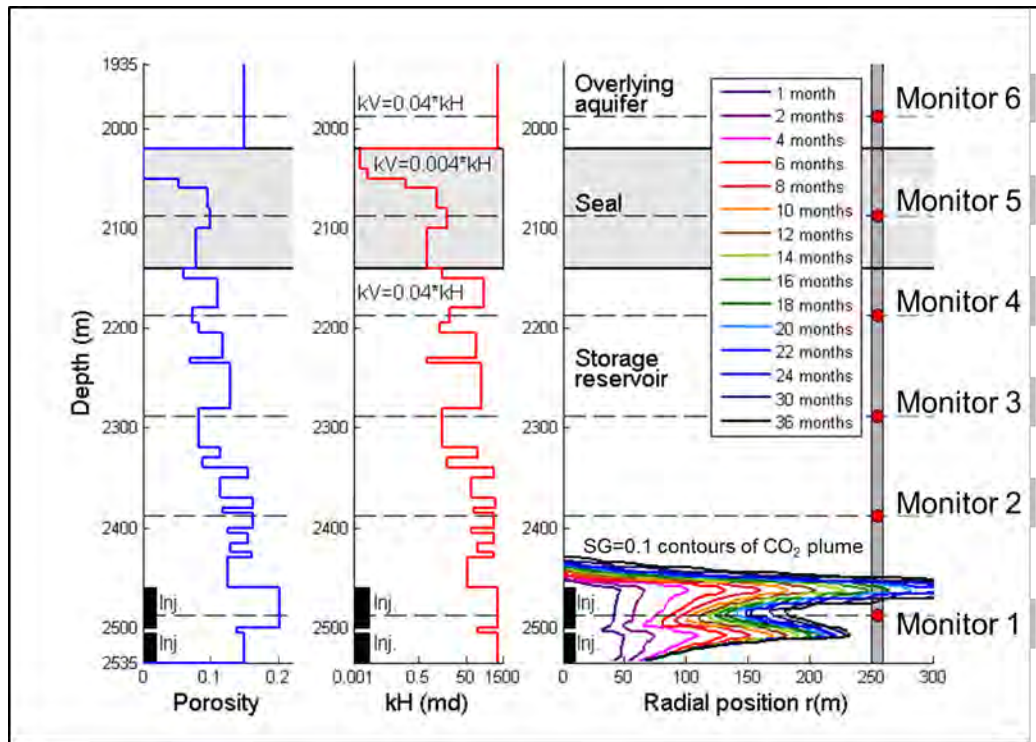
Figure 4.16: Heterogeneous anisotropic scenario: Left and Middle: Porosity (blue) and permeability (red) distributions for storage reservoir, seal, and overlying aquifer. Right: CO_2 plume contour as a function of position and time (a cutoff gas saturation SG of 0.1 defines the contour) and locations of the six pressure monitors in the monitoring well. Note that the black boxes indicating injection layers are drawn to scale only in the vertical direction.

4.4.1. Pressure Transients

Figure 4.17 shows the change in pressure transients for each of the six monitors; Figure 4.18 shows the pressure transients on logarithmic axes. In Figure 4.17 we show the full range of pressure responses; in Figure 4.18 we limit the range to pressure changes above the assumed detection limit of 0.001 MPa.
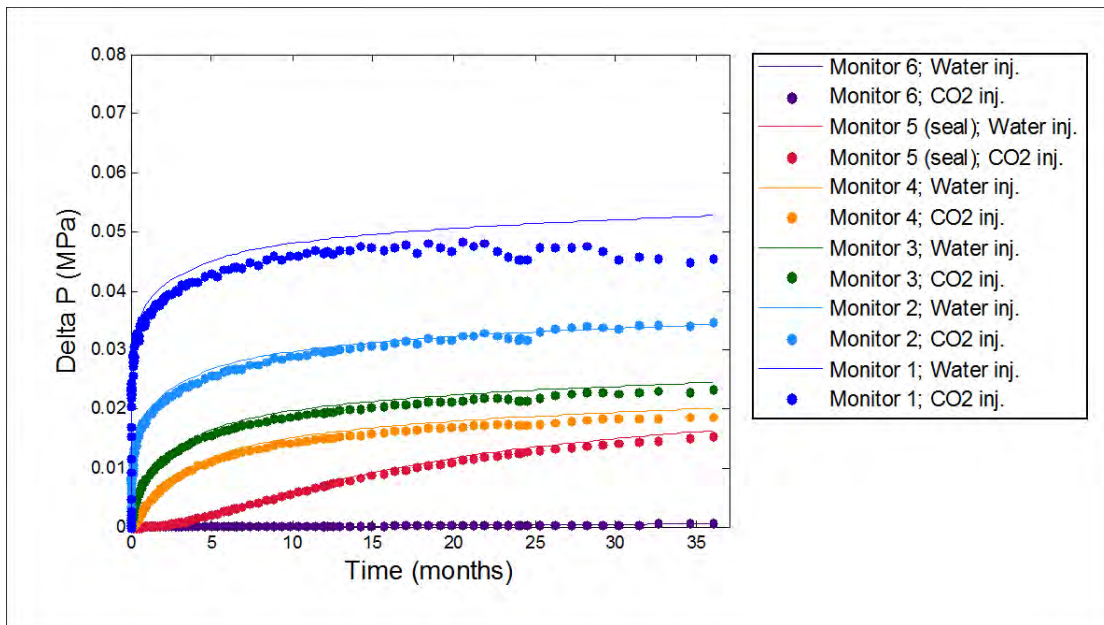
Figure 4.17: Pressure transients at Monitors 1-6 for the heterogeneous anisotropic scenario

Monitor 1, which is placed at the depth of injection, detects a pressure buildup of 0.03 MPa almost instantaneously. Over the course of injection, the pressure buildup at Monitor 1 exceeds 0.05 MPa for the pure water injection case. For the CO_2 injection case, the pressure buildup remains slightly less than the pressure buildup for the pure water injection case at all times.

Monitor 2, which is placed 75 m above the injection zone, detects an almost instantaneous pressure buildup of 0.01 MPa. In this case, the pressure buildups for the pure water injection case and the CO_2 injection case are almost identical. After three

years of injection, Monitor 1 measures a pressure buildup of about 0.05 MPa. Monitor 3 detects an almost instantaneous pressure buildup of 0.002. In this case also, the pressure buildups for the pure water injection case and the CO_2 injection case are almost identical. After three years of injection, Monitor 3 measures a pressure buildup of about 0.025 MPa.
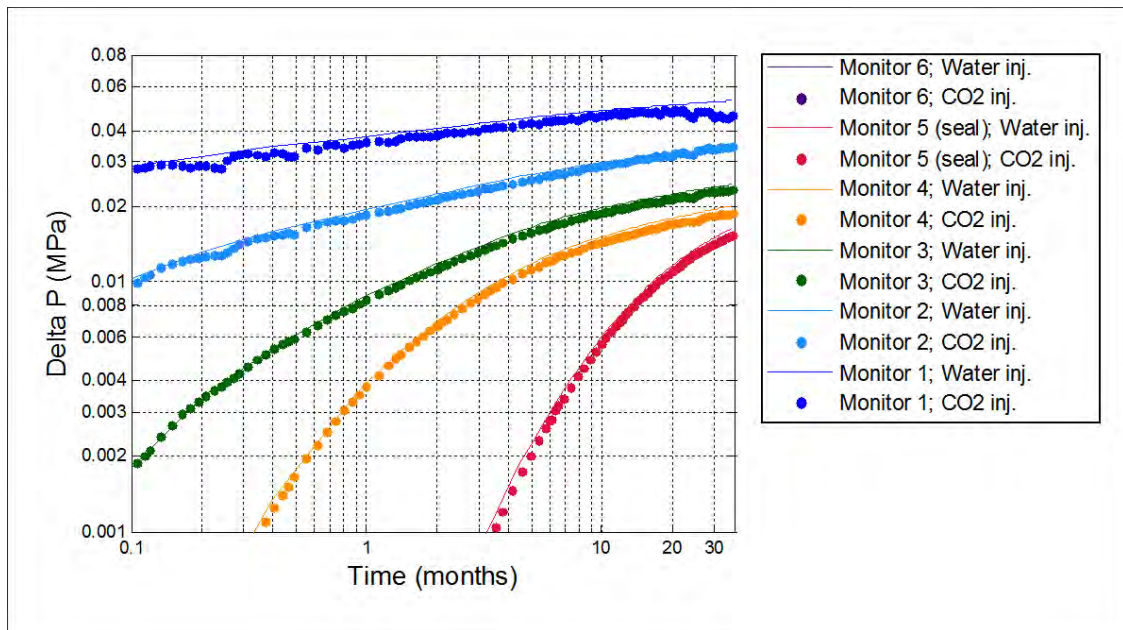
Figure 4.18: Pressure transients at Monitors 1-6 plotted on logarithmic axes for the heterogeneous anisotropic scenario

The pressure buildups at Monitors 4 and 5 may not be detected right away. The pressure buildup at Monitor 4, which is located 275 m above the injection zone, reaches the assumed detectable level after about 10 days of injection. After three years of injection, the pressure buildup at Monitor 4 has reached a magnitude of 0.02 MPa. Monitor 5, which is placed in the seal, measures a detectable pressure buildup after a little over 3 months of injection, which is after the CO_2 plume, in the case of CO_2 injection, has arrived at the monitoring well. For monitors 4 and 5 there is almost no deviation between pressure buildups for the all water injection case and the CO_2 injection case. No pressure buildup is detected by Monitor 6, which is located above the seal.

4.4.2. Vertical Pressure Gradients Normalized by Initial Hydrostatic Pressure

Figure 4.19 shows the vertical pressure gradients after one month and after 12 months of injection, as well as the horizontal permeability distribution as a function of depth.
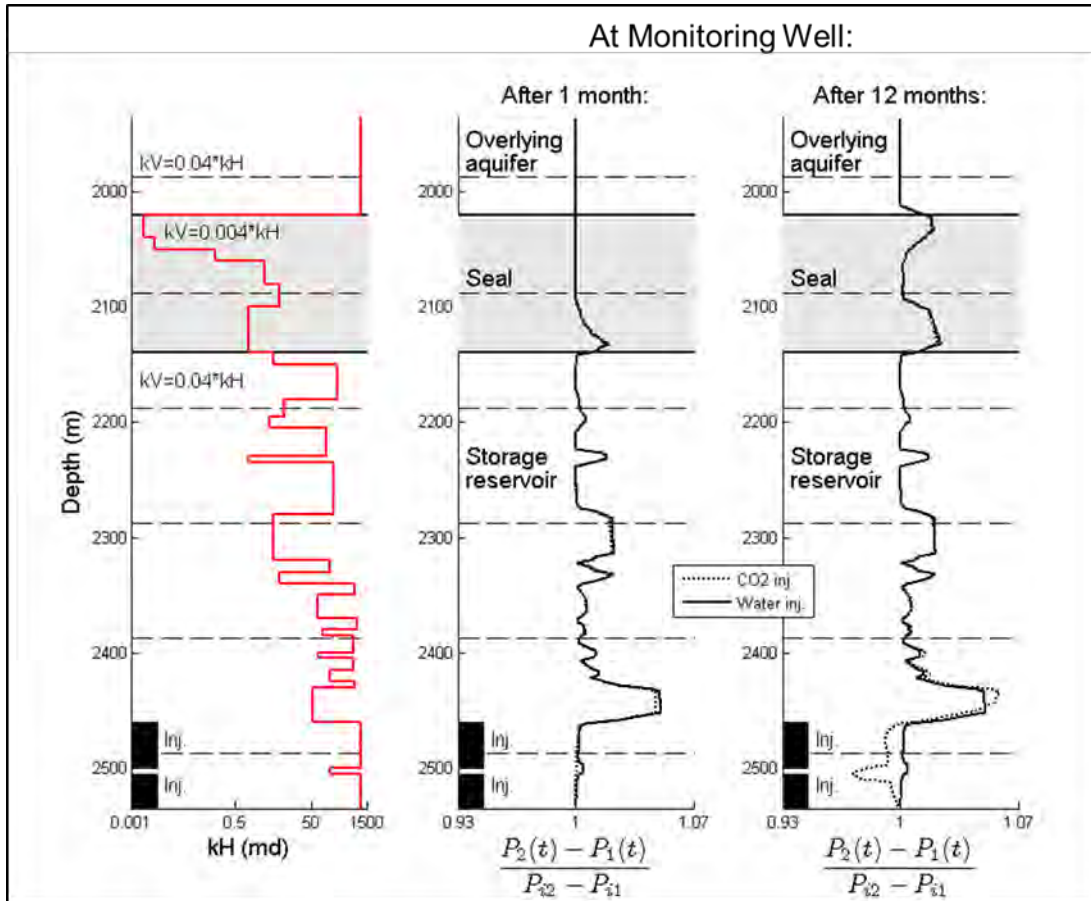
Figure 4.19: Heterogeneous anisotropic scenario: Left: Permeability distribution for storage reservoir, seal, and overlying aquifer. Middle: Normalized vertical pressure gradients at the monitoring well after one month of injection, for CO_2 injection and pure water injection. Right: Normalized vertical pressure gradients after 12 months of injection, for CO_2 injection and pure water injection.

After one month of injection there is only a very slight detectable difference between the CO_2 injection case and the water injection case. The differences occur at the depth of injection and slightly above. Where the two cases differ, the normalized vertical

pressure gradient is less for the CO_2 injection case than for the water injection case. At all other depths there is no detectable difference between the normalized vertical pressure gradient for the CO_2 injection case and the water injection case. There is nevertheless a multiple of positive anomalies at many depths in the storage reservoir. Also, in the lower part of the seal, there is a sharp, positive anomaly in the normalized vertical pressure gradient.

After 12 months of injection we see a greater deviation between the CO_2 injection case and the pure water injection case, at the same depths at which we detected a slight difference after one month of injection, namely at the depth of injection and just above. At the depth of injection, the normalized vertical pressure gradient is less for the CO_2 injection case than for the water injection case. Just above the zone of injection, the normalized vertical pressure gradient is slightly greater for the CO_2 injection case than for the water injection case. For the remaining depths in the storage reservoir, there is no difference between the CO_2 injection case and the water injection case, and the positive anomalies occur at the same depths as they did after one month of injection. In the seal, however, the spike in the normalized vertical pressure gradient that we saw after one month of injection is gone; instead there are two zones of large, positive normalized pressure gradients.

Figure 4.20 shows the position of the CO_2 plume with time, as well as the normalized vertical pressure gradients for the CO_2 injection case, from which the normalized vertical pressure gradients for the water injection case have been subtracted. At the depths of the CO_2 plume in the storage reservoir there are negative normalized pressure gradient deviations. The maximum negative spike occurs at the depth at which the CO_2 reaches the monitoring well first, but, the spike does not become prominent until just as the CO_2 arrives at the monitoring well. Directly above the large negative spike is a large positive spike. Again, the spike does not occur until just as the CO_2 reaches the monitoring well.
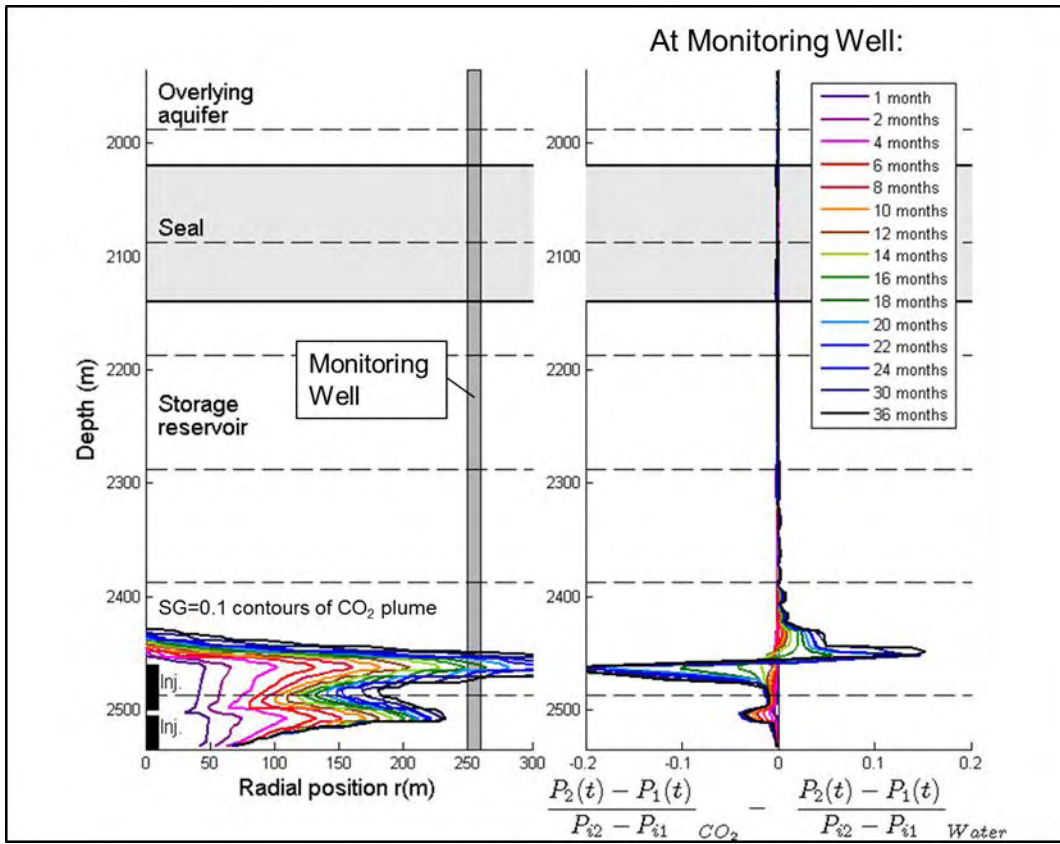
Figure 4.20: Heterogeneous anisotropic scenario: Left: CO_2 plume contour as a function of position and time (a cutoff gas saturation SG of 0.1 defines the contour). Right: Normalized vertical pressure gradient deviations as a function of time (normalized vertical pressure gradients for CO_2 injection from which the normalized vertical pressure gradients for water injection have been subtracted).

Chapter 5

5. Analysis

In the following section we analyze the results presented in Section 4. First, we examine the magnitudes of the pressure transients and compare the pressure buildup at each monitoring point for all four scenarios of homogeneity/heterogeneity and isotropy/anisotropy, for pure CO_2 injection and for pure water injection. Second, we investigate the information that can be obtained about the heterogeneity of the system and the location of the CO_2 plume from vertical pressure gradients. Third, we relate anomalies in the vertical pressure gradients to anomalous vertical aqueous flow. Finally, we use the information obtained to discuss the placement of vertically distributed pressure monitors.

5.1. Pressure Transients

Figures 5.1 and 5.2 compare the pressure transients at Monitor 1 for the four different scenarios. Initially, the pressure buildups range from 0.02 MPa to 0.045 MPa. After three years of injection, the pressure buildups range from 0.035 MPa to 0.07 MPa. All pressure buildups are large and detectable, and all four scenarios have distinctly different pressure buildups, suggesting that system heterogeneity strongly influences the pressure response. The pressure buildup is less for the CO_2 injection case than for the water injection case for all four scenarios. For the homogeneous anisotropic scenario, a distinct negative anomaly for the CO_2 injection case develops after five months of injection. If we reexamine Figures 4.6 and 4.10, we see that Monitor 1 is located at a depth adjacent to or just below the maximum lateral extent of the CO_2 plume.
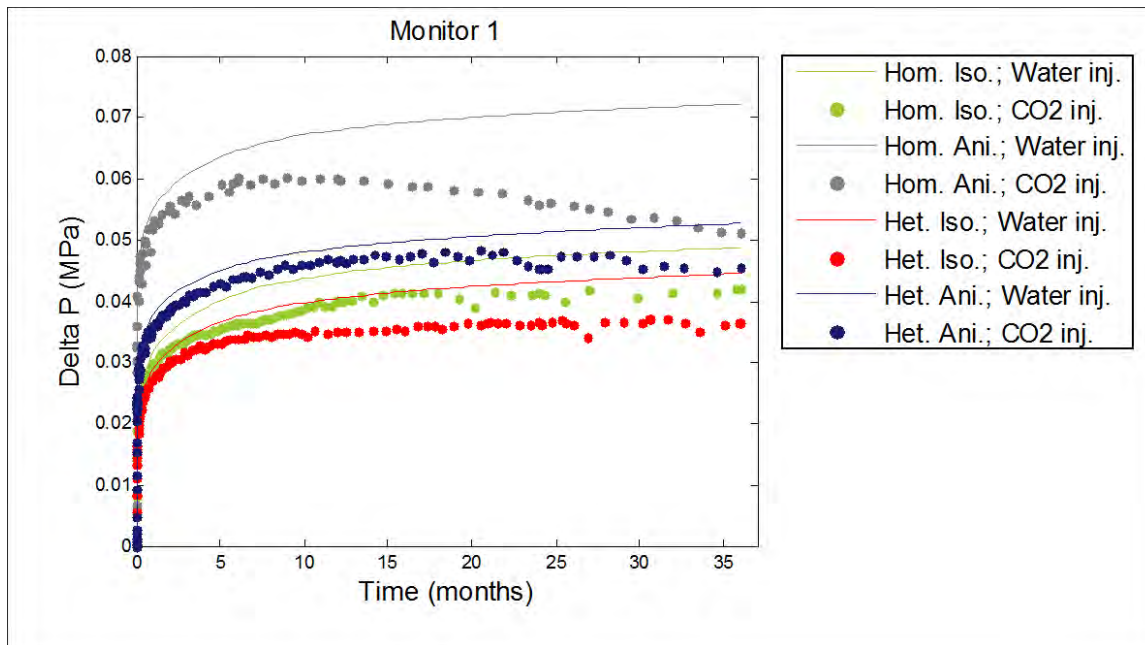
Figure 5.1: Pressure transients at Monitor 1 for all four heterogeneity/anisotropy scenarios for CO_2 injection and water injection
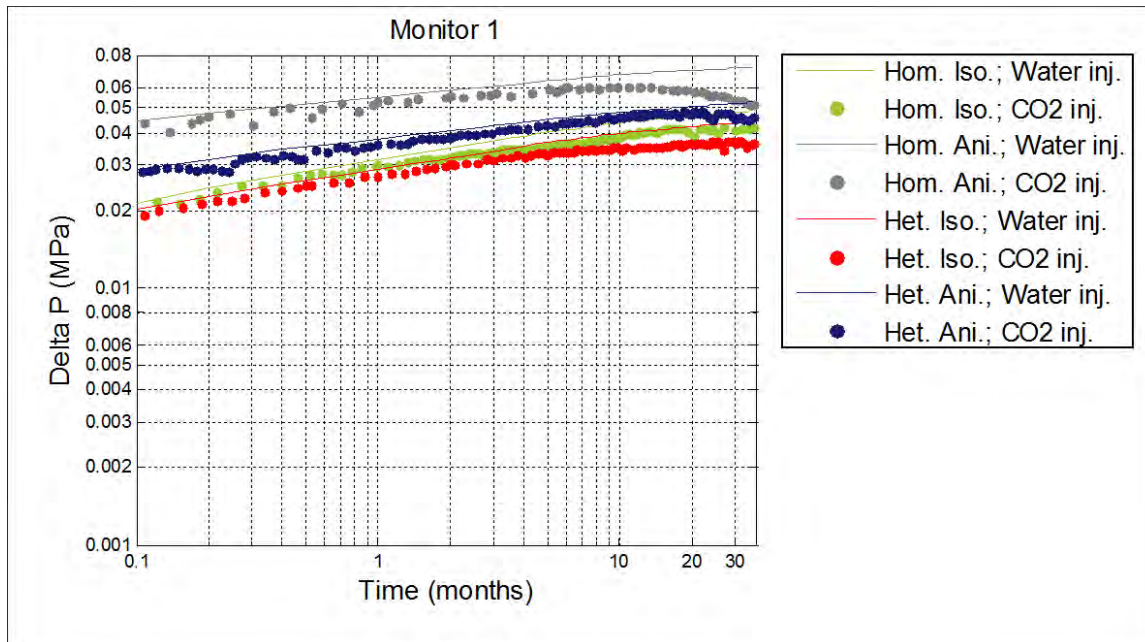
Figure 5.2: Pressure transients at Monitor 1 plotted on logarithmic axes for all four heterogeneity/anisotropy scenarios for CO_2 injection and water injection

66

Figures 5.3 and 5.4 compare the pressure buildups at Monitor 2. At this depth, the initial pressure buildups range from 0.01 MPa to 0.02 MPa. After three years of injection, the pressure buildups range from 0.035 MPa to about 0.055 MPa. Again, the pressure buildups for all scenarios are large and measureable. For the two isotropic scenarios, there appears to be no significant difference in the pressure behavior. For the water injection case, the pressure buildup is consistently somewhat less for the heterogeneous isotropic scenario than for the homogeneous isotropic scenario. For the CO_2 injection case, however, the pressure responses appear almost identical. For the first 15 months of injection, the pressure response for the homogeneous anisotropic scenario is similar to the pressure response for the two isotropic cases, but after 15 months of injection, a positive anomaly develops for the CO_2 injection case for the homogeneous anisotropic scenario. If we reexamine Figures 4.6 and 4.10, we see that the positive pressure anomaly occurs when the monitor is located at a depth slightly shallower than or at the same depth as the height of the CO_2 plume. For the heterogeneous anisotropic scenario, the pressure buildup is consistently less than for the other three scenarios. For the heterogeneous anisotropic scenario, there appears to be no difference in pressure response for the CO_2 injection case and the water injection case. If we reexamine Figures 4.16 and 4.20, we see that Monitor 2 is located about 50 m above the maximum vertical extent of the CO_2 plume in the heterogeneous anisotropic scenario.
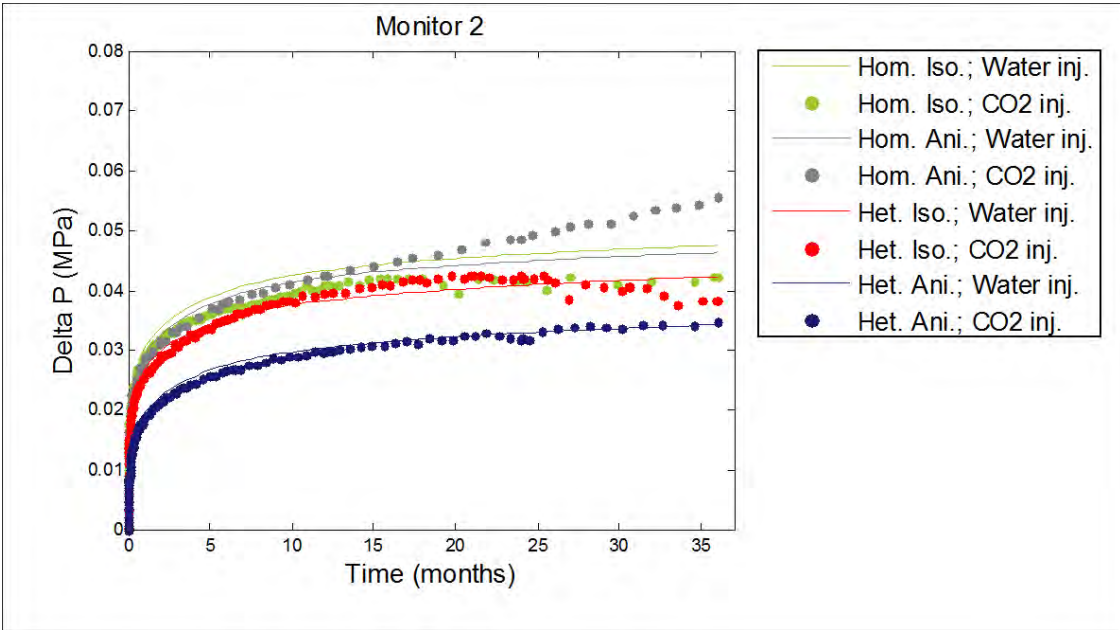
Figure 5.3: Pressure transients at Monitor 2 for all four heterogeneity/anisotropy scenarios for CO_2 injection and water injection
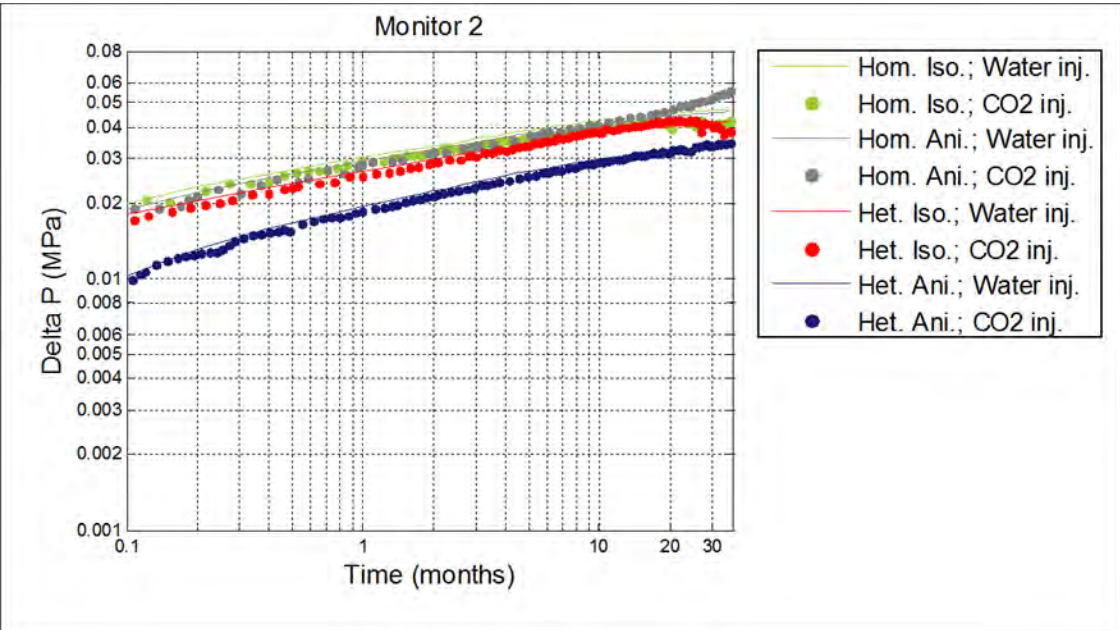
Figure 5.4: Pressure transients at Monitor 2 plotted on logarithmic axes for all four heterogeneity/anisotropy scenarios for CO_2 injection and water injection

68

Figures 5.5 and 5.6 show the pressure buildups at Monitor 3. At this depth, the initial pressure buildups range from 0.002 MPa to 0.02 MPa. After three years of injection, the pressure buildups range from about 0.024 MPa to 0.045 MPa. The pressure buildup is largest for the homogeneous isotropic scenario. The pressure buildup is less, but similar, for the homogeneous anisotropic and heterogeneous isotropic scenarios, and much less for the heterogeneous anisotropic case. Only for the heterogeneous isotropic scenario is there a distinct anomaly in the pressure response for the CO_2 injection case. The positive, anomalous pressure response starts to develop after 15 months of injection. If we reexamine Figures 4.16 and 4.20, we see that the positive pressure anomaly for the CO_2 injection case occurs when the monitor is located at a depth slightly shallower than the maximum vertical extent of the CO_2 plume.
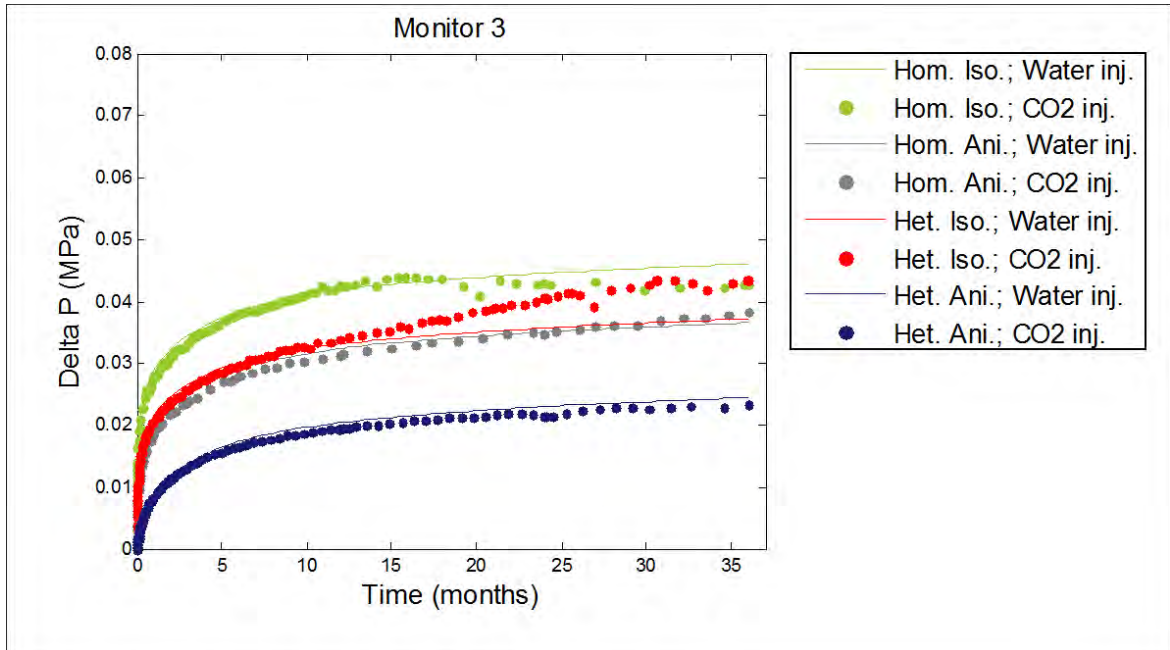
Figure 5.5: Pressure transients at Monitor 3 for all four heterogeneity/anisotropy scenarios for CO_2 injection and water injection
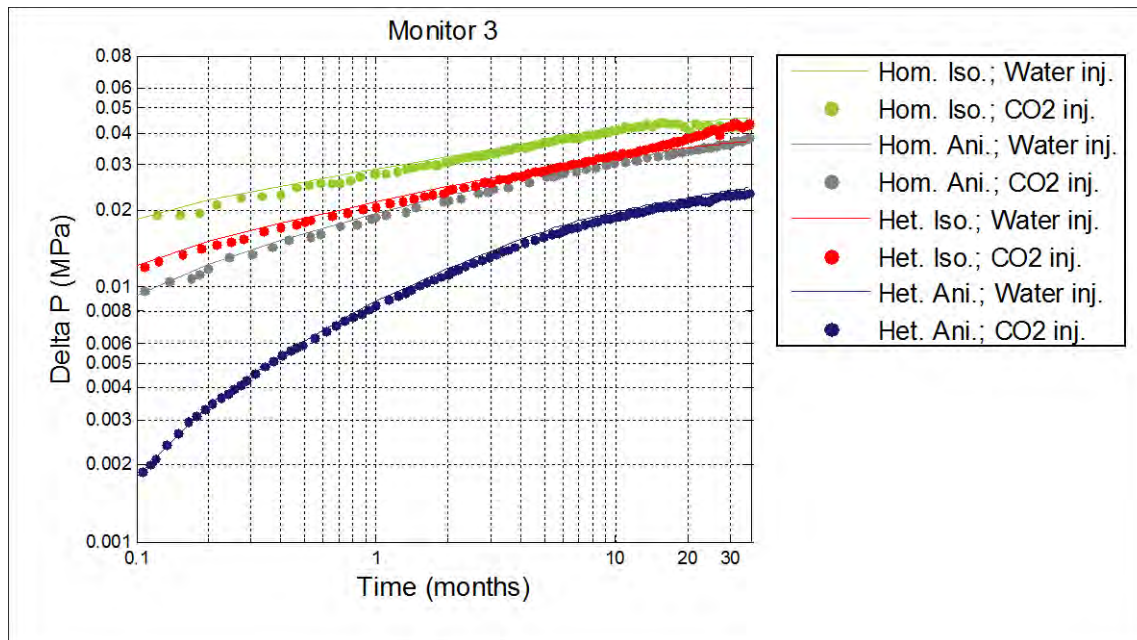
Figure 5.6: Pressure transients at Monitor 3 plotted on logarithmic axes for all four heterogeneity/anisotropy scenarios for CO_2 injection and water injection

Figures 5.7 and 5.8 show the pressure buildups at Monitor 4. At this depth, the initial pressure buildups range from less than the conservative detection limit to almost 0.02 MPa. After three years of injection, the pressure buildups range from 0.02 MPa to 0.045 MPa. After about 10 days of injection, the pressure buildups are large and measurable for all four scenarios. As for Monitor 3, the pressure buildup is largest for the homogeneous isotropic scenario. The pressure buildup is less, but similar, for the homogeneous anisotropic and heterogeneous isotropic scenarios, and much less for the heterogeneous anisotropic case. At Monitor 4, there is a positive anomaly in the pressure response for the homogeneous isotropic scenario for the CO_2 injection case. This positive pressure anomaly occurs after 15 months of injection. Reexamining Figures 4.1 and 4.5, we see that the positive pressure anomaly occurs just before and as the CO_2 plume arrives at the monitoring well. In this case, the monitor is located at a depth just below the upper, most laterally extensive, part of the CO_2 plume.

70
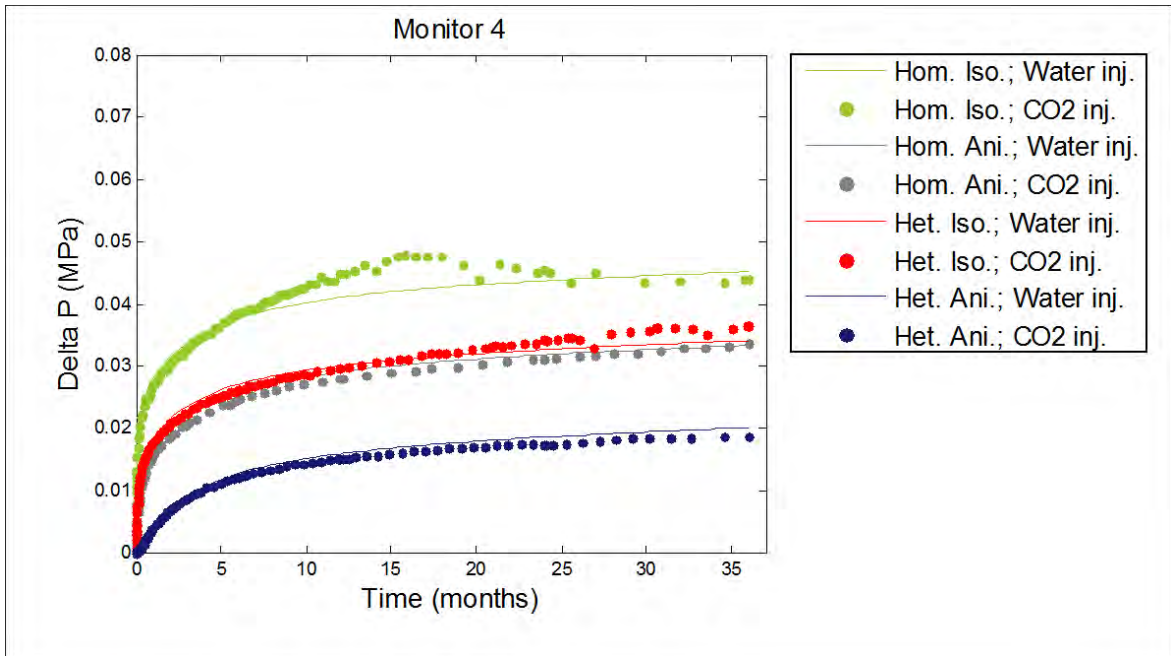
Figure 5.7: Pressure transients at Monitor 4 for all four heterogeneity/anisotropy scenarios for CO_2 injection and water injection
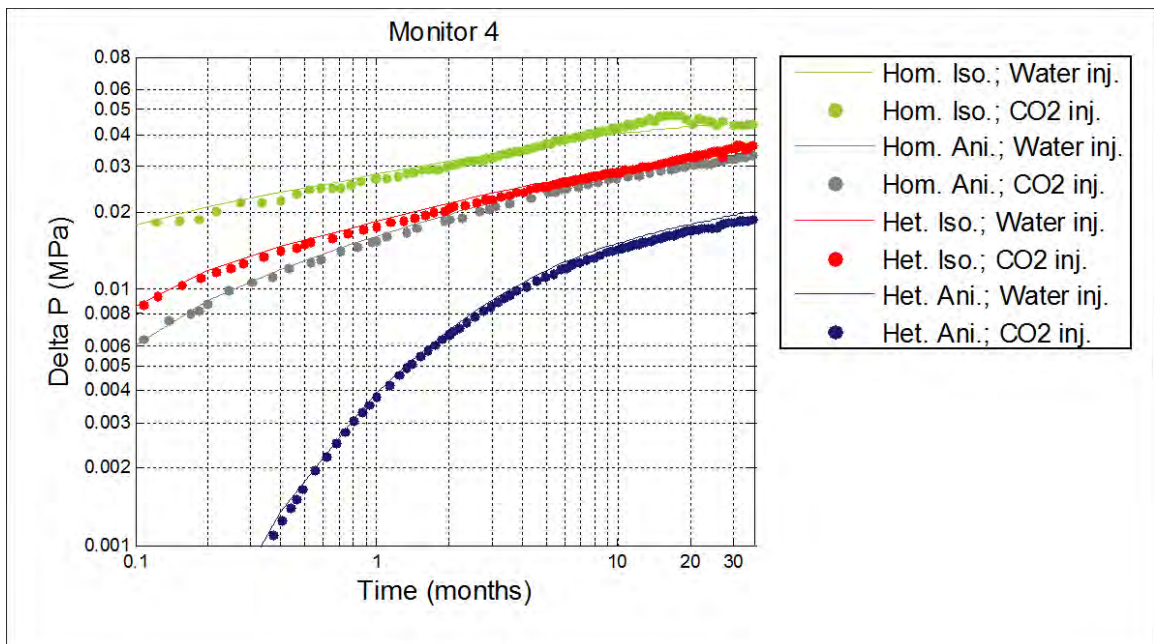
Figure 5.8: Pressure transients at Monitor 4 plotted on logarithmic axes for all four heterogeneity/anisotropy scenarios for CO_2 injection and water injection

Figures 5.9 and 5.10 show the pressure buildups in the seal at Monitor 5. At this location, the initial pressure buildups are less than the detection limit of 0.001 MPa for all four scenarios. After about two weeks of injection, the pressure buildup is greater than the detection limit for the homogeneous isotropic scenario. After three weeks of injection, the pressure buildup exceeds the detection limit for the homogeneous anisotropic scenario; after one and a half months the pressure buildup exceeds the detection limit for the heterogeneous isotropic case; and after a little more than three months the pressure buildup exceeds the detection limit for the heterogeneous anisotropic scenario. After three years of injection, the pressure buildups range from 0.015 MPa to 0.06 MPa. For the heterogeneous and homogeneous isotropic scenarios, the pressure buildups are nearly identical for the CO_2 injection case and the pure water injection case. For the homogeneous isotropic scenario, the pressure buildup for the CO_2 injection case starts to deviate from that of the water injection case after nine months of injection. After 15 months of injection there is a significant positive pressure anomaly for the CO_2 injection case. At this time, the upper portion of the CO_2 plume is migrating laterally just below the seal and just below the position of Monitor 5 (Figures 4.1 and 4.5).
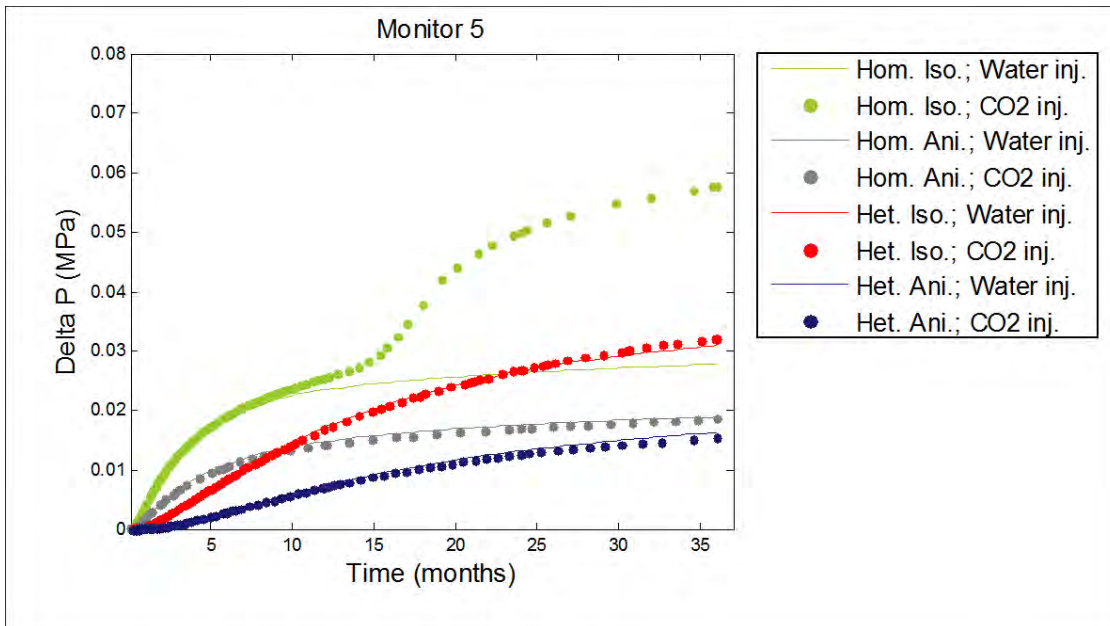
Figure 5.9: Pressure transients at Monitor 5 for all four heterogeneity/anisotropy scenarios for CO_2 injection and water injection
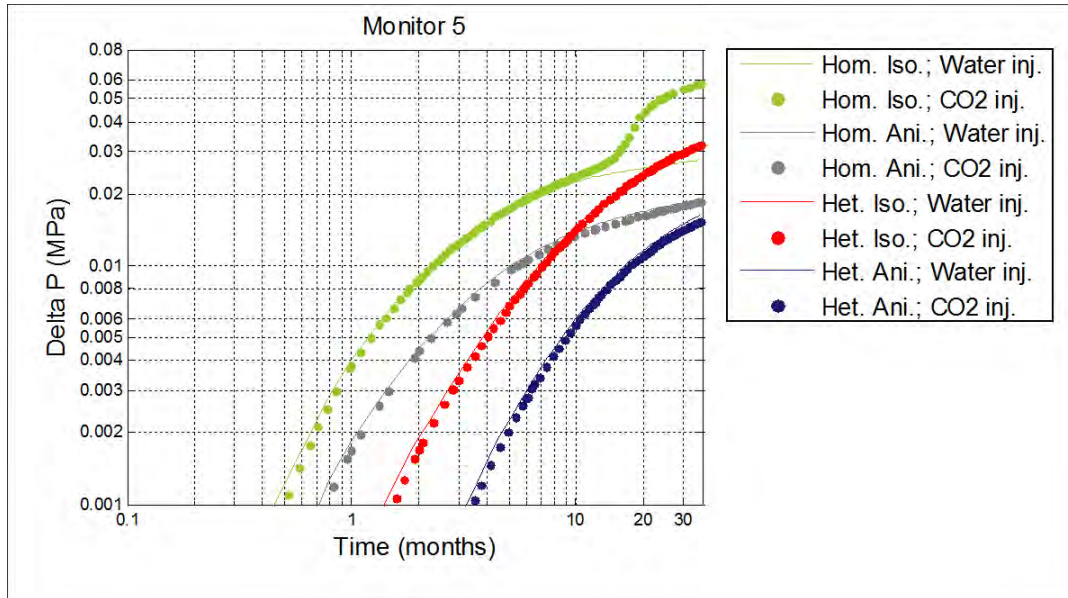
Figure 5.10: Pressure transients at Monitor 5 plotted on logarithmic axes for all four heterogeneity/anisotropy scenarios for CO_2 injection and water injection

Figures 5.11 and 5.12 show the pressure buildups at Monitor 6, which is located above the seal. At this location, the pressure buildup is less than the detection limit of 0.001 MPa for the heterogeneous scenarios during the entire time of simulation. For the homogeneous scenarios, the pressure buildup exceeds the detection level after nine months of injection. We see that the pressure buildups for the two heterogeneous scenarios are almost identical and that the same holds for the two homogeneous scenarios. Also, the pressure buildup for the heterogeneous scenarios is consistently less than the pressure buildup for the homogeneous scenarios, again suggesting that heterogeneity dominates the general trend in pressure response.
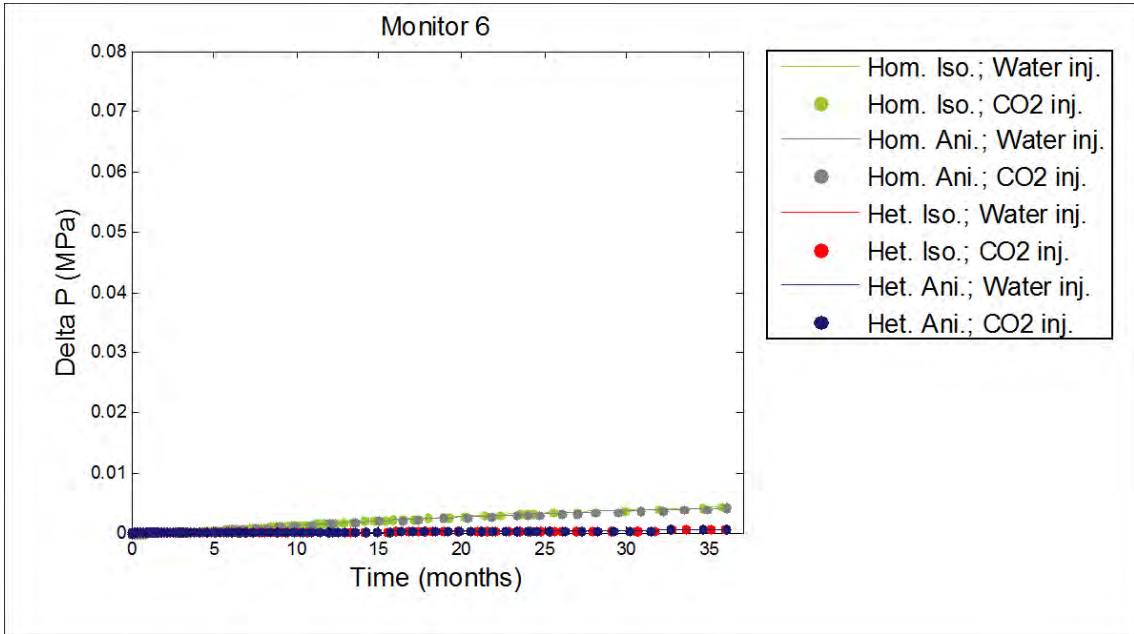
Figure 5.11: Pressure transients at Monitor 6 for all four heterogeneity/anisotropy scenarios for CO_2 injection and water injection
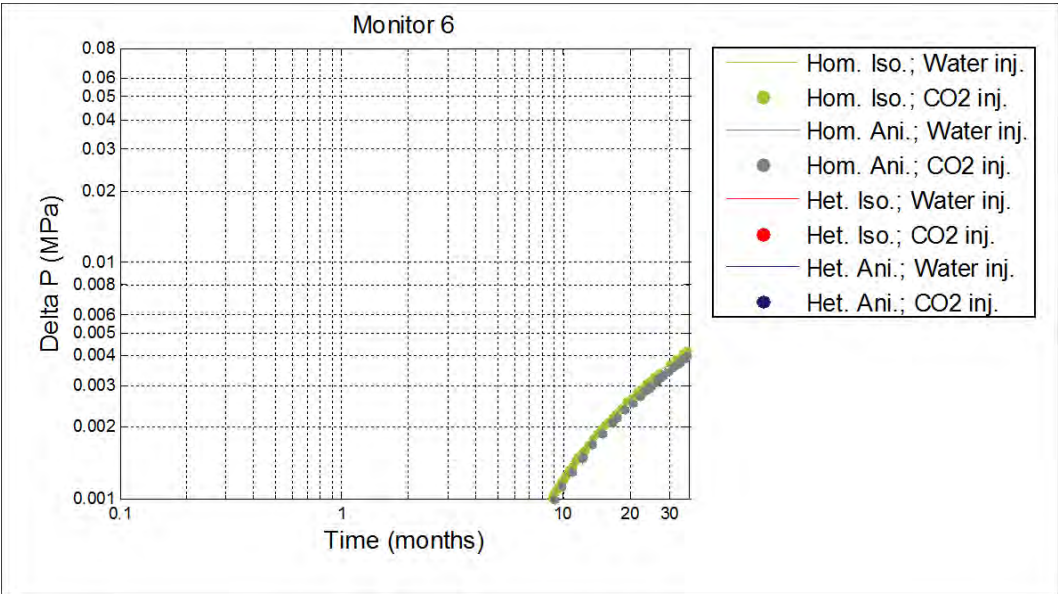
Figure 5.12: Pressure transients at Monitor 6 plotted on logarithmic axes for all four heterogeneity/anisotropy scenarios for CO_2 injection and water injection

74

In summary, unless there is a seal separating the monitoring zone from the storage reservoir, large pressure changes can be observed. Distinct pressure transients for the different system scenarios suggest that system heterogeneity greatly impacts the pressure response. However, pressure transients alone appear not to be very useful for capturing the nature of the heterogeneity of the system or the location of the CO_2 plume.

First, for the cases where there are no distinct pressure anomalies, it is difficult to know when the observed pressure change is due to CO_2 being present in the system and when it is a response to water flow. We have seen that the general trend in pressure transients is similar for CO_2 injection and pure water injection.

Second, although we detected pressure anomalies at monitors close to the location at which the CO_2 plume reaches the monitoring well for the homogeneous and the heterogeneous isotropic scenarios, we did not detect distinct pressure anomalies for the heterogeneous anisotropic scenario. Without any prior knowledge of the reservoir or the location of the CO_2 plume, it is hard to interpret these pressure anomalies. The exception is for the homogeneous isotropic scenario, where there is a very distinct and large-magnitude positive pressure anomaly occurring in the seal, just above the upper part of the gravity tongue formed by the CO_2 plume. In this case there is no doubt that the pressure response is due to CO_2 having migrated to just below the seal. In reality, however, no reservoir is homogeneous and isotropic.

5.2. Normalized Vertical Pressure Gradients

Normalized vertical pressure gradients provide 1) a clear representation of the system heterogeneity at least as early as one month after start of injection, 2) distinct, separate features depending on whether CO_2 is present in the system, and 3), a strong indication of where the CO_2 is in the reservoir, i.e. at what depth, before the CO_2 arrives at the monitoring well.

If we reexamine Figures 4.4, 4.9, 4.14, and 4.19, where the normalized vertical pressure gradients are plotted after one month of injection, we see that normalized vertical pressure gradients greater than 1 indicates layers of low permeability. The greater the anisotropy, the more detailed and distinct these features are.

If we reexamine the normalized vertical pressure gradients plotted after 12 months of injection (Figures 4.4, 4.9, 4.14, and 4.19), and compare this with the CO_2 plume contours in Figures 4.1, 4.6, 4.11, and 4.16, we see that a normalized vertical pressure gradient less than 1 indicates presence of CO_2 at that depth. As can been seen from the homogeneous anisotropic scenario, the normalized vertical pressure gradient does not need to be less than 1 to indicate presence of CO_2; it suffices that the normalized pressure gradient is less than what it would have been for the all water case. An important remark to make here is that one month after start of injection the normalized vertical pressure gradient profile is almost the same for the CO_2 injection case as for the water injection case. The normalized vertical pressure gradients for the all water case appear not to change after the initial pressure buildup. In other words, there is a strong indication that CO_2 is present at a given depth in the reservoir if the normalized vertical pressure gradient at that depth has decreased from its initial value.

Based on the reasoning above, one can subtract the normalized vertical pressure gradients for the all water case from the normalized vertical pressure gradients for the CO_2 injection case; any resulting anomalies in the normalized vertical pressure gradient deviation should be due to CO_2 being present in the system. If we reexamine Figures 4.5, 4.10, 4.15, and 4.20, it is clear that the normalized vertical pressure gradient deviation is negative at depths adjacent to the CO_2 plume and positive at depths adjacent to the uppermost part of the CO_2 plume and above.

5.3. Vertical Aqueous Flow

Here we show that the anomalous vertical pressure gradient profiles described in Section 5.2 can be attributed to buoyancy induced flows when CO_2 is injected into the storage reservoir. Above the CO_2 plume, buoyancy induced flow causes anomalous upward flow of water. Within the plume, countercurrent flow of water and CO_2 causes anomalous downwards flow of water. This in turn induces downward flows in the region beneath the plume of CO_2. Figures 5.13 to 5.16 show contour plots of the vertical aqueous flow (kg/s) in the entire system for each of the four scenarios 12 months after start of injection. In Figures 5.13 - 5.16, the upper left plot shows the vertical aqueous flow for pure CO_2

injection, along with the contour of the CO_2 plume. The upper right plot shows the vertical aqueous flow for the all water case, with the dashed line indicating where the CO_2 plume would have been for the CO_2 injection case. Finally, the lowermost plot displays the vertical flow for the CO_2 injection case from which the vertical flow for the all water case has been subtracted. Because the there is only upward flow in the all water case, the lowermost plot displays a diminished upward flow and an exaggerated downward flow compared to that for the pure CO_2 injection case. The trend is nevertheless the same as for the CO_2 injection case.

If we compare the lowermost plots in Figures 5.13 to 5.16 with the normalized vertical pressure gradient deviations in Figures 4.5, 4.10, 4.15, and 4.20, we see that negative normalized vertical pressure gradient deviations correspond to downward flow at the monitoring well, whereas positive normalized vertical pressure deviations correspond to upward flow at the monitoring well. An important not to make here, with regard to Figures 4.5 and 5.13 (homogeneous isotropic scenario), is that the vertical pressure gradient is also a function of vertical permeability. Hence, for the homogeneous isotropic scenario, the normalized vertical pressure gradient deviation in the lower portions of the storage reservoir is zero, even though the contour plot of the vertical aqueous flow deviation shows significant downward flow in this region. The homogeneous and isotropic storage reservoir is permeable and does not offer much resistance to flow.
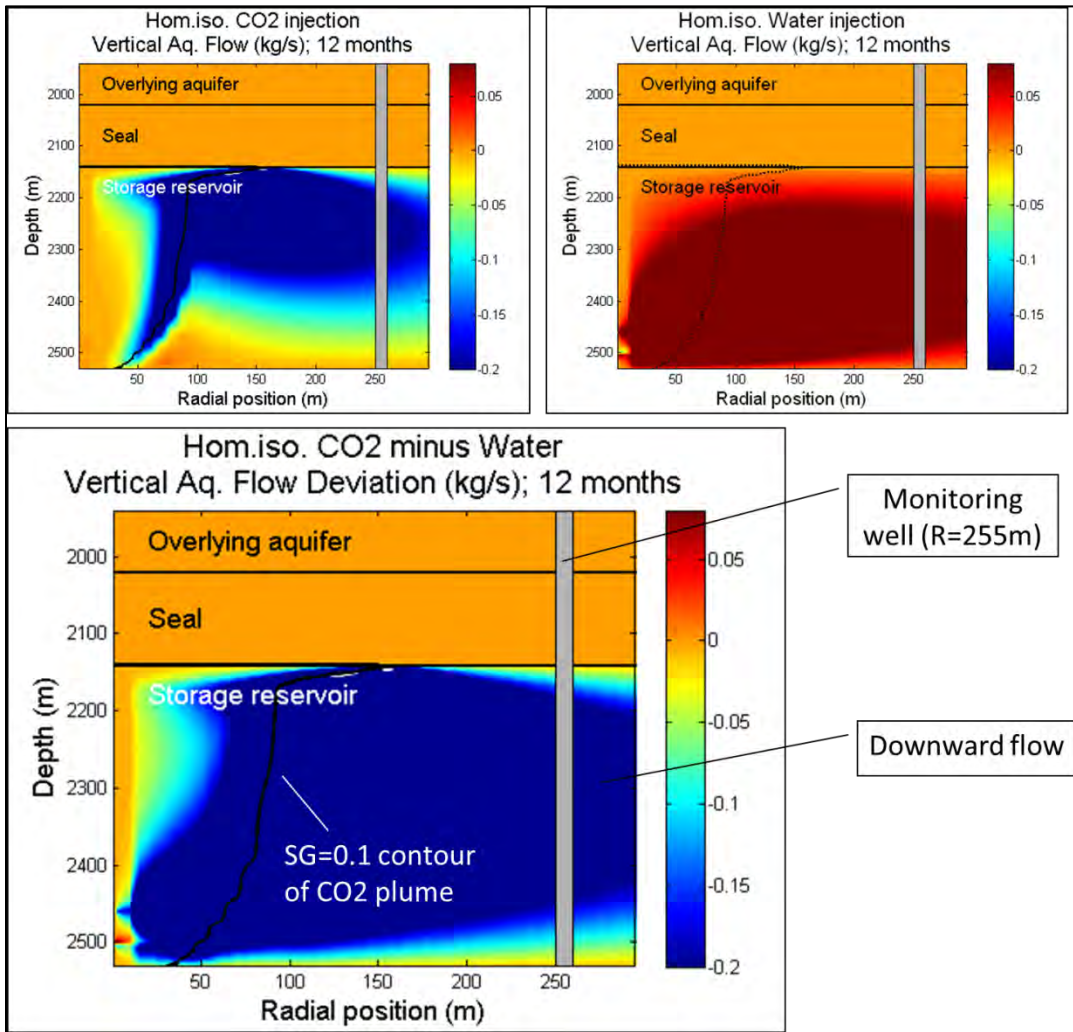
Figure 5.13: Vertical aqueous flow for the homogeneous isotropic scenario. Negative values indicate downward flow; positive values indicate upward flow. Upper left: Vertical flow after 12 months of CO_2 injection. Upper right: Vertical flow after 12 months of water injection. Bottom: Vertical flow for CO_2 injection from which the vertical flow for water injection has been subtracted.
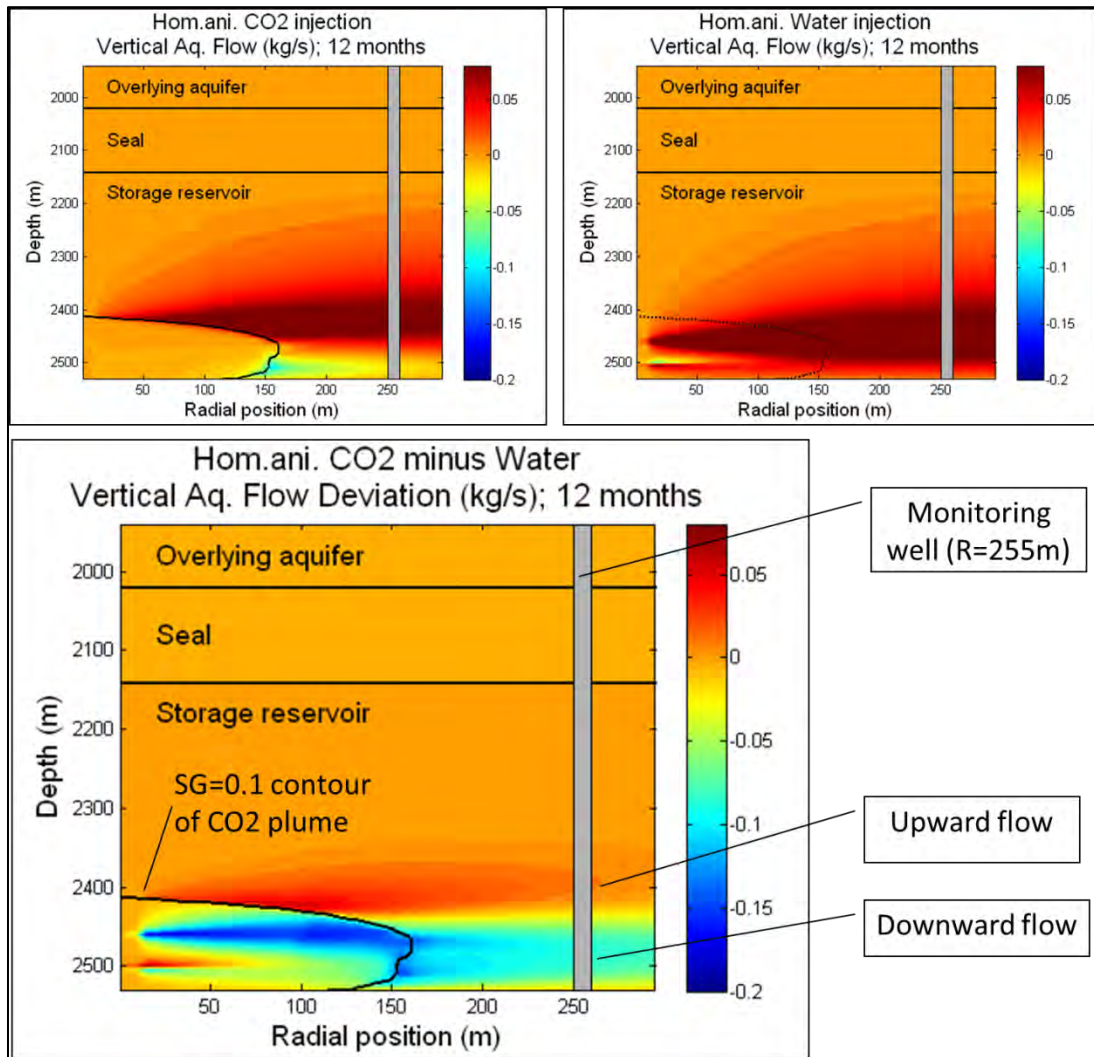
Figure 5.14: Vertical aqueous flow for the homogeneous anisotropic scenario. Negative values indicate downward flow; positive values indicate upward flow. Upper left: Vertical flow after 12 months of CO_2 injection. Upper right: Vertical flow after 12 months of water injection. Bottom: Vertical flow for CO_2 injection from which the vertical flow for water injection has been subtracted.
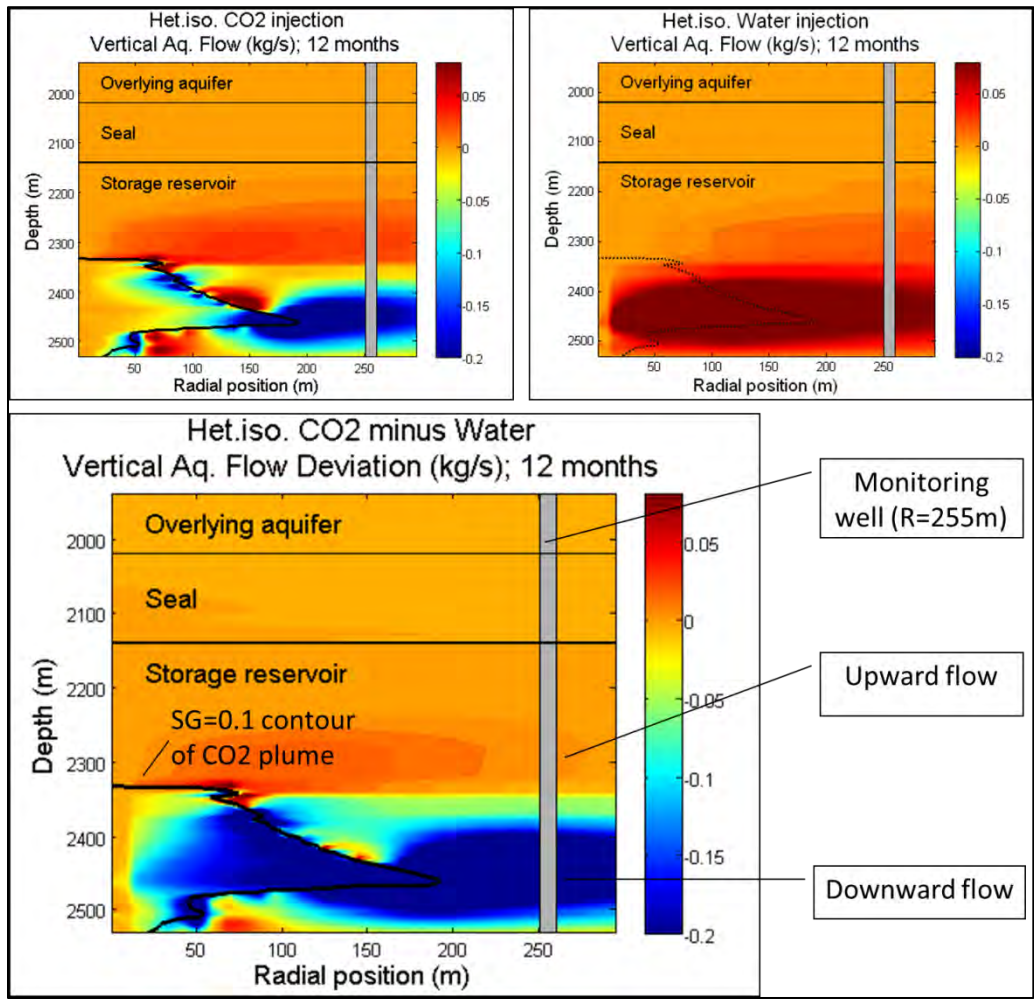
Figure 5.15: Vertical aqueous flow for the heterogeneous isotropic scenario. Negative values indicate downward flow; positive values indicate upward flow. Upper left: Vertical flow after 12 months of CO_2 injection. Upper right: Vertical flow after 12 months of water injection. Bottom: Vertical flow for CO_2 injection from which the vertical flow for water injection has been subtracted.

80
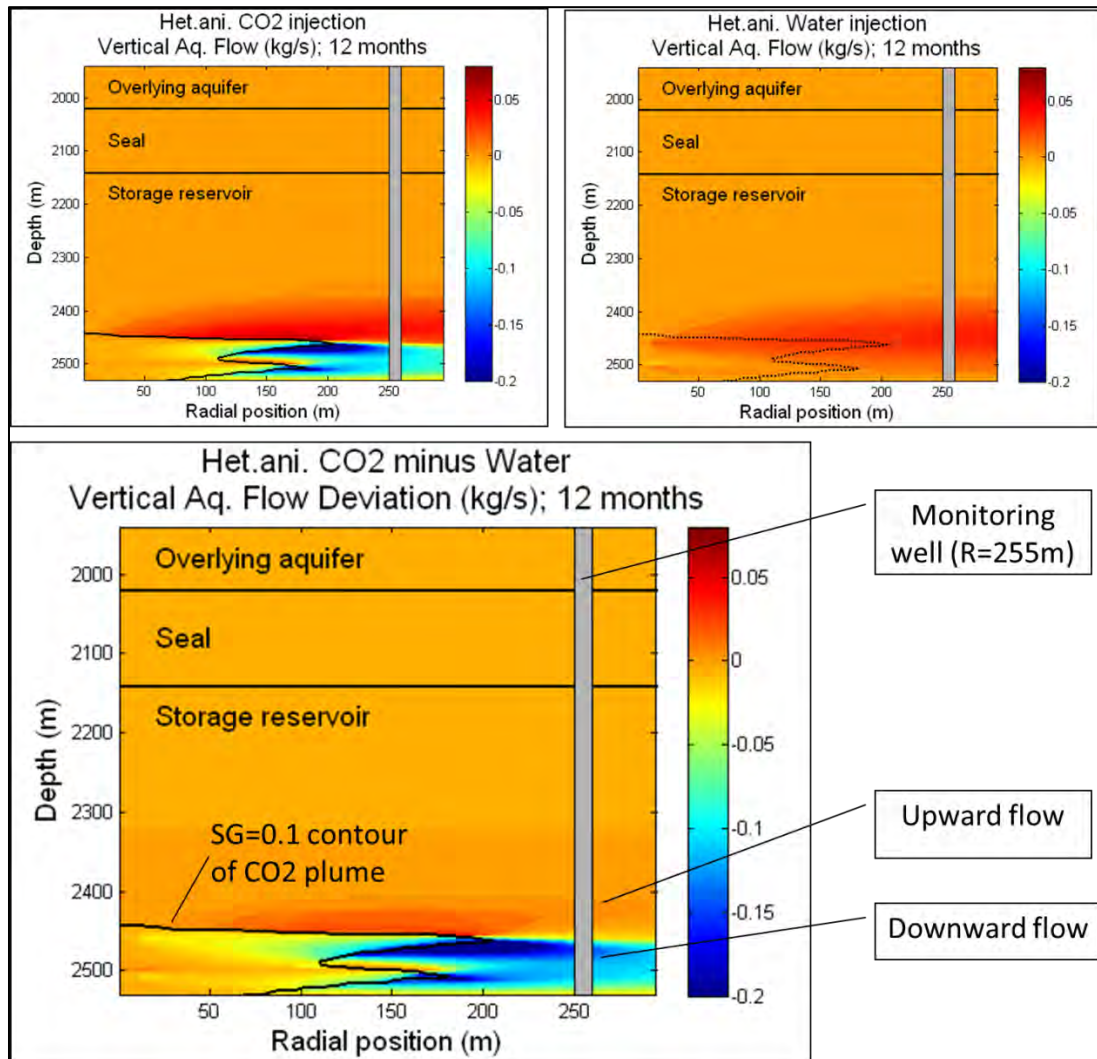
Figure 5.16: Vertical aqueous flow for the heterogeneous anisotropic scenario. Negative values indicate downward flow; positive values indicate upward flow. Upper left: Vertical flow after 12 months of CO_2 injection. Upper right: Vertical flow after 12 months of water injection. Bottom: Vertical flow for CO_2 injection from which the vertical flow for water injection has been subtracted.

5.4. Placement of Multilevel Pressure Monitors

Last, we need to consider where to place the pressure monitors for a real case setting. For the analysis of vertical pressure gradients normalized to the initial hydrostatic pressure we assumed that we had pressure sensors every 5 m (i.e., in every grid cell in the

simulation model), but for a real case scenario that would likely not be economically feasible.

Even though the number of pressure monitors might be limited by cost, we would still like to have as many pressure monitors in the storage reservoir as possible. The more pressure monitors are placed in the reservoir, the more information on reservoir heterogeneity and position of CO_2 plume can be obtained. In particular, pressure monitors should be placed at the depth of injection, and also in the lower permeability layers above, as this is where we see the largest anomalies in pressure response (due to resistance to flow). A few monitors should also be placed in the seal and in the overlying aquifer, as large pressure anomalies in the seal are indicative of the CO_2 plume having migrated to the top of the storage reservoir, and since we want to be able to detect possible leaks through the seal and into the overlying aquifer.

82

Chapter 6

6. Conclusions and Future Work

6.1. Conclusions

The objective of this research was to conduct a simulation study to evaluate the effectiveness of vertically distributed pressure monitors. Demonstration projects for large scale implementation of CO_2 sequestration are now in place that will have pressure monitoring not just in permeable zones above the seal but also at multiple depths in the storage reservoir itself. In the context of CCS, the concept of pressure monitoring in permeable zones above the seal is not new, and the diagnostic and interpretative value of such measurements have been illustrated for various leakage scenarios (e.g. Chabora, 2009). Multilevel pressure monitoring is nevertheless a technique that has yet to be thoroughly investigated. Using the Illinois Basin-Decatur Project at ADM's facilities in Illinois as a basis for the model setup and a nearby well as a predictor for the stratigraphy, we conducted a simulation study of various scenarios for which supercritical CO_2 was injected into the bottom of a 30-layer system comprised of storage reservoir, seal, and overlying aquifer. Through the simulations conducted in this investigation, we can make the following observations and conclusions about multilevel pressure monitoring and its application to CO_2 sequestration:

- Unless there is a seal separating the monitoring zone from the storage reservoir, large, measurable pressure changes can be observed (we did not consider leakage scenarios, in which case large pressure changes would have been expected above the seal as well). Distinct pressure transients for the different system scenarios suggest that system heterogeneity has a substantial impact on the pressure response. However, pressure transients from individual monitoring points alone appear not to be very diagnostic of the nature of the heterogeneity of the system or the location of the CO_2 plume. Simultaneous inversion of pressure transient

data from multiple zones could be helpful in defining the nature of the heterogeneity, but this has not been attempted here.

- Normalized vertical pressure gradients provide 1) a clear representation of the system heterogeneity soon after start of injection, 2) distinct, separate features depending on whether CO_2 is present in the system, and 3), a strong indication of where the CO_2 is in the reservoir, i.e. at what depth, prior to the CO_2 arriving at the monitoring well.

- Anomalous vertical pressure gradients can be attributed to anomalous vertical aqueous flow in the storage reservoir. The vertical flow is caused by water being displaced by the advancing CO_2 plume.

- As many pressure monitors as possible should be placed at the depth of injection and in low permeability layers above. For a strongly heterogeneous and anisotropic system, the CO_2 plume is likely to be contained to the depth of injection; for less anisotropic systems the CO_2 plume may migrate to shallower depths in the storage reservoir.

Given the observations just listed, our study confirms the basis for an inverse method for reservoir characterization and CO_2 plume migration detection. Before a more formal method for inverting the pressure data can be developed, several concerns need to be addressed, some of which involve answering the questions for future work listed in Section 6.2.

6.2. Remaining Questions for Future Work

The most pressing matter with regard to future work involves inputting the real geologic data from the ADM site into the simulation model. In order to more accurately evaluate the effectiveness of multilevel pressure monitoring, it is important to have a real case

scenario to compare with. Other questions and ideas generated during the course of this investigation involve the following:

- The porosity and corresponding horizontal permeabilities from the Weaber-Horn #1 well, on which we based our simulation model, were average values based on a division of the Mt. Simon Sandstone into distinct hydrogeologic layers. A sensitivity analysis should be conducted on porosity and permeability distributions as well as on the layer thickness and the number (and ordering) of distinct layers.

- The location of the injection zone may be varied to see what the effects are.

- In our simulation study we placed the monitoring well 255 m from the injection well. A sensitivity analysis may be conducted on the location of the monitoring well as well as on the rate of injection.

- Though the stratigraphic layers at the ADM site are expected to be fairly horizontal, it might be useful to study the effect of dipping stratigraphic layers as well as system heterogeneity in the lateral direction.

- Leakage scenarios have previously been studied for above-zone pressure monitoring (e.g. Chabora, 2009) but were not considered in this investigation of multilevel pressure monitoring. In this investigation we were more concerned with the method's effectiveness with regard to detecting CO_2 plume migration in the storage reservoir. However, we are also interested in effectiveness of multilevel pressure monitoring in preventing and/or detecting leakage into overlying aquifers, hence it would be optimal if future work would include studies of various leakage scenarios.

- Finally, an optimization strategy for where to place the pressure monitors and how closely they should be spaced would be beneficial.

Nomenclature

Abbreviations

ADM	Archer Daniels Midland Company
AZMI	Above-zone monitoring interval
CCS	Carbon dioxide capture and storage
Ei	$\int_{y=u}^{\infty} \frac{e^{-y}}{y} dy;$ Exponential Integral
EOR	Enhanced oil recovery
EOS	Equation of State
EPA	Environmental Protective Agency
GtC	Giga tons of Carbon
IFD	Integral Finite Difference
IPCC	Intergovernmental Panel on Climate Change
ISGS	Illinois State Geological Survey
LBNL	Lawrence Berkeley National Laboratory
LIDAR	Laser Systems and Light Detection and Ranging
MGSC	Midwest Geological Sequestration Consortium
NETL	National Energy Technology Laboratory
PDE	Partial Differential Equation
psi	pounds-force per square inch
SG	Gas saturation
SRO	Surface Read-Out

Symbols

C	specific heat capacity	$\left(\frac{J}{kg\,^{\circ}C}\right)$
c_R	rock compressibility	(Pa^{-1})

c_t	total system compressibility	(Pa^{-1})
Δd	depth below the water table	(m)
F	mass or heat flux	$\left(\frac{kg}{m^2\,s}\right)$ or $\left(\frac{J}{m^2\,s}\right)$
g	vector of acceleration due to gravity	(m/s^2)
h	thickness or height of rock layer	(m)
J	Leverett J-function	(-)
K	wet heat conductivity	$\left(\frac{W}{m\,°C}\right)$
k	absolute permeability of rock formation (SI), field	(m^2), md
kH	permeability in the horizontal direction (SI), field	(m^2), md
kV	permeability in the vertical direction (SI), field	(m^2), md
k_r	relative permeability of a phase	
	[in Equation 2.1: radial component of	
	permeability tensor] (SI), field	(m^2), md
M	total mass of a component	(kg)
NK	total number of components	(-)
n	inward-pointing normal vector	(-)
P, p	fluid pressure (SI), field	(Pa), psi
P_{atm}	atmospheric pressure (SI), field	(101,325 Pa), 14.7 psi
P_c	capillary pressure between immiscible phases (SI), field	(Pa), psi
P_0	capillary entry pressure of non-wetting phase (SI), field	(Pa), psi
Q	volumetric flow rate	(m^3/s)
q	mass flow rate	(kg/s)
r	radial distance	(m)
S	saturation or fraction of the pore space occupied by a phase	(-)
T	temperature	(°C)
t	time	(s)
V	arbitrary volume within flow system	(m^3)
X	mass fraction of a component in a phase	(-)
z	vertical position or depth in the reservoir	(m)

Greek Symbols

θ	azimuthal orientation	(radians)
Θ	contact angle between two immiscible fluids	(°)
σ	interfacial tension between immiscible phases	(mN/m)
φ	porosity	(-)
μ	fluid viscosity	(Pa·s)
ρ	mass density	(kg/m^3)
$\overline{\rho_w}$	average water mass density	(kg/m^3)
Γ	closed surface of arbitrary volume	(-)
λ	fitting parameter for the van Genuchten capillary pressure model	(-)
Δ	change in value	(-)
∇	gradient, i.e., for Cartesian coordinates and arbitrary scalar G, $\nabla G = \left(\hat{\mathbf{x}} \frac{\partial}{\partial x} + \hat{\mathbf{y}} \frac{\partial}{\partial y} + \hat{\mathbf{z}} \frac{\partial}{\partial z} \right) G$	(m^{-1})

Subscripts

g	pertaining to the non-wetting phase (here: CO_2)
gr	pertaining to the residual non-wetting phase (TOUGH2 notation)
i	initial state of conditions in the reservoir
l	pertaining to the wetting phase (TOUGH2 notation) (here: water)
lr	pertaining to the residual wetting phase (TOUGH2 notation)
ls	pertaining to the saturated wetting content (TOUGH2 notation)
max	maximum value
n	index
nw	pertaining to the non-wetting phase
R	pertaining to the rock formation
r	radial component of permeability tensor
z	vertical component of permeability tensor or vertical position in the reservoir

w   pertaining to the wetting phase

θ azimuthal component of permeability tensor

β phase (e.g. gas, liquid)

1   shallower grid cell

2   deeper grid cell

Superscripts

κ component

References

Alcott, A., Swenson, D. and Hardeman, B., 2006, "Using PetraSim to Create, Execute, and Post-Process TOUGH2 Models," *Proceedings TOUGH Symposium 2006,* Lawrence Berkeley National Laboratory, Berkeley, California.

Atherton, E., 1975, "Precambrian Rocks" in *Handbook of Illinois Stratigraphy: Illinois State Geological Survey Bulletin 95*, eds. H.B. Willman, E. Atherton, T.C. Buschbach, C. Collinson, J.C. Frye, M.E. Hopkins, J.A. Lineback and J.A. Simon, Urbana, Illinois, pp. 32-33.

Benbennick, D., February, 2006*, Map of Illinois highlighting Macon County,* Homepage of Wikipedia, The Free Encyclopedia. May, 2011. Available: http://en.wikipedia.org/wiki/File:Map_of_Illinois_highlighting_Macon_County.svg

Benson, S.M., Gasperikova, E. and Hoversten, G.M., 2004, "Overview of Monitoring Techniques and Protocols for Geologic Storage Projects," IEA Greenhouse Gas R&D Programme Report.

Benson, S.M. and Hepple, R., 2005, "Prospects for Early Detection and Options for Remediation of Leakage from CO2 Storage Projects" in *Carbon Dioxide Capture for Storage in Deep Geologic Formations, Volume 2*, eds. S.M. Benson & D.C. Thomas, Elsevier Ltd.

Benson, S.M., Hepple, R., Apps, J., Tsang, C.F. and Lippmann, M., 2002, *Lessons Learned from Natural and Industrial Analogues for Storage of Carbon Dioxide in Deep Geological Formations*, Report LBNL-51170, Lawrence Berkeley National Laboratory, Berkeley, California.

Benson, S.M., Myer, L.R., Oldenburg, C.M., Doughty, C.A., Pruess, K., Lewicki, J., Hoversten, M., Gasperikova, E., Daley, T., Majer, E., Lippmann, M., Tsang, C.-., Knauss, K., Johnson, J., Foxall, W., Ramirez, A., Newmark, R., Cole, D., Phelps,

T.J., Parker, J., Palumbo, A., Horita, J., Fisher, S., Moline, G., Orr, L., Kovscek, T., Jessen, K., Wang, Y., Zhu, J., Cakici, M., Hovorka, S., Holtz, M., Sakurai, S., Gunter, B., Law, D. and van der Meer, B., 2004, *GEO-SEQ Best Practices Manual. Geologic Carbon Dioxide Sequestration: Site Evaluation to Implementation.*, Report LBNL-56623, Lawrence Berkeley National Laboratory, Berkeley, California.

Benson, S.M., Trautz, R. and Shan, C. 2006, "Sensitivity of Pressure Monitoring for Leak Detection," *presented at the Fifth Annual Conference on Carbon Capture and Sequestration,* Alexandria, Virginia, May 8-11.

Bergstrom, R.E., Piskin, K. and Follmer, L.R., 1976, *Geology for planning in the Springfield-Decatur Region, Illinois*, Illinois State Geological Survey Circular 497, 76 p., Urbana, Illinois.

Bickford, M.E., Van, W.R. and Zietz, I., June, 1986, "Proterozoic history of the midcontinent region of North America," *Geology,* vol. 14, no. 6, pp. 492-496.

Birkholzer, J.T., 2009, *Basin-Scale Hydrologic Impacts of CO2 Storage: Regulatory and Capacity Implications*, Report LBNL-1716E, Lawrence Berkeley National Laboratory, Berkeley, California.

Birkholzer, J.T., Zhou, Q. and Tsang, C., 2009, "Large-scale impact of CO2 storage in deep saline aquifers: A sensitivity study on pressure response in stratified systems," *International Journal of Greenhouse Gas Control,* vol. 3, no. 2, pp. 181-194.

Buschbach, T.C., 1975, "Cambrian System" in *Handbook of Illinois Stratigraphy: Illinois State Geological Survey Bulletin 95*, eds. H.B. Willman, E. Atherton, T.C. Buschbach, C. Collinson, J.C. Frye, M.E. Hopkins, J.A. Lineback and J.A. Simon, Urbana, Illinois, pp. 34-46.

Buschbach, T.C. and Kolata, D.R., 1991, "Regional Setting of the Illinois Basin" in *Interior Cratonic Basins*, eds. M.W. Leighton, D.R. Kolata, D.F. Oltz and J.J. Eidel, AAGP Memoir 51, pp. 29-55.

Chabora, E., 2009, *The Utility of Above-Zone Pressure Measurements in Monitoring Geologically Stored Carbon Dioxide*, Master of Science Report, Stanford University, Stanford, California.

Cherry, J.A., Gillham, R.W., Anderson, E.G. and Johnson, P.E., 1983, "Migration of contaminants in groundwater at a landfill: A case study : 2. Groundwater monitoring devices," *Journal of Hydrology,* vol. 63, no. 1-2, pp. 31-49.

Cherry, J.A. and Johnson, P.E., 1982, "A multilevel Device for Monitoring in Fractured Rock," *Ground Water Monitoring & Remediation,* vol. 2, no. 3, pp. 41-44.

Cherry, J.A., Parker, B.L. & Keller, C., 2007, "A New Depth-Discrete Multilevel Monitoring Approach for Fractured Rock," *Ground Water Monitoring & Remediation,* vol. 27, no. 2, pp. 57-70.

Cooper, K., 2011*, Multilevel Monitoring Well Installations,* Homepage of Solinst Canada Ltd. May 2011. Available: http://www.solinst.com/Res/papers/401K.html

Corey, A.T., 1954, "The Interrelation Between Gas and Oil Relative Permeabilities," *Producers Monthly,* vol. 19, no. 1, pp. 38-41.

Davis, H.G., 1991, "Pre-Mississippian Hydrocarbon Potential of the Illinois Basin" in *Interior Cratonic Basins*, eds. M.W. Leighton, D.R. Kolata, D.F. Oltz and J.J. Eidel, AAPG Memoir 51, pp. 473-489.

Doughty, C., Benson, S. and Pruess, K., 2002, *Capacity investigation of brine-bearing sands for geologic sequestration of CO_2*, Report LBNL-51333, Lawrence Berkeley National Laboratory, Berkeley, California.

Droste, J.B. and Patton, J.B., 1985, *Lithostratigraphy of the Sauk sequence in Indiana*, Indiana Department of Natural Resources, Geological Survey Occational Paper 47, 24p.

Droste, J.B. and Shaver, R.H. 1983, *Atlas of early and middle Paleozoic paleogeography of the southern Great Lakes area*, Indiana Department of Natural Resources, Geological Survey Special Report 32, 32p.

Finley, R., *MGSC/ISGS Carbon Sequestration Demonstration Project,* Homepage of Illinois Sustainable Technology Center, University of Illinois at Urbana-Champaign, April 15, 2009. Accessed May 2011. Available: http://www.istc.illinois.edu/about/SustainabilitySeminar20090415.cfm.

Finley, R.J., *Permitting and Developing a 1 Million Tonne Geological Sequestration Test in a Deep Saline Reservoir at Decatur, Illinois, USA*, presented at the Irish Academy of Sciences, March 11, 2010.

Fishman, N.S., 1997, "Basin-wide fluid movement in a Cambrian paleoaquifer: evidence from the Mt. Simon sandstone, Illinois and Indiana" in *Basin-wide diagenetic patterns: Integrated petrologic, geochemical, and hydrologic considerations*, eds. I.P. Montanez, J.M. Gregg and K.I. Shelton, SEPM Special Publication No. 57, pp. 221-234.

Horne, R.N., 1995, *Modern Well Test Analysis,* Second Edition, Petroway, Palo Alto, California.

Houseknecht, D.W. and Ethridge, F.G., 1978, "Depositional history of the Lamotte Sandstone of southeast Missouri," *Journal of Sedimentary Petrology,* vol. 48, pp. 575-586.

Houseknecht, D.W. and Weaverling, P.H., 1983, "Early Paleozoic sedimentation in Reelfoot rift," *AAPG Bull.,* vol. 67, pp. 146.

Howe, J.R. and Thompson, T.L., 1984, "Tectonics, sedimentation, and hydrocarbon potential of the Reelfoot rift," *Oil and Gas Journal,* vol. 82, pp. 179-190.

IPCC, 2005, *IPCC Special Report on Carbon Dioxide Capture and Storage. Prepared by Working Group III of the Intergovernmental Panel on Climate Change.*, Cambridge University Press, Cambridge, United Kingdom and New York, NY, USA, 442 pp.

Katz, D.L. and Coats, K.H., 1968, *Underground Storage of Fluids,* Distributed by Ulrich's Books Inc., Ann Arbor, Michigan.

Kolata, D.R., 1991, "Overview of Sequences" in *Interior Cratonic Basins*, eds. M.W. Leighton, D.R. Kolata, D.F. Oltz and J.J. Eidel, AAPG Memoir 51, pp. 59-73.

Leverett, M.C., 1941, "Capillary behavior in porous solids," *Trans. AIME 142,* pp. 152-169.

Macke, D.L., 1995, "Illinois Basin Province (064)" in *National assessment of United States oil and gas resources--Results, methodology, and supporting data: U.S. Geological Survey Digital Series DDS-30, Release 2, one CD-ROM*, eds. D.L. Gautier, G.L. Dolton, K.I. Takahashi and K.L. Varnes,.

Meckel, T.A. and Hovorka, S.D., 2010, "Above-Zone Pressure Monitoring as a Surveillance Tool for Carbon Sequestration Projects," *SPE International Conference on CO2 Capture, Storage, and Utilization*, 10-12 November 2010, SPE 139720.

Merritt, E.A. and Parsons, P.J., 1960, "Sampling devices for water and soil" in *Disposal of Radioactive Wastes*, Vol. II, Vienna, Austria: IAEA, pp. 329-338.

Narasimhan, T.N. and Witherspoon, P.A., 1976, "An Integrated Finite Difference Method for Analyzing Fluid Flow in Porous Media," *Water Resources Research,* vol. 12, no. 1, pp. 57-64.

National Energy Technology Laboratory (NETL), 2009, *Best Practices for Monitoring, Verification, and Accounting of CO_2 Stored in Deep Geologic Formations*, First Edition, U.S. Department of Energy Report: DOE/NETL-311/081508, http://www.netl.doe.gov/technologies/carbon_seq/refshelf/MVA_Document.pdf.

Patton, J.B. and Dawson, T.A., 1969, "Some petroleum prospects of the Cincinnati Arch province", *Proceedings of Technical Sessions, Kentucky Oil and Gas Association, 33rd Ann. Mtg., June 5-6, 1969,* Kentucky Geological Survey, Series X, Special Publication 18, pp. 32.

Perry, K.F., 2005, "Natural Gas Storage Industry Experience and Technology: Potential Application to CO_2 Geologic Storage" in *Carbon Dioxide Capture for Storage in Deep Geologic Formations, Volume 2*, eds. D.C. Thomas and S.M. Benson, Elsevier Ltd.

Pickens, J.F., Cherry, J.A., Grisak, G.E., Merritt, W.F. and Risto, B.A., 1978, "A Multilevel Device for Ground-Water Sampling and Piezometric Monitoring," *Ground Water,* vol. 16, no. 5, pp. 322-327.

'Pressure-Transient Analysis,' 2011, Homepage of Oilfield Glossary, Schlumberger Limited. 2011. Available: http://www.glossary.oilfield.slb.com/Display.cfm?Term=pressure-transient%20analysis.

Pruess, K., 2005, *ECO2N: A TOUGH2 Fluid Property Module for Mixtures of Water, NaCl, and CO_2*, Report LBNL-57952, Lawrence Berkeley National Laboratory, Berkeley, California.

Pruess, K., 1991, *A General-Purpose Numerical Simulator for Multiphase Fluid and Heat Flow*, Report LBNL-29400, Lawrence Berkeley National Laboratory, Berkeley, California.

Pruess, K., 1987, *TOUGH User's Guide, Nuclear Regulatory Commission*, Report NUREG/CR- 4645; also Lawrence Berkeley Laboratory Report LBL-20700.

Pruess, K., Oldenburg, C.M. and Moridis, G.J., 1999, *TOUGH2 User's Guide Version 2*, Report LBNL-43134, Lawrence Berkeley National Laboratory, Berkeley, California.

Sargent, M.L., 1991, "Sauk Sequence: Cambrian System through Lower Ordovician Series" in *Interior Cratonic Basins*, eds. M.W. Leighton, D.R. Kolata, D.F. Oltz and J.J. Eidel, AAPG Memoir 51, pp. 75-85.

Solomon, S., Qin, D., Manning, M., Alley, R.B., Berntsen, T., Bindoff, N.L., Chen, Z., Chidthaisong, A., Gregory, J.M., Hegerl, G.C., Heimann, M., Hewitson, B., Hoskins, B.J., Joos, F., Jouzel, J., Kattsov, V., Lohmann, U., Matsuno, T., Molina, M., Nicholls, N., Overpeck, J., Raga, G., Ramaswamy, V., Ren, J., Rusticucci, M., Somerville, R., Stocker, T.F., Whetton, P., Wood, R.A. and Wratt, D., 2007, *Technical Summary. In: Climate Change 2007: The Physical Science Basis. Contribution of Working Group I to the Fourth Assessment Report of the Intergovernmental Panel on Climate Change*, Cambridge University Press, Cambridge, United Kingdom and New York, NY, USA.

Spycher, N. and Pruess, K., 2005, "CO2-H2O mixtures in the geological sequestration of CO2. II. Partitioning in chloride brines at $12–100°C$ and up to 600 bar," *Geochimica et Cosmochimica Acta,* vol. 69, no. 13, pp. 3309-3320.

Theis, C.V., 1935, "The Relationship Between the Lowering of the Piezometric Surface and the Rate and Duration of Discharge of a Well Using Ground-water Storage," *Trans. Am. Geophys. Union,* vol. 16, pp. 519-524.

United States Environmental Protection Agency (EPA), 1986, *RCRA Ground-Water Monitoring Technical Enforcement Guidance Document (TEGD)*, US Government Printing Office OSWER-9950.1.

van Genuchten, M.T., 1980, "A Closed-form Equation for Predicting the Hydraulic Conductivity of Unsaturated Soils," *Soil Sci. soc. Am. J.,* vol. 44, pp. 892-898.

Willman, H.B., 1975, "Paleozoic Erathem" in *Handbook of Illinois Stratigraphy: Illinois State Geological Survey Bulletin 95*, eds. H.B. Willman, E. Atherton, T.C. Buschbach, C. Collinson, J.C. Frye, M.E. Hopkins, J.A. Lineback and J.A. Simon, Urbana, Illinois, pp. 33-34.

Zeidouni, M., in preparation, *Geological Sequestration of CO$_2$ in Saline Aquifers: Injectivity and Leakage*, PhD Dissertation, University of Calgary, Calgary, Canada.

Zeidouni, M. and Pooladi-Darvish, M., 2010, "Characterization of Leakage through Cap-Rock with Application to CO2 Storage in Aquifers - Single Injector and Single Monitoring Well," *Canadian Unconventional Resources and International Petroleum Conference*, 19-21 October 2010, SPE 138178.

Zhang, K., Wu, Y.S. and Pruess, K., 2008, *User's Guide for TOUGH2-MP - A Massively Parallel Version of the TOUGH2 Code*, Report LBNL-315E, Lawrence Berkeley National Laboratory, Berkeley, California.

Zhou, Q., Birkholzer, J.T., Mehnert, E., Lin, Y. and Zhang, K., 2010, "Modeling Basin- and Plume-Scale Processes of CO2 Storage for Full-Scale Deployment," *Ground Water,* vol. 48, no. 4, pp. 494-514.